Growth of Graphene and MoS2 by Chemical Vapour Deposition

ALSULAMI, TAGHREED,SULAIMAN,B

Growth of Graphene and MoS_2 by Chemical Vapour Deposition

Taghreed Sulaiman Alsulami

A thesis submitted in partial fulfillment of the requirements
for the degree of
Doctor of Philosophy

Supervised by Dr. Michael R. C. Hunt
Department of Physics
University of Durham
UK
November 2022

Growth of Graphene and MoS_2 by Chemical Vapour Deposition

Taghreed Sulaiman Alsulami

Abstract

The growth of two-dimensional materials by low-cost atmospheric pressure chemical vapour deposition (AP-CVD) is explored in this thesis, with an emphasis on understanding key features of the growth process. In particular, the growth of graphene on copper foils using a methane precursor, MoS_2 on natively oxidised silicon and MoS_2 on graphene, graphite and graphene 'paper' were studied. The resulting few-layer, monolayer and sub-monolayer films were characterised by a combination of Raman spectroscopy (RS), Scanning Electron Microscopy (SEM) and X-ray photoelectron spectroscopy (XPS).

Through varying the methane flow rate it was found that there is no self-limitation to graphene growth at high methane concentrations, resulting in graphene multilayers that can delaminate from the copper substrate. The effect of a number of surface pre-treatments on graphene growth is also presented. Nitric acid etching of copper foil was found to produce a superior growth surface in comparison with those prepared with acetic acid or electropolishing, evidenced by a reduction in nucleation density and increased island size. Raman spectra showed a remarkable correlation with these observations, indicating increased hole doping with improved sample treatment. Therefore, Raman spectroscopy may be used as a probe for the effectiveness of surface preparation. Several different approaches to the growth of MoS_2 on natively oxidised silicon by AP-CVD using S and MoO_3 precursors are presented. It was found that the growth of MoS_2 was strongly dependent on the timing with which a sufficient sulphur flux is introduced into the growth region. These results led to an investigation into the influence of sulphur partial vapour pressure on MoS_2 growth. It was found that MoS_2 coverage decreased with increasing sulphur vapour pressure. These results could be successfully rationalised by the Langmuir-Hinshelwood model of growth kinetics, which is usually applied to reactions on well-defined crystalline surfaces and had not previously been considered for MoS_2 growth. XPS was used to study the composition of AP-CVD grown MoS_2 as a function of sulphur evaporation temperature and provided clear evidence that lower sulphur vapour pressure leads to an increased concentration of sulphur vacancy defects.

Attempts were made to grow MoS_2 directly on highly oriented pyrolytic graphite as a model substrate. MoS_2 was found to grow on graphite under similar conditions to those for natively oxidised silicon, but nucleation was observed to occur primarily at defect (step) sites. Attempts to grow MoS_2 directly on graphene CVD grown on copper, commercially sourced graphene powder, and graphene paper are also reported.

Contents

List of Figures

List of Tables

Declaration

The material contained within this thesis has not previously been submitted for a degree at the University of Durham or any other university. The research reported within this thesis has been conducted by the author unless indicated otherwise.

Acknowledgements

My deepest gratitude goes to Almighty Allah, the most Merciful and Beneficent, who granted me with a shower of blessings and the strength that I needed to complete this research with merit.

I would like to thank my supervisor, Dr. Michael R. C. Hunt, for his guidance and help.

I am also thankful to Mr. Leon Bowen for his help with SEM measurements.

I also thank the IT and technical staff, and especially appreciate the effort of Mr. Duncan McCallum and Mr. David Pattinson in the labs.

Thank you to the glassblowing workshop in the Department of Chemistry, Malcolm Richardson and Aaron Brown for designing quartz tubes.

I thank Prof. Lidija Siller for XPS measurements at the NEXUS facility, Newcastle University and Dr. Michael Hunt for fitting the XPS data.

I am also grateful to my office-mates, Alina, Amy, Divya, Latifah, Rachel, Ruthie and Sarah, for their help and constant support at all times, especially during the most difficult ones.

I am very grateful to the Ministry of Higher Education, Umm AlQura University in Saudi Arabia and Saudi Culture Bureau in London for making my dreams possible.

All the love goes to my family: my mother, brothers and sisters for their sincere prays, wishes, and endless support and my nuclear family, my kids Faisal, Tala and my little Baby AlQais, and especially my husband Abdulelah for their patience and support during my Ph.D journey.

I am very thankful to my close friends in Saudi Arabia for all their support throughout my studies.

Taghreed Sulaiman Alsulami, Durham UK, 2022

Chapter 1

Introduction

This chapter provides a brief introduction to some members of the family of two- dimensional (2D) materials, with particular emphasis on graphene and molybdenum disulphide (MoS_2). The structure, properties and preparation of these materials are also discussed.

1.1 Introduction

Graphene was the first 2D material to be successfully isolated, a feat which was achieved in 2004 [1]. Isolating graphene opened the door to other two-dimensional materials such as molybdenum disulphide (MoS_2), boron nitride (h-BN), other dichalcogenides and layered oxides. These 2D materials possess a number of desirable properties distinct from their bulk structure. This chapter provides a brief introduction to some members of the family of 2D materials, their structures and their properties.

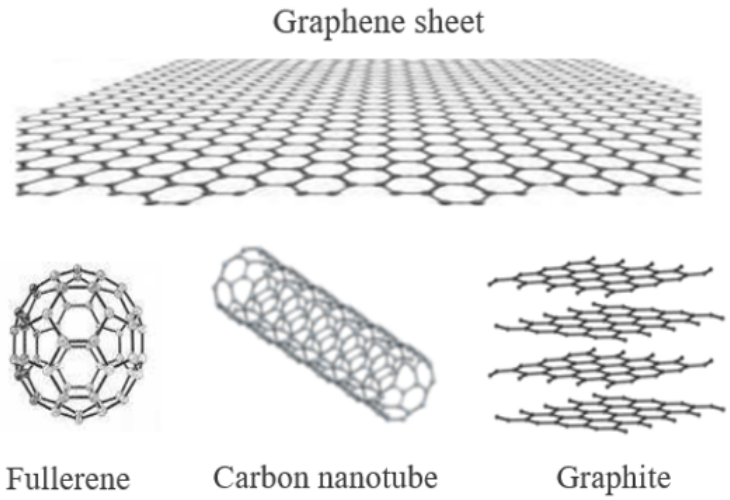

Figure 1.1: *Graphene can be considered to be the origin of all graphtic forms. The basic structure of graphene can, in a thought experiment, be 'wrapped up' into a 0D fullerene, 'rolled up' into 1D nanotubes and stacked into 3D graphite. Adapted from [2].*

1.1.1 Graphene

Graphene is considered to be the origin of all graphitic forms, whatever their dimensionality, since its structure forms the basis of graphite, 1D carbon nanotubes and 0D fullerenes [2] as seen in Figure 1.1. The isolation of graphene was relatively recent as it was originally thought that a single, isolated, layer would be unstable. The first investigation of graphene and its band structure was carried out by Wallace in 1947 [3]; this study found that graphene is zero band gap semiconductor. Geim and Novoselov, in 2004, were the first who successfully isolated monolayer graphene by using the simple approach of micromechanical cleavage [1]. In 2010, they gained the Nobel Prize in Physics for this work. More recently, single and multi-layer graphene have been grown via chemical vapour deposition

(CVD) [4, 5, 6] on metal films using hydrocarbon precursors and expitaxially by thermal decomposition of SiC [7, 8]. Epitaxial growth of graphene can produce high quality films and is readily scalable [6] although, currently, it is generally agreed that micromechanical cleavage produces graphene with the lowest density of defects.

Graphene has been a prime focus of much recent research because of its exciting properties, e.g., the unusual structure of graphene gives rise to numerous interesting behaviours such as an extremely high carrier mobility ($350,000$ cm^2 V^{-1} s^{-1}) [9]), a constant absorption of only 2.3% of light across the whole of the visible range [10] and excellent thermal conductivity ($\approx$ 5000 W m^{-1} K^{-1} [11]). Since films of graphene are conducting, transparent and have a very high degree of flexibility they are regarded as excellent candidates for use in applications such as field effect transistors [12], transparent conductors in solar cells, and they have been suggested as a potential replacement for indium tin oxide (ITO) in touch screens [13] in the future. The isolation of monolayer graphene provided the inspiration for the isolation/growth of a wide variety of related two-dimensional materials [14] such as molybdenum disulphide (MoS_2), boron nitride (hBN), other dichalcogenides and layered oxides. The existence of a large family of two-dimensional solids, each with their own unique electronic and optical properties, has led to the idea of the controlled assembly of isolated sheets of different two-dimensional materials into stacks known as van der Waals heterostructures, (in analogy to semiconductor heterostructures). Such structures, which have recently been successfully demonstrated in the laboratory [15, 16], will be discussed in more detail below.

1.1.2 Graphene structure

The structure of monolayer graphene consists of hexagons of carbon atoms tiled to fill a two-dimensional space, see Figure 1.2a). It is necessary to consider the bonding between the carbon atoms to understand the origin of the hexagonal lattice. The carbon atoms in graphene have sp^2 hybridization in which the $2s$ orbitals undergo superposition with $2p_x$ and $2p_y$ orbitals form three sp^2 hybridized orbitals oriented at 120° to each other. An unhybridized p_z orbital is left perpendicular to the planar structure, see 1.2b). Due to the overlap of sp^2 orbitals on neighboring carbon atoms three strong σ bonds are formed. These covalent bonds are responsible for the mechanical properties of graphene and, in the absence of defects, make it the strongest material in nature [17]. The perpendicular p_z orbital overlaps with those on adjacent carbon atoms, leading to the formation of a delocalized state located near the Fermi level in the graphene band structure. I.e., the overlapping p_z orbitals lead to a filled band (π bonding orbital) and an empty band (π^* antibonding orbital) which are responsible for the conductivity of graphene. As shown from Figure 1.2a), the unit cell of graphene lattice has two carbon atoms, A and B, each forming

a triangular 2D lattice and these carbon atoms are displaced by a distance $a_{c-c} = 0.142$ nm with respect to each other [17].

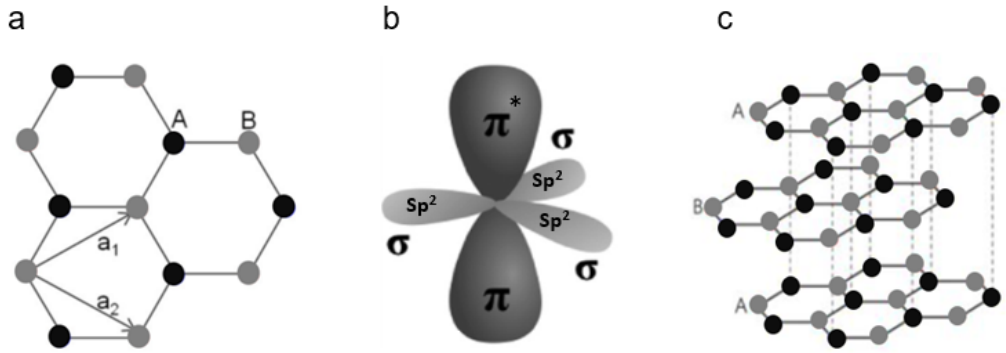

Figure 1.2: *(a) Top view of the real space unit cell of monolayer graphene with unit vectors a_1 and a_2, including both the inequivalent A and B atoms. (b) Arrangement of the sp2-hybridised orbitals in graphene; an unhybridized p_z orbital is left perpendicular to the planar structure. (c) The Bernal (AB) stacking present in graphite. Adapted from [17].*

The structure of three-dimensional graphite (bulk) can be produced by stacking individual graphene sheets parallel to one another, and is held together due to the van der Waals forces acting between the individual graphene layers, which are much weaker than the in-plane bonds. The most common (and lowest energy) stacking arrangement found in graphite is the AB (or Bernal) type in which atoms in the upper layer are located at the vacant centers of the hexagons of the lower layer, as seen in Figure 1.2c). With AB stacking in graphite, the unit cell contains four carbon atoms on two unique layers. Other stacking arrangements are also possible, such as AA and disordered (often known as turbostratic) stacking. However, Bernal stacking is the most common and is often preserved during exfoliation, as can be seen from investigations of exfoliated bilayer graphene which normally exhibits AB stacking, and has four atoms in its unit cell. Trilayer graphene has three layers, two of which are the same as that in bilayer graphene, but the third layer is displaced with respect of the other two layers, as shown in Figure 1.2c) [18].

The valence (π), and conduction (π^*) bands meet each other at six points located at the corner of the 2D honeycomb-shaped Brillouin zone [3]. These are inequivalent points labeled with the symbols K and $K^{'}$ and are known as Dirac points, as shown in Figure 1.3. The dispersion relation for charge carriers (electron and holes) close to Fermi level is linear.

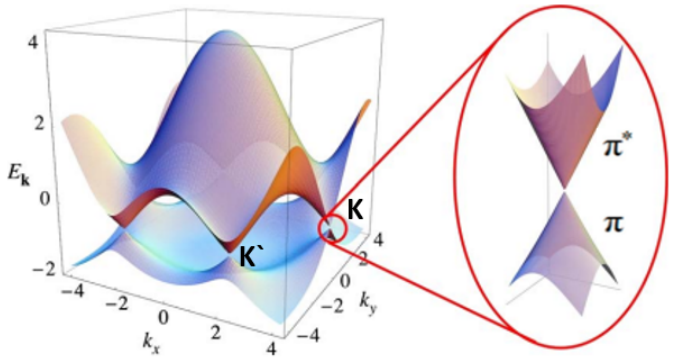

Figure 1.3: *Graphene band structure, showing both valence (π) and conduction (π^*) bands at six points in Brillouin zone [17].*

1.1.3 Other Two-Dimensional Nanomaterials

Graphene, as the first two-dimensional material discovered [1] and the most studied so far, can be regarded as the prototype for an entire family of two-dimensional solids and their derivatives. As discussed in detail in the section above, graphene has an unusual band structure that provides high-electronic mobility, however its zero-energy band gap makes unmodified graphene unsuitable for digital electronics: for example, due to the absence of a band gap the ON:OFF ratio of graphene field effect transistors (FETs) is many orders of magnitude below that required for digital logic and information storage [19]. To solve this problem there have attempts to produce novel graphene materials with band gaps through chemical modification [6] or by exploiting quantum confinement through the production of thin 'ribbons' [20]. Ribbons have been produced with a band gap up to 400 meV [21] but there are issues such as mobility reduction, loss of coherence and the need for operating voltages exceeding 100 V, which make building logic circuits that would operate at room temperature with low power dissipation difficult. Therefore, the focus has turned towards fabrication of devices based on 2D solids from analogous materials such as the transition metal dichalcogenides [19]. For example, monolayer MoS_2 has a direct band gap of about 1.8 eV and FET structures have been successfully fabricated from this solid, as discussed later in this chapter. As a result of the isolation of two-dimensional materials with a variety of electronic structures, it has been seen that they have promising applications in technology such as for phototransistors and batteries [22] and other areas such as cosmetics, catalysts and solid lubricants [22].

Layered van der Waals solids are a common class of crystalline structures that can be exfoliated as stable single layers. The general structure of 2D materials is of a series of covalently bound atomic layers held together via van der Waals forces. There are

a variety of techniques that can be used to exfoliate such materials, and they capable of being exfoliated into single or few layer platelets mechanically and chemically [22]. These type of methods rely on separating the layers from the bulk by overcoming the interlayer van der Waals interactions. As the thickness of these materials is reduced to a monolayer many of their properties, such as electronic structure [22] and, as a result, optical absorption [23] are modified from the bulk behaviour. Research has led to the emergence of many single-layer materials with distinct physical and electronic properties. This can be exemplified by several investigations of transition metal chalcogenides such as MoS_2, WS_2, Ti_2Se_2 and Bi_2Se_3 that can approach monolayer thicknesses [22]. Some materials, such as MoS_2, can undergo a transition from an indirect to a direct band gap semiconductor [22] as their thickness is reduced to a single layer, together with accompanying increases in photoluminescence and photoabsorption [22]. This transition enables the effective use of such materials in optoelectronics even if the properties of the bulk 'parent' are unsuitable for these applications.

In addition to two-dimensional materials produced by exfoliation of van der Waals solids, it is also possible to use epitaxial growth techniques to produce elemental counterparts to graphene such as, silicene and germanene [22]. Silicene was recently fabricated by physical vapour deposition of elemental silicon on a single-crystal silver foil [24]. It is expected to possess excellent physical and electronic properties for example, a band gap that can be opened by applying an electric field along with high mobility [22]. Similar approaches have been used to produce germanene [22] and stannene [25]. However, these materials require a supporting substrate (such as silver, iridium or zirconium diboride) to be stable, which limits their applications [24].

Elemental 2D materials can also form the basis of novel two-dimensional compounds. For example. germanane can be produced in a stable layered form through the hydrogenation of single layer germanene. Germanane is a silver black monolayer solid which does not require supporting substrate like silicene to be stable [22]. Bulk layered germanane is found to have a direct band gap of approximately 1.7 eV. Monolayer material delivers a strong optical photoluminescence about 1.35 eV [22] and theoretical calculations have shown that germanane has a direct band gap around 1.53 eV, which means that it is potentially an excellent material for the absorption layer in solar cells because due to the close coincidence of the band gap and the maximum in the solar spectrum at the Earth's surface. However, germanane is somewhat sensitive to temperature, with dehydrogenation occurring above 75 °C and the material becomes amorphous [22]. As the majority of transistors and solar cell devices need to be robust against elevated temperature [22], electronics made from germanane will be unstable. Therefore, this material is currently not suitable for such applications, even though it has unique features which may be exploited in the future.

1.1.4 Graphene production

1.1.4.1 Micromechanical cleavage

Graphene was first isolated by micromechanical exfoliation from bulk highly oriented/ordered pyrolytic graphite (HOPG) using adhesive tape. Micromechanical exfoliation carried out via adhesive/scotch tape involves the employment of a force roughly of the order of 300 nN μm^{-2} [26] to peel off graphene flakes from the bulk [1]. The resulting graphene flakes can then deposited onto substrates such as silicon wafers with an insulating silicon dioxide (SiO_2) layer, as shown in Figure 1.4(a). In this case, an appropriate choice of the thickness of the oxide layer creates interference effects which make feasible the observation of graphene single layer by optical microscopy. In such a manner pristine single layer and few layer graphene can be isolated and then utilized to, for example, examine the electronic characteristics of graphene. Micromechanical exfoliation is viewed as an effective route to produce high quality graphene with high mobility [26]; however, the time-consuming nature of the process, skill required, and limited yield of monolayer or few layer graphene means that this approach is not scalable. Moreover, the sheet size obtained by mechanical exfoliation is limited [27, 28]. It is for these reasons that other methods of producing graphene with the large areas have received attention.

1.1.4.2 Epitaxial growth on SiC via Si sublimation

Another method frequently used to produce graphene is thermal decomposition at the SiC(0001) surface [12, 30, 31, 32], where a SiC sample is annealed in vacuum at a high temperature ($\geq$1400 °C) leading to Si sublimation and graphitisation of the remaining carbon atoms to form graphene layers, see Figure 1.4(b). For electronic devices, graphene on insulating substrates such as glass, plastic foils, or SiO_2/Si wafers is required. Since SiC is a wide band-gap semiconductor in this case it is not required to transfer graphene to from the initial growth substrate [33, 34], reducing processing steps and the potential for damage or contamination. Whilst this method is straightforward, production of graphene on SiC is nonetheless highly expensive due to the cost of the silicon carbon substrate, the vacuum required and high temperature [35]. Furthermore, graphene quality is lower than that gained by micromechanical exfoliation of graphite [28, 36]. Therefore, although capable of producing large areas of graphene, this approach is only suited for mass production in niche applications.

1.1.4.3 Liquid Phase Exfoliation

Another method that can be used for exfoliate bulk layered materials into thin monolayer and few-layer platelets is liquid phase exfoliation. There are a number of variation upon this

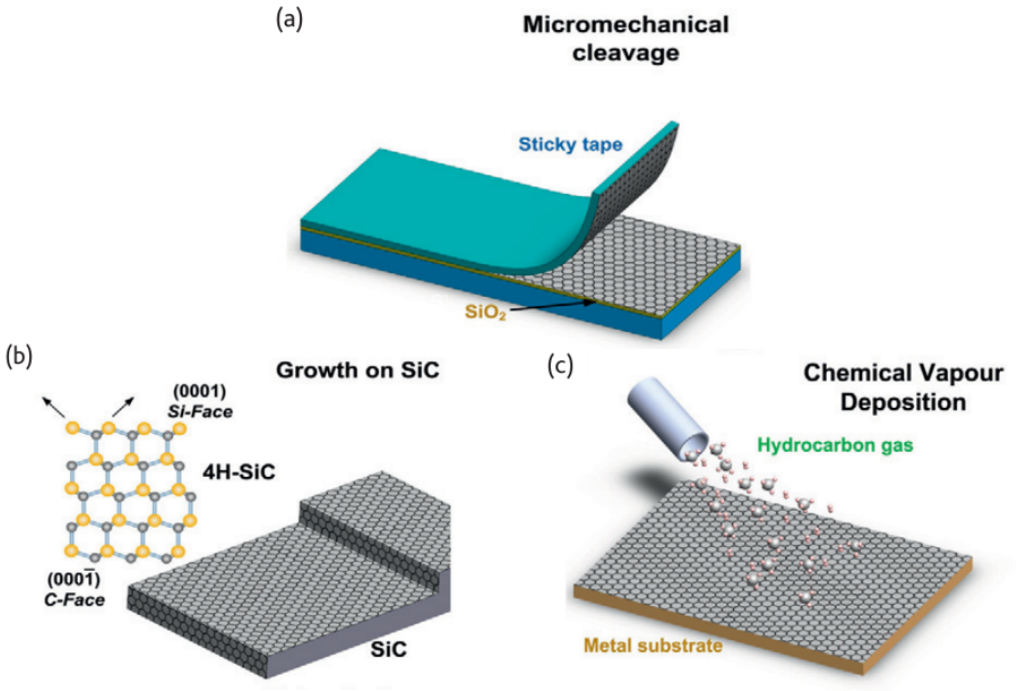

Figure 1.4: *Schematic showing graphene preparation techniques: (a) production of graphene by micromechanical cleavage; (b) growth of graphene on silicon carbide by sublimation of silicon atoms and graphitisation of the excess carbon atoms at the substrate surface; (c) growth of graphene by CVD on a metal foil with low carbon solubility [29].*

technique, but all require the input of external energy, through for example ultra-sonication or high shear forces to break the weak van der Waals interactions between layers and so exfoliated thin platelets of material. Separation techniques such as centrifuging can then be applied to separate the thinnest flakes for analysis, research or application. Perhaps the most straightforward of these techniques is the use of high shear mixing developed by Coleman's group [37] in which a specialist mixer is used to apply high shear forces to bulk flakes of graphene in a liquid phase. Typically the liquid phase is N-methyl-pyrrolidone (NMP), which is chosen as the interfacial surface energy between this liquid and the graphene is favourable, so preventing the graphene and few-layer graphene sheets re-stacking. An alternate approach to using a surface energy matched liquid phase which has been successfully demonstrated is to use a surfactant in combination with water [38].

1.1.4.4 Chemical Vapour Deposition

One of the most promising methods to synthesize high quality graphene with large area at an acceptable cost is chemical vapour deposition (CVD) [6, 39, 40, 41, 42], which is discussed in more detail in Chapters 2, 3 and 4. In this method, hydrocarbon precursors such as

methane decompose at high temperature at the surface of a catalytic metal substrate. If the metal has a significant carbon solubility at elevated temperature the carbon species will diffuse into the bulk of the metal and, upon cooling, these carbon atoms will diffuse out to the surface and form a single (or few) layer graphene film [41, 43, 44]. The disadvantage of using such metals is that it is extremely difficult to control the concentration of carbon in the metal and, in consequence, the thickness of the resulting graphene film. The use of a transition metal such as copper, which is possessed of a low carbon solubility can potentially overcome these problems. Graphene grown on copper substrates has long been viewed to be self-limiting as a result of carbon precursors being confined to the surface of the metal, resulting in the formation of homogeneous monolayer film [45]. However, as will be discussed in Chapter 4, we find that self-limiting growth occurs only under specific growth conditions even on copper substrates and that exposure to high precursor concentrations can lead to the formation of multilayers.

A complicating factor associated with CVD graphene growth is that the transfer of graphene onto insulating substrates is required for any electronics applications. Transfer of a graphene layer between substrates has drawbacks, e.g., creation of defects such as wrinkles, vacancies and impurities during the transfer process. Moreover, the graphene films obtained by CVD growth are polycrystalline [46] and contain numerous grain boundaries [46]. Grain boundaries have been found to have a negative impact on both mechanical [27] and transport [27] properties. They degrade, for example, electronic transport and so can limit device performance. Therefore, it is desirable to minimise the density of grain boundaries for fabrication of efficient graphene devices [47].

1.2 Transition Metal dichalcogenides (TMDCs)

As discussed above, since the discovery of graphene in 2004, other 2D layered materials such as transition metal dichalcogenides (TMDCs), transition metal oxides and other 2D materials such as BN, Bi_2Se_3 and Bi_2Te_3 have received much interest. Indeed, there are more than 40 different kinds of TMDCs alone [48]. TMDCs have applications in several areas such as catalysis, lubrication, and photovoltaics. Many belong to the class of layered compounds and their structures take the formula MX_2, in which (M) is a transition metal – most commonly molybdenum or tungsten (Mo or W) – sandwiched between two chalcogens (X) atoms – usually, sulphur, selenium or tellurium (S, Se, or Te) [49]. The thickness of each layer within these materials is about 0.65 nm. As with graphite, in the bulk these layered materials have a stacked structure, which involve strong covalent bonding in-plane within each layer, while the layers are held together by van der Waals forces. The transition metal atoms within layered TMDC crystals are surrounded by six chalcogen atoms.

TMDCs display a wide variety of electronic properties including insulating, metallic and semiconducting behaviour [48]. The most commonly studied TMDCs (MoS_2, WS_2, $MoSe_2$, and WSe_2) are semiconductors which have a band gap that evolves from indirect in the bulk to direct in single layers. These TMDCs naturally have band gaps in the range of 1-2 eV together with measured mobility generally of the order of 100 $cm^2\ V^{-1}\ s^{-1}$ at room temperature. This flexibility makes them potentially suitable for optoelectronic devices, for example.

MoS_2, has received the most attention among the metal dichalcogenides. A single layer MoS_2 is built up from layers comprising of a layer of Mo atoms sandwiched between two layers of S atoms, with the S and Mo atoms covalently bound [49]. The most commonly occurring (2H hexagonal) crystal structure is shown in Figure 1.5. In the MoS_2 unit cell Mo atoms are coordinated with six S atoms, and the S atoms coordinated to three Mo atoms [49]. In its bulk form MoS_2 is a semiconductor with an indirect band gap of around 1.2 eV. However, in ultrathin layers of MoS_2 photoluminescence has been observed despite its absence in the bulk material [50]. This photoluminescence has been found to increase as the sheet thickness decreases, and photoluminescence resulting from a monolayer is found to be the strongest. The cause of this change in behaviour is associated with a change from indirect to direct band gap behaviour with decreasing thickness, as will be discussed below. The presence of direct optical absorption/emission coupled with the relatively high channel mobility (200 $cm^2\ V^{-1}\ s^{-1}$) and large ON:OFF ratios (1×10^8) displayed by MoS_2 in field-effect transistors (FETs) make this material highly promising for phototransistors and photodetectors.

The electronic structure of a single MoS_2 triple layer (S-M-S) is discussed by Shaw [51] and can be described as follows: Bonding in MoS_2 requires S_sS_p and M_dM_s hybridization, and full occupation of the s and p shells of S. Thus, sulphur atoms are saturated resulting in the inertness between the MoS_2 layers [49]. All the TMDCs in group six have this same structure. The trigonal prismatic coordination of the metal splits its d-orbital, giving a rise to d_{z^2} orbitals with lower energy followed by two degenerate $d_{x^2-y^2}$ and d_{xy} orbitals, then two degenerate d_{xz} and d_{yz} orbitals with higher energies [48, 49]. From this description the band structure of a single layer of MoS_2, shown in Figure 1.6, can be understood. In the case of MoS_2, the lowest energy of the valence band is specified by the Mo-d, S-p hybridized bonding [49], followed by the non-bonding states d_{z^2}, d_{xy} and $d_{x^2-y^2}$ in the next highest energy level. In MoS_2, Mo and S has a formal charge of $+4$ and -2, respectively. Two d-electrons are left in the d_{z^2} orbitals in a d_2 configuration of Mo atom as seen in Figure 1.6a. Due to the two electrons that occupied d_{z^2} orbitals, there is an energy barrier to the next lowest unfilled state, Figure 1.6b.

The MoS_2 band structure can be calculated from first principles density functional

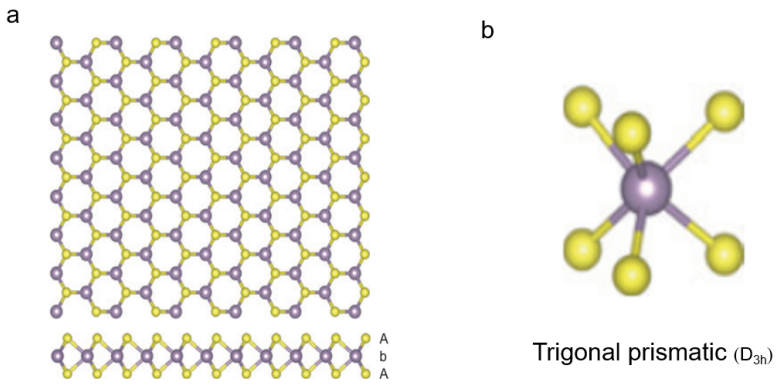

Figure 1.5: *(a) The structure of transition metal dichalcogenides (MX_2) in the 2H hexagonal trigonal prismatic crystal arrangement where a single layer in MX_2 is comprised of a metal atoms sandwiched between two chalcogen layers. (b) The trigonal prismatic structure of MX_2 with the metal atom, shown in purple, surrounded by chalcgen atoms shown in yellow [48].*

theory (DFT) to obtain additional understanding of its electronic structure. Figure 1.7 represents the MoS_2 band structures obatined for the bulk and mono-layer forms of MoS_2 [52]. As can be seen, MoS_2 in bulk form is a semiconductor with indirect band gap between the valence band maximum at the Γ point and the conduction band minimum, part way between Γ and K, of around 1.2 eV. Whereas, for an isolated two-dimensional monolayer sheet of the same material the band gap is direct and both valence band maximum and conduction band minimum are located at the K point, which lies at the corner of the two-dimensional Brillouin zone.

The changes that occur in the MoS_2 band structure with layer number originate from a change in hybridization between the d orbitals on the Mo atoms and p_z orbitals on the S atoms [53, 54, 55]. The bulk MoS_2 band structure shows that at the Γ-point, the upper state of the valence band originates from a combination of an orbital hybridisation between the d_{z^2} orbital on Mo and the p_z orbial on S. The energy of these interactions is strongly dependent on interlayer distance. The nature of these antibonding interactions is the reason that with increasing interlayer distance, such as in the case of isolating a single 2D layer, the valence band energy diminishes at Γ [49]. Conversely, the top of valence band and the bottom of the conduction band at the K-point consist of states derived from localized in-plane Mo-Mo d_{xy} and $d_{x^2-y^2}$ orbitals which do not alter when the number of layers decrease. It is independent of interlayer spacing since the Mo atoms are situated in the middle of the layer between two S atoms and are unaffected by interlayer interactions [53]. Thus, as the number layers reduces the gap between these two energy bands at K remain relatively constant at 1.8 eV [49]. Hence, a transition in electronic structure arises from an indirect gap of 1.2 eV

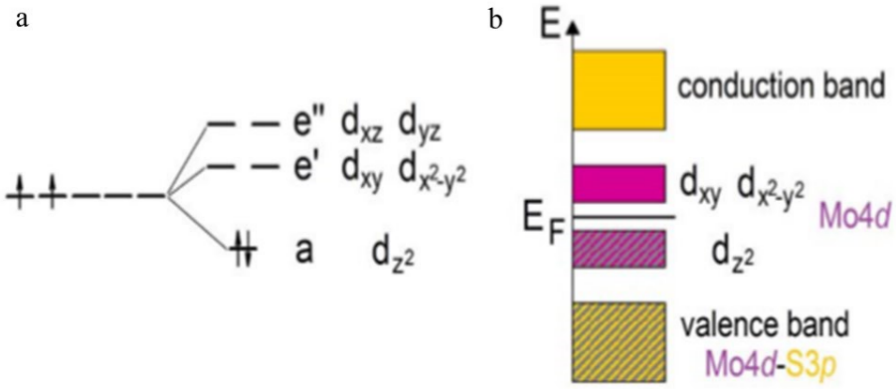

Figure 1.6: *(a) Electronic structure of d-transition metal dichalcogenide with a d_2 configuration of the metal atom in which the trigonal prismatic coordination splits the degenerate d-orbitals. (b) A schematic of the band structure for single layer MoS_2 with a gap between the orbitals d_{z^2} and d_{xy}, $d_{x^2-y^2}$ [49].*

to a 1.8 eV direct gap ($K \rightarrow K$) when the MoS_2 thickness is reduced down to a monolayer.

1.2.1 Preparation of monolayer and few-layer transition metal dichalcogenides

1.2.1.1 'Top-down' techniques

Many of the 'top-down' techniques for the production of monolayer and few layer TMDCs are similar to those employed for the production of graphene, discussed in section 1.1.4. Like graphene, layered TMDCs can be isolated into single-layers by using micromechanical cleavage. Such a mechanical exfoliation approach is a simple and effective method. Novoselov *et al.* separated 2D MoS_2 through rubbing the 3D bulk surface of a layered crystal [56]. A mixture of single and few layer MoS_2 flakes were found on the substrate. Single flakes, formed through applying the cleavage technique, have been described as highly crystalline and have high purity which make this approach suitable for the fabrication of devices which can enable the fundamental physical properties of this material to be explored [19, 53, 57]. However, as described above for the case of graphene, the micromechanical cleavage process is slow with the result that this technique is unsuitable for the large scale production of two-dimensional materials.

Liquid phase exfoliation (section 1.1.4.3) has been successfully used to exfoliate single and few-layers platelets from layered TMDCs such as MoS_2, $MoSe_2$, WS_2, $MoTe_2$ and h-BN in isopropanol (IPA) and N-methyl-pyrrolidone (NMP) as solvents [58]. Material consisting of monolayer and few-layer nanosheets were observed with lateral size of about 50 nm to 1000 nm. The disadvantages of liquid exfoliation the difficulty in making single-layer

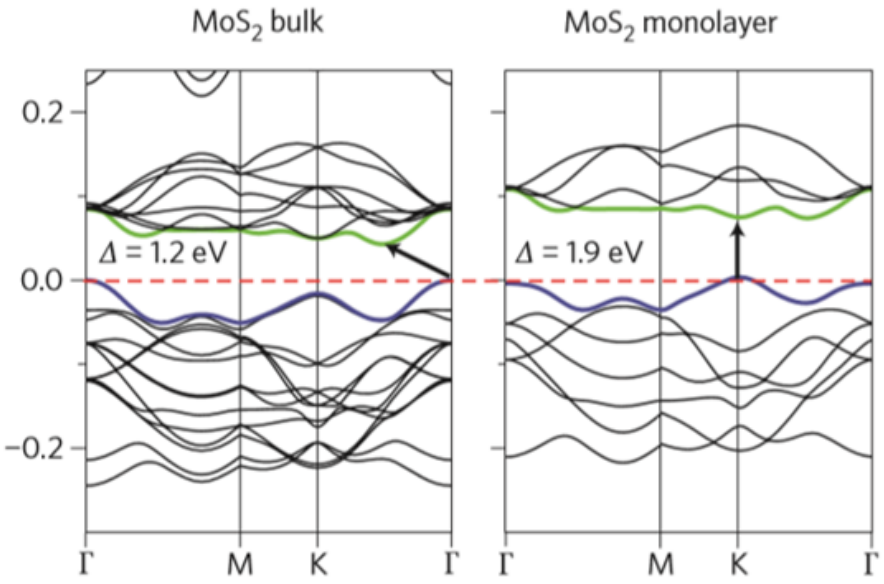

Figure 1.7: *Energy dispersion in bulk (left panel) and monolayer MoS_2 (right panel). The blue and green lines represent the valence band and the conduction bands, respectively. The solid arrows display the interband transitions associated with the fundamental gap and it can be seen that the transition is indirect in the bulk but direct in the monolayer [52].*

TMDC nanosheets, control over the size distribution and the controlled deposition of the nanosheets onto a suitable substrate. Thus, to utilize the unique electronic and optical properties of monolayer TMDC, approaches that can controllably produce very thin films is required.

1.2.1.2 'Bottom-up' techniques

Controllable deposition of TMDCs with the required number of layers of material on a chosen substrate can be achieved by 'bottom-up' methods. As mentioned before, the development of methods for producing graphene on a large scale through chemical vapour deposition (CVD) on metal substrates [59] and epitaxial growth on SiC substrates [60] has facilitated the fabrication of devices at large scale. Recently, synthesis of single layer MoS_2 sheets of large area has also been reported using several CVD-based methods [61, 52].

In CVD-based approaches for MoS_2 growth different solid powders such as MoO_3 and sulphur have been used as precursors, heated to a suitably high temperature to evaporate into an appropriate gas flow. These precursors either react in the gas phase and then deposited on a substrate or adosorb at the surface of the substrate and then react. In

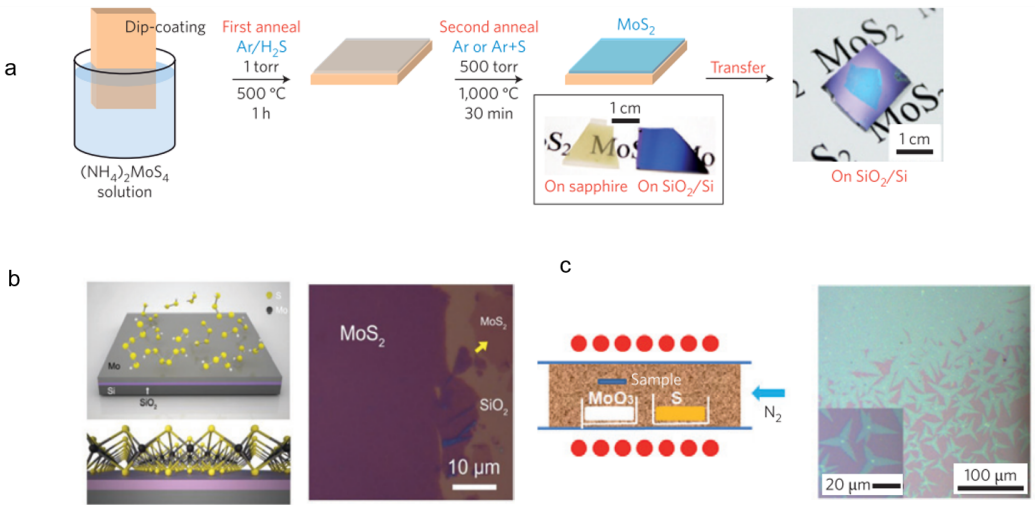

Figure 1.8: *Schematic methods for the preparation of monolayer and sub-monolayer MoS_2 films and their resulting structure: a) MoS_2 films are produced by high temperature treatment using a precursor dip-coated onto the substrate in the presence of Ar gas and S vapour; b) Growth of MoS_2 via deposition of a solid layer of Mo on SiO_2 followed by the direct sulphurization under sulfur vapour, the resulting MoS_2 film is shown in the right-hand panel; c) Schematic of CVD growth of MoS_2 using direct reaction between MoO_3 and S precursors (left) and resulting MoS_2 layers on SiO_2 (right) [52].*

both cases MoS_2 films of controllable coverage and thickness can be formed [62, 63]. This approach is discussed in detail in Chapters 2 and 3 and forms the basis of the results presented in Chapters 5 and 6, so here we focus on alternative, but closely-related methods of MoS_2 growth.

A number of 'bottom-up' approaches to the production of TMDCs have involved the treatment of layers of precursor materials deposited upon a substrate of choice. For example, it has been reported that MoS_2 layers can be produced on insulating substrates by dip-coating the substrate in ammonium thiomolybdate $(NH_4)_2MoS_4$ solution followed by a subsequent annealing at 500°C under an Ar/H_2 atmosphere which converted the surface thiomolybdates to MoS_2. Subsequent annealing under S vapour at high temperature was employed to further improve the MoS_2 crystal quality. This process is shown schematically in Figure 1.8a [61]. Lin and co-workers employed a similar method in which monolayer MoS_2 was obtained when thin MoO_3 films were deposited on a substrate and subsequently treated with S vapour [64]. Elemental Mo thin films can also be deposited on a substrate followed by the direct sulphurization under sulphur vapour, Figure 1.8b [65]. These growth methods are considered an efficient route of producing thin MoS_2 films with large area, however, control over thickness and uniformity is poor.

Lee *et al.* developed an alternative process for synthesizing single layer MoS_2 sheets using direct reaction between MoO_3 and S powders on a pretreated substrate [62]. Before CVD growth, the substrate was pretreated by exposure to a solution of reduced graphene oxide (rGO) to improve the growth of MoS_2 films. During the reaction the MoO_3 precursor was reduced by S vapor to MoO_{3-X} then diffused to the substrate and further treated with S to grow MoS_2 sheets. MoS_2 grew preferentially on the rGO and the resulting crystals had the form of three pointed stars with the film thickness of about 0.7 nm, corresponding to a single layer of material.

Plasma-enhanced [66] and laser-induced [67] deposition are other bottom up methods which have been used for producing MoS_2 films. MoS_2 can be grown at extremely low temperatures using plasma-enhanced chemical vapor deposition (PECVD). For example, Ahn *et al.* reported the direct deposition of MoS_2 on a plastic substrate at a temperature of 150–300°C. Initially, a thick layer of Mo is produced on the plastic substrate, which is then sulphurized in inert Ar plasma conditions. Raman spectroscopy and atomic force microscopy (AFM) showed that the deposited film had a few layers that were more than 3 nm thick. Loh and Chua used a laser to produce MoS_2 on a silver (Ag) metal substrate at 500°C. The resulting MoS_2 film is crystalline and can be as thin as two to three layers.

1.3 Van der Waals hetrostructures

As described above, each two-dimensional material may possess properties distinct from their 3D parent solid. Moreover, 2D materials provide further flexibility through the thickness dependence of their electronic properties [68]. Therefore, band gaps can be 'engineered' in a given semiconducting two-dimensional material through control of the number of layers in a sample. The result is that it is possible to create a wide variety of 'building blocks' by choosing different two-dimensional materials of controlled thickness with tailored physical properties which can then be combined in an artificial three-dimensional structure consisting of a stack of two-dimensional components. This concept is schematically illustrated in Figure 1.9. Since the forces binding the layers together are dominated by van der Waals interactions these structures are termed van der Waals hetrostructures (vdWHs) [68].

2D van der Waals hetrostructures do not require the lattice matching needed in a conventional hetrostructure due to the weak forces between layers. Van der Waals bonding possesses energies around 40-70 meV per atom in comparison with in-plane covalent bond energies of around 200-6000 meV [23]. Hence, 'epitaxy' of crystalline 2D materials on top of each other is possible without lattice matching due to the dominance of the in-plane bonds, which determine the layer structure. This is known as 'van der Waals epitaxy' and can be exploited for 2D layers of similar materials (known as homoepitaxy) or 2D layers of

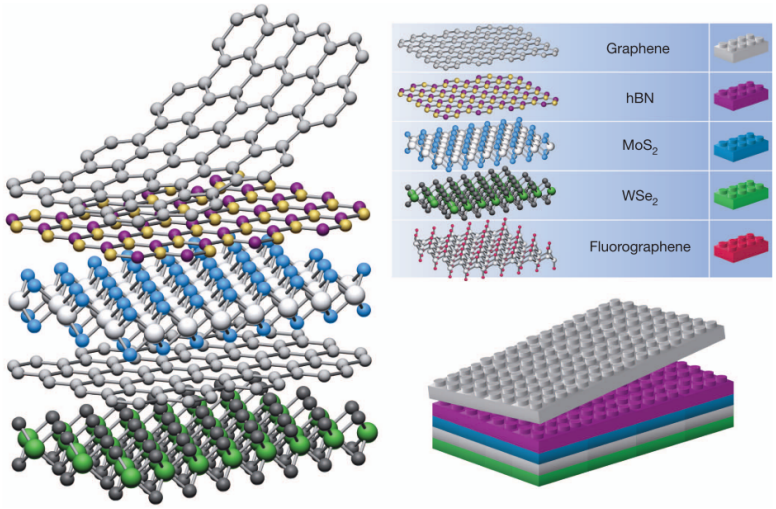

Figure 1.9: *A schematic illustration of the assembly of a vdW hetrostructure [68].*

varying materials (called heteroepitaxy). Thus, a form of 'epitaxy' is feasible even if there is substantial lattice difference between the layers, eliminating interfacial defects and their associated degradation of materials properties.

Whilst conventional hetrostructures compromise semiconductors only, in Van der Waals hetrostructures it is possible to stack semiconductors, (e.g. MoS_2) metals (e.g. graphene) and insulators (e.g. hexagonal boron nitride). The significant range of heterostructure functionalities possibly results in several feasible applications. Graphene can be grown on hBN to achieve graphene transistors with high mobility [69], and combining graphene as transparent electrodes with semiconducting layers has enabled the fabrication of light-emitting devices [69]. The combination of graphene with other members of the family of two-dimensional materials, such as transition metal dichalcogenides (TMDCs) and hexagonal (h-BN) can produce devices which are only a few atomic layers thick and stable mechanically. For example, Xu *et al.* [70] fabricated a transparent transistor from graphene and MoS_2 which has a high flexibly and photoresponsivity up to (10^4 mA W^{-1}). Georgiou and co-workers combined graphene and WS_2 into heterostructures to fabricate vertical field-effect tunneling transistors (FETTs). Not only was the resulting device appropriate for transparent and flexible electronics but also displayed high current on/off ratio through tunneling barriers in the WS_2 [71].

1.4 Aim of this study

This research aims to explore the growth of two-dimensional materials by low-cost atmospheric pressure chemical vapour deposition (AP-CVD), emphasising understanding key features of the growth process. Many techniques for producing high-quality graphene have been discovered. Still, growth from CVD on Cu substrates appears to be the most direct route to graphene-based electrical devices that can outperform their existing Si equivalents. As a result, optimising the growth of graphene from CVD on Cu is needed to guarantee the highest quality graphene. Therefore, we determined those processing parameters that should be kept consistent and found the most optimum condition for fabrication by varying numerous processing parameters. Further investigations aimed to examine parameters in graphene growth, particularly temperature, growth time, and surface pre-treatment before the deposition of hetero-layers is explored through CVD. Characterisation of the samples using Raman spectroscopy and SEM is used to assess the efficacy of the CVD process. In general, this CVD process applies to other two-dimensional materials. Given our success with graphene, this technique can be applied to other two-dimensional materials such as MoS_2.

Therefore, we also used CVD for synthesising MoS_2 layers because it involved the direct reaction of MoO_3 powder with S powder on untreated silicon substrates with native surface oxides. The MoS_2 growth mechanism we employ is the same as those previously reported in the existing literature. These studies looked at the effect of changing the MoO_3 and substrate temperatures but not the sulphur partial pressure, which is the primary emphasis of this chapter. The effect of sample temperature and growth time was investigated similarly to those investigated in the literature to discover 'baseline' parameters for MoS_2 monolayer and few-layer film growth and obtain insight into the growth mechanism. The impact of sulphur partial pressure (via vaporisation temperature) on MoS_2 growth is then investigated while the temperatures of MoO_3 and substrate remain constant. Although a decrease in MoS_2 coverage has previously been noted with rising sulphur growth temperatures in the literature, no reason for this occurrence has previously been proposed. Therefore, this chapter focuses on finding reasonable explanations for this phenomenon.

Finally, this thesis aims to show the CVD growth of MoS_2 on CVD-prepared graphene to create such heterostructures and the growth of MoS_2 on highly-oriented pyrolytic graphite (HOPG) as a model system. The findings highlight some of the issues that must be addressed if direct growth is to be used for vdWHS fabrication.

1.5 Organisation of Thesis

The remainder of this thesis is organised as follows: Chapter 2 outlines the theory behind the analytical techniques used to characterise the materials studied in this thesis; Chapter 3 presents the instruments and techniques used to acquire the data presented, along with

details of sample preparation; In Chapter 4, graphene is synthesised using the CVD method from a hydrocarbon precursor (methane), and the effects of precursor flow rate, growth temperature and substrate cleaning on the resulting graphene films are investigated; In Chapter 5, the synthesis of MoS_2 from MoO_3 and sulphur precursors using CVD is demonstrated, focusing on the effect of growth temperature and sulphur vapour pressure on the resultant MoS_2 films. In chapter 6, initial experiments to investigate the growth of MoS_2 on graphite, graphene/Cu and graphene 'paper' via CVD are described. Chapter 7 presents overall conclusions and outlines possible routes for future work which build on the results presented.

1.6 Summary

In this chapter, a brief introduction to graphene and the other members of the family of two-dimensional (2D) materials was provided. The structures and properties of graphene and 2D transition metal dichalcogenides (TMDCs) – with specific reference to MoS_2 – were described. Methods for preparation of graphene and MoS_2 and their relative advantages and disadvantages were discussed.

References

[1] Kostya S Novoselov, Andre K Geim, Sergei V Morozov, D Jiang, Y_ Zhang, Sergey V Dubonos, Irina V Grigorieva, and Alexandr A Firsov. Electric field effect in atomically thin carbon films. *Science*, 306(5696):666–669, 2004.

[2] Andre K Geim and Konstantin S Novoselov. The rise of graphene. In *Nanoscience and technology: a collection of reviews from nature journals*, pages 11–19. World Scientific, 2010.

[3] Philip Richard Wallace. The band theory of graphite. *Physical Review*, 71(9):622, 1947.

[4] Gang Hee Han, Fethullah Gunes, Jung Jun Bae, Eun Sung Kim, Seung Jin Chae, Hyeon-Jin Shin, Jae-Young Choi, Didier Pribat, and Young Hee Lee. Influence of copper morphology in forming nucleation seeds for graphene growth. *Nano Letters*, 11(10):4144–4148, 2011.

[5] Yimin A Wu, Ye Fan, Susannah Speller, Graham L Creeth, Jerzy T Sadowski, Kuang He, Alex W Robertson, Christopher S Allen, and Jamie H Warner. Large single crystals of graphene on melted copper using chemical vapor deposition. *ACS Nano*, 6(6):5010–5017, 2012.

[6] Xuesong Li, Weiwei Cai, Jinho An, Seyoung Kim, Junghyo Nah, Dongxing Yang, Richard Piner, Aruna Velamakanni, Inhwa Jung, Emanuel Tutuc, et al. Large-area synthesis of high-quality and uniform graphene films on copper foils. *Science*, 324(5932):1312–1314, 2009.

[7] AJ Van Bommel, JE Crombeen, and A Van Tooren. Leed and auger electron observations of the sic (0001) surface. *Surface Science*, 48(2):463–472, 1975.

[8] Taisuke Ohta, Aaron Bostwick, Thomas Seyller, Karsten Horn, and Eli Rotenberg. Controlling the electronic structure of bilayer graphene. *Science*, 313(5789):951–954, 2006.

[9] Luca Banszerus, Michael Schmitz, Stephan Engels, Jan Dauber, Martin Oellers, Federica Haupt, Kenji Watanabe, Takashi Taniguchi, Bernd Beschoten, and Christoph Stampfer. Ultrahigh-mobility graphene devices from chemical vapor deposition on reusable copper. *Science Advances*, 1(6):e1500222, 2015.

[10] Rahul Raveendran Nair, Peter Blake, Alexander N Grigorenko, Konstantin S Novoselov, Tim J Booth, Tobias Stauber, Nuno MR Peres, and Andre K Geim. Fine structure constant defines visual transparency of graphene. *Science*, 320(5881):1308–1308, 2008.

[11] Alexander A. Balandin, Suchismita Ghosh, Wenzhong Bao, Irene Calizo, Desalegne Teweldebrhan, Feng Miao, and Chun Ning Lau. Superior thermal conductivity of single-layer graphene. *Nano Letters*, 8(3):902–907, 2008. PMID: 18284217.

[12] Y-M Lin, Christos Dimitrakopoulos, Keith A Jenkins, Damon B Farmer, H-Y Chiu, Alfred Grill, and Ph Avouris. 100-ghz transistors from wafer-scale epitaxial graphene. *Science*, 327(5966):662–662, 2010.

[13] Sukanta De and Jonathan N Coleman. Are there fundamental limitations on the sheet resistance and transmittance of thin graphene films? *ACS Nano*, 4(5):2713–2720, 2010.

[14] Kostya S Novoselov, D Jiang, F Schedin, TJ Booth, VV Khotkevich, SV Morozov, and Andre K Geim. Two-dimensional atomic crystals. *Proceedings of the National Academy of Sciences*, 102(30):10451–10453, 2005.

[15] L Britnell, RV Gorbachev, R Jalil, BD Belle, F Schedin, A Mishchenko, T Georgiou, MI Katsnelson, L Eaves, SV Morozov, et al. Field-effect tunneling transistor based on vertical graphene heterostructures. *Science*, 335(6071):947–950, 2012.

[16] Thanasis Georgiou, Rashid Jalil, Branson D Belle, Liam Britnell, Roman V Gorbachev, Sergey V Morozov, Yong-Jin Kim, Ali Gholinia, Sarah J Haigh, Oleg Makarovsky, et al. Vertical field-effect transistor based on graphene–WS_2 heterostructures for flexible and transparent electronics. *Nature Nanotechnology*, 8(2):100–103, 2013.

[17] AH Castro Neto, Francisco Guinea, Nuno MR Peres, Kostya S Novoselov, and Andre K Geim. The electronic properties of graphene. *Reviews of Modern Physics*, 81(1):109, 2009.

[18] LM Malard, Marcos Assunção Pimenta, Gene Dresselhaus, and MS Dresselhaus. Raman spectroscopy in graphene. *Physics Reports*, 473(5-6):51–87, 2009.

[19] Branimir Radisavljevic, Michael Brian Whitwick, and Andras Kis. Integrated circuits and logic operations based on single-layer MoS_2. *ACS Nano*, 5(12):9934–9938, 2011.

[20] Young-Woo Son, Marvin L Cohen, and Steven G Louie. Erratum: Energy gaps in graphene nanoribbons [phys. rev. lett. 97, 216803 (2006)]. *Physical Review Letters*, 98(8):089901, 2007.

[21] Melinda Y Han, Barbaros Özyilmaz, Yuanbo Zhang, and Philip Kim. Energy band-gap engineering of graphene nanoribbons. *Physical Review Letters*, 98(20):206805, 2007.

[22] Kristie J Koski and Yi Cui. The new skinny in two-dimensional nanomaterials. *ACS Nano*, 7(5):3739–3743, 2013.

[23] Sheneve Z Butler, Shawna M Hollen, Linyou Cao, Yi Cui, Jay A Gupta, Humberto R Gutiérrez, Tony F Heinz, Seung Sae Hong, Jiaxing Huang, Ariel F Ismach, et al. Progress, challenges, and opportunities in two-dimensional materials beyond graphene. *ACS Nano*, 7(4):2898–2926, 2013.

[24] Geoff Brumfiel. Sticky problem snares wonder material. *Nature*, 495(7440):152–153, 2013.

[25] Sivacarendran Balendhran, Sumeet Walia, Hussein Nili, Sharath Sriram, and Madhu Bhaskaran. Elemental analogues of graphene: silicene, germanene, stanene, and phosphorene. *Small*, 11(6):640–652, 2015.

[26] Yuanbo Zhang, Joshua P Small, William V Pontius, and Philip Kim. Fabrication and electric-field-dependent transport measurements of mesoscopic graphite devices. *Applied Physics Letters*, 86(7):073104, 2005.

[27] Cecilia Mattevi, Hokwon Kim, and Manish Chhowalla. A review of chemical vapour deposition of graphene on copper. *Journal of Materials Chemistry*, 21(10):3324–3334, 2011.

[28] Konstantin S Novoselov, VI Fal, L Colombo, PR Gellert, MG Schwab, K Kim, et al. A roadmap for graphene. *Nature*, 490(7419):192–200, 2012.

[29] Francesco Bonaccorso, Antonio Lombardo, Tawfique Hasan, Zhipei Sun, Luigi Colombo, and Andrea C Ferrari. Production and processing of graphene and 2d crystals. *Materials Today*, 15(12):564–589, 2012.

[30] Walt A De Heer, Claire Berger, Xiaosong Wu, Phillip N First, Edward H Conrad, Xuebin Li, Tianbo Li, Michael Sprinkle, Joanna Hass, Marcin L Sadowski, et al. Epitaxial graphene. *Solid State Communications*, 143(1-2):92–100, 2007.

[31] G. H. Wells, T. Hopf, K. V. Vassilevski, E. Escobedo-Cousin, N. G. Wright, A. B. Horsfall, J. P. Goss, A. G. O'Neill, and M. R. C. Hunt. Determination of the adhesion energy of graphene on sic(0001) via measurement of pleat defects. *Applied Physics Letters*, 105(19), 2014.

[32] T. Hopf, K. V. Vassilevski, E. Escobedo-Cousin, P. J. King, N. G. Wright, A. G. O'Neill, A. B. Horsfall, J. P. Goss, G. H. Wells, and M. R. C. Hunt. Dirac point and transconductance of top-gated graphene field-effect transistors operating at elevated temperature. *Journal of Applied Physics*, 116(15), 2014.

[33] Bharati Gupta, Marco Notarianni, Niraj Mishra, Mahnaz Shafiei, Francesca Iacopi, and Nunzio Motta. Evolution of epitaxial graphene layers on 3C SiC/Si (1 1 1) as a function of annealing temperature in UHV. *Carbon*, 68:563–572, 2014.

[34] Walt A De Heer, Claire Berger, Ming Ruan, Mike Sprinkle, Xuebin Li, Yike Hu, Baiqian Zhang, John Hankinson, and Edward Conrad. Large area and structured epitaxial graphene produced by confinement controlled sublimation of silicon carbide. *Proceedings of the National Academy of Sciences*, 108(41):16900–16905, 2011.

[35] J Leclercq and P Sveshtarov. The transfer of graphene: A review. *Bulgarian Journal of Physics*, 43(2), 2016.

[36] Kinam Kim, Jae-Young Choi, Taek Kim, Seong-Ho Cho, and Hyun-Jong Chung. A role for graphene in silicon-based semiconductor devices. *Nature*, 479(7373):338–344, 2011.

[37] K. R. Paton, E. Varrla, C. Backes, R. J. Smith, U. Khan, A. O'Neill, C. Boland, M. Lotya, O. M. Istrate, P. King, T. Higgins, S. Barwich, P. May, P. Puczkarski, I. Ahmed, M. Moebius, H. Pettersson, E. Long, J. Coelho, S. E. O'Brien, E. K. McGuire, B. M. Sanchez, G. S. Duesberg, N. McEvoy, T. J. Pennycook, C. Downing, A. Crossley, V. Nicolosi, and J. N. Coleman. Scalable production of large quantities of defect-free few-layer graphene by shear exfoliation in liquids. *Nature Materials*, 13(6):624–30, 2010.

[38] M. Lotya, P. J. King, U. Khan, S. De, and J. N. Coleman. High-concentration, surfactant-stabilized graphene dispersions. *Acs Nano*, 4(6):3155–3162, 2010. 612hu Times Cited:486 Cited References Count:38.

[39] Sukang Bae, Hyeongkeun Kim, Youngbin Lee, Xiangfan Xu, Jae-Sung Park, Yi Zheng, Jayakumar Balakrishnan, Tian Lei, Hye Ri Kim, Young Il Song, et al. Roll-to-roll production of 30-inch graphene films for transparent electrodes. *Nature Nanotechnology*, 5(8):574–578, 2010.

[40] Gedeng Ruan, Zhengzong Sun, Zhiwei Peng, and James M Tour. Growth of graphene from food, insects, and waste. *ACS Nano*, 5(9):7601–7607, 2011.

[41] Qingkai Yu, Jie Lian, Sujitra Siriponglert, Hao Li, Yong P Chen, and Shin-Shem Pei. Graphene segregated on ni surfaces and transferred to insulators. *Applied Physics Letters*, 93(11):113103, 2008.

[42] Alfonso Reina, Xiaoting Jia, John Ho, Daniel Nezich, Hyungbin Son, Vladimir Bulovic, Mildred S Dresselhaus, and Jing Kong. Large area, few-layer graphene films on arbitrary substrates by chemical vapor deposition. *Nano Letters*, 9(1):30–35, 2009.

[43] Xuesong Li, Weiwei Cai, Luigi Colombo, and Rodney S Ruoff. Evolution of graphene growth on ni and cu by carbon isotope labeling. *Nano Letters*, 9(12):4268–4272, 2009.

[44] E Starodub, S Maier, I Stass, NC Bartelt, PJ Feibelman, M Salmeron, and KF McCarty. Graphene growth by metal etching on ru (0001). *Physical Review B*, 80(23):235422, 2009.

[45] Kiyeol Lee and Jongpil Ye. Significantly improved thickness uniformity of graphene monolayers grown by chemical vapor deposition by texture and morphology control of the copper foil substrate. *Carbon*, 100:441–449, 2016.

[46] Qingkai Yu, Luis A Jauregui, Wei Wu, Robert Colby, Jifa Tian, Zhihua Su, Helin Cao, Zhihong Liu, Deepak Pandey, Dongguang Wei, et al. Control and characterization of individual grains and grain boundaries in graphene grown by chemical vapour deposition. *Nature Materials*, 10(6):443–449, 2011.

[47] Pierre Trinsoutrot, Caroline Rabot, Hugues Vergnes, Alexandru Delamoreanu, Aziz Zenasni, and Brigitte Caussat. High quality graphene synthesized by atmospheric pressure CVD on copper foil. *Surface and Coatings Technology*, 230:87–92, 2013.

[48] Manish Chhowalla, Hyeon Suk Shin, Goki Eda, Lain-Jong Li, Kian Ping Loh, and Hua Zhang. The chemistry of two-dimensional layered transition metal dichalcogenide nanosheets. *Nature Chemistry*, 5(4):263, 2013.

[49] AN Enyashin and Gotthard Seifert. Electronic properties of MoS_2 monolayer and related structures. *Nanosystems: Physics, Chemistry, Mathematics*, 5(4):517–539, 2014.

[50] Andrea Splendiani, Liang Sun, Yuanbo Zhang, Tianshu Li, Jonghwan Kim, Chi-Yung Chim, Giulia Galli, and Feng Wang. Emerging photoluminescence in monolayer MoS_2. *Nano Letters*, 10(4):1271–1275, 2010.

[51] Jonathan Caplette Shaw. *Direct Synthesis of Semiconducting Transition Metal Dichalcogenide Monolayers and Heterojunctions by Chemical Vapor Deposition*. University of California, Los Angeles, 2016.

[52] Qing Hua Wang, Kourosh Kalantar-Zadeh, Andras Kis, Jonathan N Coleman, and Michael S Strano. Electronics and optoelectronics of two-dimensional transition metal dichalcogenides. *Nature Nanotechnology*, 7(11):699–712, 2012.

[53] Andrea Splendiani, Liang Sun, Yuanbo Zhang, Tianshu Li, Jonghwan Kim, Chi-Yung Chim, Giulia Galli, and Feng Wang. Emerging photoluminescence in monolayer MoS_2. *Nano Letters*, 10(4):1271–1275, 2010.

[54] Tianshu Li and Giulia Galli. Electronic properties of MoS_2 nanoparticles. *The Journal of Physical Chemistry C*, 111(44):16192–16196, 2007.

[55] Kin Fai Mak, Changgu Lee, James Hone, Jie Shan, and Tony F Heinz. Atomically thin MoS_2: a new direct-gap semiconductor. *Physical Review Letters*, 105(13):136805, 2010.

[56] Kostya S Novoselov, D Jiang, F Schedin, TJ Booth, VV Khotkevich, SV Morozov, and Andre K Geim. Two-dimensional atomic crystals. *Proceedings of the National Academy of Sciences*, 102(30):10451–10453, 2005.

[57] Anthony Ayari, Enrique Cobas, Ololade Ogundadegbe, and Michael S Fuhrer. Realization and electrical characterization of ultrathin crystals of layered transition-metal dichalcogenides. *Journal of Applied Physics*, 101(1):014507, 2007.

[58] Jonathan N Coleman, Mustafa Lotya, Arlene O'Neill, Shane D Bergin, Paul J King, Umar Khan, Karen Young, Alexandre Gaucher, Sukanta De, Ronan J Smith, et al. Two-dimensional nanosheets produced by liquid exfoliation of layered materials. *Science*, 331(6017):568–571, 2011.

[59] Xuesong Li, Weiwei Cai, Jinho An, Seyoung Kim, Junghyo Nah, Dongxing Yang, Richard Piner, Aruna Velamakanni, Inhwa Jung, Emanuel Tutuc, et al. Large-area synthesis of high-quality and uniform graphene films on copper foils. *Science*, 324(5932):1312–1314, 2009.

[60] J Hass, WA De Heer, and EH Conrad. The growth and morphology of epitaxial multilayer graphene. *Journal of Physics: Condensed Matter*, 20(32):323202, 2008.

[61] Keng-Ku Liu, Wenjing Zhang, Yi-Hsien Lee, Yu-Chuan Lin, Mu-Tung Chang, Ching-Yuan Su, Chia-Seng Chang, Hai Li, Yumeng Shi, Hua Zhang, et al. Growth of large-area and highly crystalline MoS_2 thin layers on insulating substrates. *Nano Letters*, 12(3):1538–1544, 2012.

[62] Yi-Hsien Lee, Xin-Quan Zhang, Wenjing Zhang, Mu-Tung Chang, Cheng-Te Lin, Kai-Di Chang, Ya-Chu Yu, Jacob Tse-Wei Wang, Chia-Seng Chang, Lain-Jong Li, et al. Synthesis of large-area MoS_2 atomic layers with chemical vapor deposition. *Advanced Materials*, 24(17):2320–2325, 2012.

[63] Sivacarendran Balendhran, Jian Zhen Ou, Madhu Bhaskaran, Sharath Sriram, Samuel Ippolito, Zoran Vasic, Eugene Kats, Suresh Bhargava, Serge Zhuiykov, and Kourosh Kalantar-Zadeh. Atomically thin layers of MoS_2 via a two step thermal evaporation–exfoliation method. *Nanoscale*, 4(2):461–466, 2012.

[64] Yu-Chuan Lin, Wenjing Zhang, Jing-Kai Huang, Keng-Ku Liu, Yi-Hsien Lee, Chi-Te Liang, Chih-Wei Chu, and Lain-Jong Li. Wafer-scale mos_2 thin layers prepared by MoO_3 sulfurization. *Nanoscale*, 4(20):6637–6641, 2012.

[65] Yongjie Zhan, Zheng Liu, Sina Najmaei, Pulickel M Ajayan, and Jun Lou. Large-area vapor-phase growth and characterization of MoS_2 atomic layers on a SiO_2 substrate. *Small*, 8(7):966–971, 2012.

[66] Chisung Ahn, Jinhwan Lee, Hyeong-U Kim, Hunyoung Bark, Minhwan Jeon, Gyeong Hee Ryu, Zonghoon Lee, Geun Young Yeom, Kwangsu Kim, Jaehyuck Jung, et al. Low-temperature synthesis of large-scale molybdenum disulfide thin films directly on a plastic substrate using plasma-enhanced chemical vapor deposition. *Advanced Materials*, 27(35):5223–5229, 2015.

[67] Tamie AJ Loh and Daniel HC Chua. Growth mechanism of pulsed laser fabricated few-layer MoS_2 on metal substrates. *ACS Applied Materials & Interfaces*, 6(18):15966–15971, 2014.

[68] Andre K Geim and Irina V Grigorieva. Van der waals heterostructures. *Nature*, 499(7459):419–425, 2013.

[69] KS Novoselov, A Mishchenko, A Carvalho, and AH Castro Neto. 2D materials and van der waals heterostructures. *Science*, 353(6298), 2016.

[70] Hua Xu, Juanxia Wu, Qingliang Feng, Nannan Mao, Chunming Wang, and Jin Zhang. High responsivity and gate tunable graphene-MoS_2 hybrid phototransistor. *Small*, 10(11):2300–2306, 2014.

[71] Thanasis Georgiou, Rashid Jalil, Branson D Belle, Liam Britnell, Roman V Gorbachev, Sergey V Morozov, Yong-Jin Kim, Ali Gholinia, Sarah J Haigh, Oleg Makarovsky, et al. Vertical field-effect transistor based on graphene–WS_2 heterostructures for flexible and transparent electronics. *Nature Nanotechnology*, 8(2):100, 2013.

Chapter 2

Experimental Techniques

This chapter outlines the theory behind the analytical techniques used to characterise the materials studied in this thesis. Materials characterisation methods include the study of crystal structure, bonding and composition using Raman spectroscopy (RS), examination of morphology using scanning electron microscopy (SEM) and the study of elemental composition and chemical state with X-ray photoelectron spectroscopy (XPS). The chapter also discusses sample preparation approaches, in particular production of graphene and MoS_2 samples by atmospheric pressure chemical vapour deposition (APCVD).

2.1 Chemical Vapour Deposition (CVD)

2.1.1 Introduction

Chemical vapour deposition (CVD) can be defined as the deposition of a thin solid film on a heated substrate from the vapour phase by a chemical reaction of precursors [1]. This process requires the use of a vapour-transfer process with atoms or molecules as the deposition material. The advantage of CVD over other thin film deposition techniques is that it can produce homogenous, high quality films with controllable thickness. Moreover, a CVD system is easy to design and can be constructed using equipment and precursors with low-cost and the results can be quickly and reliably obtained. In general, a CVD system consists of a method of transport of precursors required for deposition, a reaction chamber in which the precursors are decomposed, and a system for exhausting reaction products and unreacted precursors.

CVD has different ways to initiate the decomposition of reactants within the system. In its simplest terms, the fabrication of thin films is a result of decomposition of precursors near, or on, the substrate surface activated by thermal energy, the deposition temperature often being over 900 °C. For temperature-sensitive substrates other forms of energy input are required to avoid damaging the substrate. Reduced growth temperatures can be achieved by using plasma-enhanced CVD (PECVD) which facilitates deposition at very low temperature (300 °C or even at room temperature) [2]. In this deposition technique electrical energy is used rather than thermal energy, inducing a plasma which activates the precursor to produce active ions followed by further chemical reaction which results in film formation on the substrate surface [3]. Photo-assisted CVD is another method used for deposition of thin layers on a surface, which applies a focused beam of light radiation to induce reactions in the precursor(s) in the gas phase or on the growth surface [4]. CVD can be performed at both low pressure and atmospheric pressure. The latter is selected for this work for its simplicity and the absence of a need for expensive equipment.

2.1.2 CVD process

The basic steps of a simplified CVD process are illustrated in Figure 2.1. First, precursor(s) are transported by bulk gas flow to the furnace reactor. If the precursors are solids under normal laboratory conditions this step also involves their heating and evaporation, often into an inert gas flow. The precursors then diffuse into the main region of the reactor and reactions may take place on the substrate surface, resulting in the formation of reactive intermediates and gases. Reactive intermediates may then diffuse over the surface to form island nuclei. Depending on the quantity of the precursors and growth time, the islands

increase in size through the addition of further reactive species and can coalesce together at their boundaries until a continuous film is formed. Finally, any unreacted precursor and/or volatile byproducts will desorb and diffuse away from the surface [2].

A variation on this process uses reactive precursors in the gas phase, such that precursor decomposition at the substrate surface is not required. Although this process is sometimes known as Chemical Vapour Transport, it is more often also known as CVD and is the terminology used in this thesis.

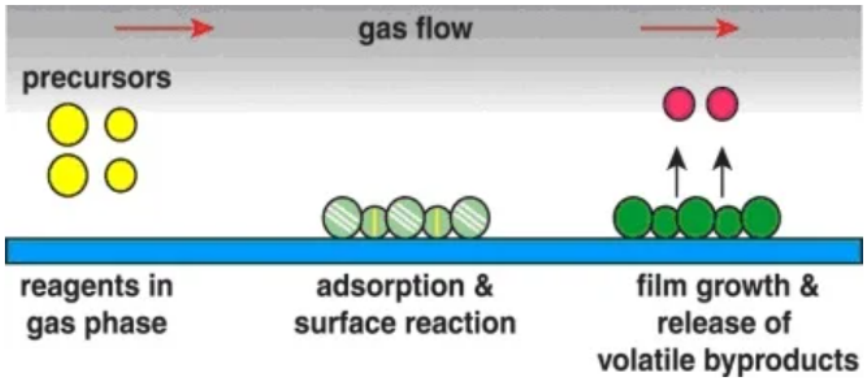

Figure 2.1: *A schematic diagram of the steps required in CVD growth of thin films. The reactant gases are introduced to the system and then react on the surface followed by diffusion to nucleation sites on the substrate surface and desorption of byproducts and unreacted species [5].*

In a thermal CVD process, the precursor is subject to a sufficiently high temperature to allow its decomposition, resulting in desired product being deposited on the sample surface. In CVD, growth parameters such as furnace temperature, substrate, precursor flow and growth time all can be controlled during the experiment. Thermal reactors used in the CVD process can be either hot wall or cold-wall [6]. In a hot wall reactor the entire reaction chamber is heated with the substrate and therefore, a large volume of the substrate can be covered. In a cold-wall reactor only the substrate is heated. Although the concentration of contamination is less when using a cold-wall reactor [6], a hot-wall reactor was chosen for growing thin film in this project due to its simplicity of use and the fine control of deposition parameters. Figure 2.2 (a) demonstrates a horizontal tube reactor in which the deposition region and the substrate is placed inside a tube furnace and (b) a horizontal reactor in which the sample is mounted on top of a heater stage.

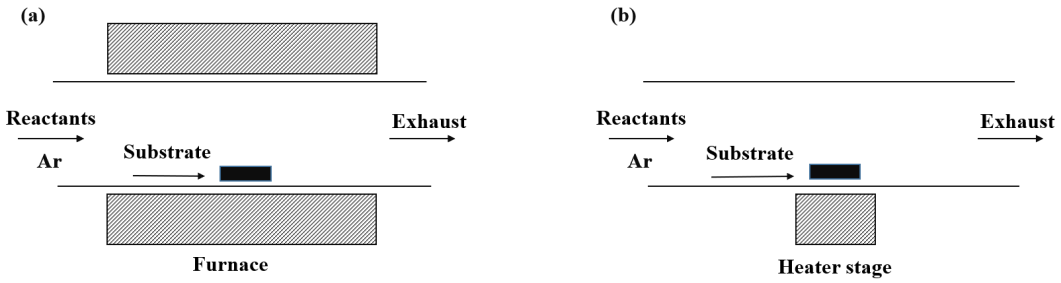

Figure 2.2: *A horizontal hot-wall CVD reactor (a) and a horizontal cold-wall reactor (b). Adapted from [6]*

2.2 Sample Characterisation

2.2.1 Raman spectroscopy

Raman spectroscopy is a powerful, non-destructive analytical tool which can be used to provide insight into the physical and chemical structure of molecules and solids [7]. The Raman technique is based on the inelastic scattering of a photon by a molecule or a solid and the measurement of the wavelength/energy of the scattered photon. In a Raman experiment light of fixed wavelength, most commonly generated by a laser, is focused on to a sample of interest. The incident photon can be either elastically or inelastically scattered by the vibrational modes of the sample (phonons when considering a solid). In the case of inelastic scattering, the photon will have a different frequency (or, equivalently, energy) – such photons are said to have undergone Raman scattering. The shift in energy of the scattered photon is measured and provides information regarding the vibrations/phonons of the system.

Raman scattering can be divided into two types: *resonant* and *non-resonant*. Non resonant Raman scattering is a form of inelastic scattering that can be defined as absorption and immediate re-emission (although in practice it is a single, coherent process). In this process an electron within a molecule or solid is promoted to a virtual energy state (one which is sufficiently short-lived not to violate the Heisenberg Uncertainty Principle) as this state decays there is a probability that the final state may involve vibrational excitation or de-excitation of the system [7, 8].

If the energy of the final state of the molecule or solid is the same as the initial state, the scattering of the photon is elastic, which is known as *Rayleigh scattering*. However, in Raman scattering, the final vibrational state has different energy from the initial state, and possesses either higher or lower energy. If the energy of the final state is greater than

the energy of the initial state, the scattered light will lose energy, a process which is called *Stokes scattering*. If, instead, the energy of the final vibrational state is lower than intially, the scattered light will gain energy and this mode of scattering is known as *Anti-Stokes* Raman scattering. The elastic and inelastic scattering processes mentioned are illustrated in Figure 2.3. Therefore, a Raman spectrum can be constructed by measuring the difference in energy of the scattered photon with respect to that of the incident photon.

Raman scattering has a very weak intensity as most scattered photons undergo Rayleigh scattering. However, the intensity of scattered light can be increased under certain 'resonant' conditions. Resonance Raman (RR) scattering occurs in a similar way to that in non-resonant Raman scattering. However, in the resonant case, the frequency of the incident photon is close to (or equal) to the frequency of an electronic transition in the molecule or solid. This enables the electron to gain enough energy to move it to a higher energy electronic state rather than a virtual one, resulting in an increase in Raman intensity. Both non-resonance and Resonance Raman (RR) scattering are illustrated in the energy level diagram in Figure 2.3.

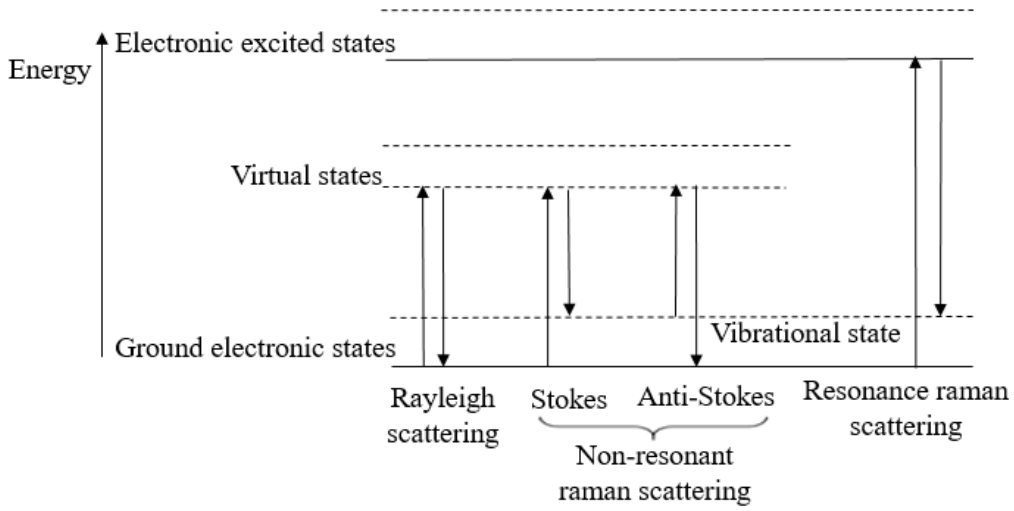

Figure 2.3: *Energy level diagram illustrating non-resonant Rayleigh, Stokes and Anti-Stokes scattering and Resonance Stokes Scattering [7].*

Raman scattering can be understood from the viewpoint of classical electromagnetism if we consider a phonon which has an associated time varying polarisation:

$$\mathbf{p} = \alpha \mathbf{E} \cos(\omega t), \tag{2.1}$$

where $\mathbf{p}$ is the local dipole moment per unit volume (polarisation) in the lattice due to the vibration considered, and α is the local *polarisability*. $\mathbf{E}$ is the incident electric field, oscillating at frequency ω and t is time.

Let us assume that the vibration leads to a time varying local polarisability:

$$\alpha = \alpha_0 + \Delta\alpha \cos(\Omega t), \tag{2.2}$$

where Ω is the vibrational frequency of the phonon, α_0 is the static polarisability and $\Delta\alpha$ is the amplitude of the change in polarisability arising from that phonon mode.

Hence,

$$\mathbf{p} = (\alpha_0 + \Delta\alpha \cos(\Omega t))\mathbf{E} \cos(\omega t), \tag{2.3}$$

And thus

$$\mathbf{p} = \alpha_0 \mathbf{E} \cos(\omega t) + \frac{\Delta\alpha}{2}\mathbf{E}(\cos(\omega - \Omega)t + \cos(\omega + \Omega)t). \tag{2.4}$$

The first term is the elastic *Rayleigh scattering*. However, the two components at lower and higher frequency are associated with *Stokes* and *anti-Stokes* Raman scattering. Hence Raman-active vibrations/phonons are those which possess a time-varying local polarisability.

2.2.1.1 Raman spectra of graphene

Raman spectroscopy is a fast and ideal tool for graphene characterization [9]. In addition to the non-destructive nature of this technique (and the lack of any requirement for specialist sample preparation), Raman scattering from graphene has the distinct advantage of presenting a strong signal. The strength of the Raman scattering signal originates from the resonant scattering processes described above, which enables even a monolayer of graphene to be readily investigated [9, 10]. Due to the sensitivity of the Raman active modes in graphene and it's few-layer analogues to a variety of physical properties, the technique can be used to determine the number of graphene layers, crystallite size, quality of the sample, the effect of doping, chemical impurities, defects and the general structure of graphene samples [10]. In this study, Raman spectroscopy is applied to all graphene samples to identify the thickness of graphene layers grown by Chemical Vapour Deposition (CVD) and the relative density of defects.

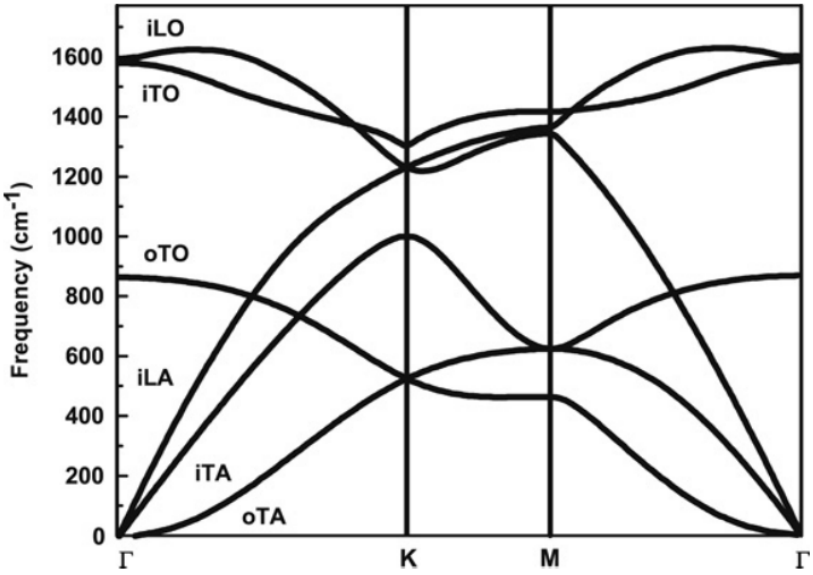

Figure 2.4: *Phonon dispersion relation of graphene, showing all six phonon modes [9].*

A knowledge of the phonon dispersion relation for graphene is important in order to understand its Raman spectrum. The unit cell of graphene consists of two carbon atoms, A and B, and are situated at inequivalent sites within the two-dimensional graphene lattice [11], and hence there will be six phonon dispersion branches (a result of the three degrees of freedom of motion for each atom) [9], as seen in Figure 2.4. Three of these branches are acoustic (A) and the other three are optic (O). When the vibrations of two carbon atoms are in phase, the phonon is categorised as an acoustic mode (A), but out of phase oscillations produce optical phonons (O). One acoustic and one optic branch occur when the atomic oscillations are perpendicular to the graphene plane, thus, these modes relate to out- of- plane (o) phonon branches. Two acoustic and two optic phonon modes relate to in-plane (i) vibrations. Traditionally, it is necessary to consider the vibrations in terms of the direction of the nearest carbon-carbon bond, thus, the phonon modes are categorized as longitudinal L, or transverse T modes, depending on if the oscillations are parallel or perpendicular to those bonds. Therefore, the dispersion curves are assigned to LO, iTO, oTO, LA, iTA and oTA phonon branches, as can be seen in Figure 2.4.

The most noticeable feature in the Raman spectra of graphene are the so-called D, G and $G^{'}$ bands (the latter sometimes known as the $2D$ band due to it being approximately twice the D band frequency) [9], Figure 2.5. The G band, which occurs at approximately 1580 cm^{-1}, is associated with the two doubly degenerate iTO and LO phonon modes, Figure 2.4 at the centre of the Brillouin zone, Γ. The vibration arises due to a first-order Raman transition involving absorption and emission of phonons as seen in Figure 2.6(a).

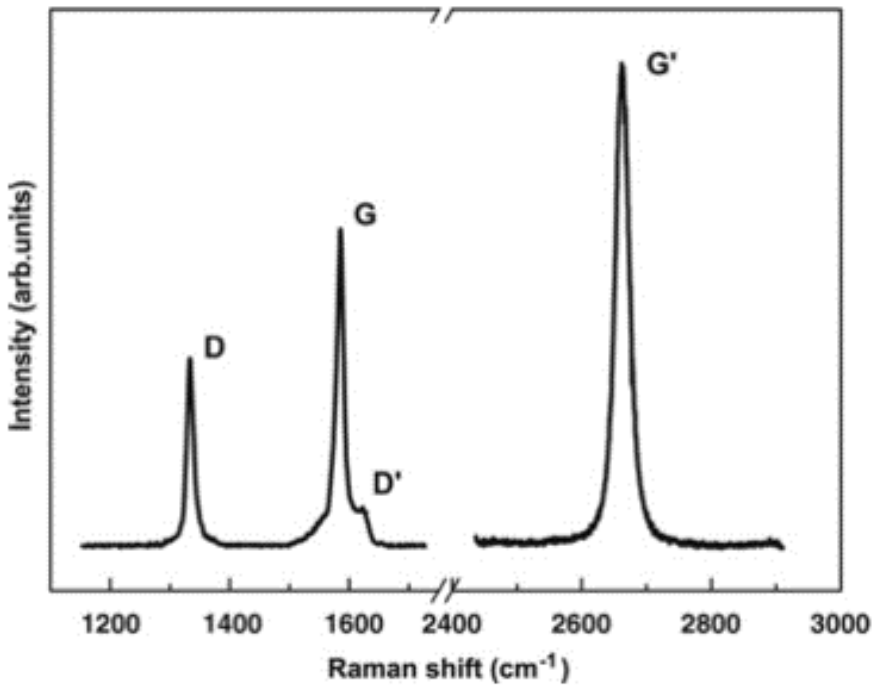

Figure 2.5: *Raman spectrum of graphene [9].*

In contrast, the D and $G^{'}$ peaks, which are located at around 1350 cm^{-1} and 2700 cm^{-1}, respectively, arise from what is known as a *double resonance* (DR) process. For the $2D$ peak, this process involves the following steps: An electron close to a K-point in the graphene Brillouin Zone (BZ) absorbs an incident photon which is then scattered inelastically from an iTO phonon to a point on a circle around Dirac point located at $K^{'}$ within the BZ. The electron is then inelastically scattered back to the original region of the BZ by another iTO phonon. Finally the excited states decays, emitting a photon by the excited electron recombining with a hole, as illustrated by Figure 2.6(b). For the case of the D peak, we see that there is a different DR process, which involves an excited electron elastically scattered by a defect of the crystal (which can be anything which lowers symmetry, such as a vacancy, edge or impurity), subsequently followed by inelastic scattering by an iTO phonon, Figure 2.6(c).

2.2.1.2 Raman spectra of MoS_2

Bulk, crystalline MoS_2 possesses four Raman-active vibrational modes, labelled by their symmetry symbols E_{1g}, E^1_{2g}, E^2_{2g} and A_{1g}, as illustrated in Figure 2.7. The two modes E_{1g} and E^2_{2g} correspond to the relative movement of the two-dimensional layers with respect to one another and have low frequency [12] due to the weak inter-planar van der

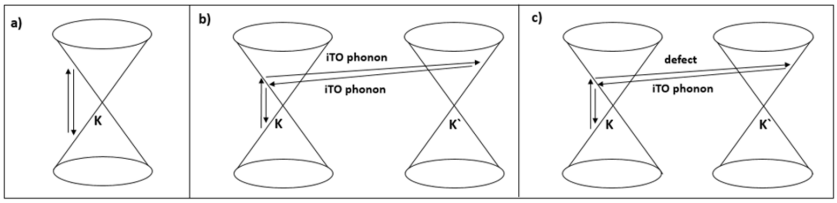

Figure 2.6: *a) First order G band Raman scattering process from an iTO and iLO phonon. b) 2D band second order DR process involving inelastic scattering from two iTO phonons at Dirac points K and K′. c) D band DR process, which originates from elastic scattering by a defect at the K point followed by inelastic scattering from a phonon at the K′ point. Adapted from [9].*

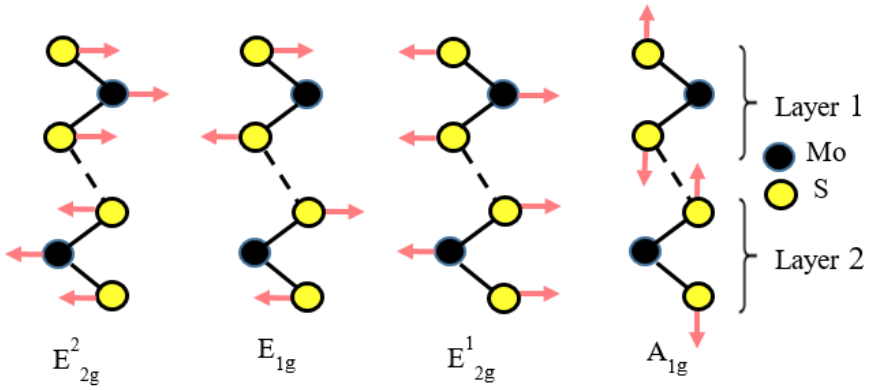

Figure 2.7: *Atomic vibrations in MoS_2 bulk crystal for the four Raman-active modes in the unit cell. Adapted from [12].*

Waals bonds in this material (Chapter 1). The other two, prominent, Raman modes are associated with in-plane (E^1_{2g}) and and out-of-plane (A_{1g}) modes within a single layer. These two modes can be used to characterise the thickness of an MoS_2 sample since, at least for mechanically exfoliated samples [12], they show a well defined dependence with the number of layers in the sample. As the number of layers in a sample increases from a single layer upwards, the A_{1g} mode undergoes a blueshift (move to higher frequency), while the E^1_{2g} mode suffers a redshift (shift to lower frequency). For MoS_2 samples which contain four or more layers the frequencies of these two modes will meet the value of the bulk (and cannot therefore be distinguished from bulk materials by this approach). In principle this behaviour offers a means for the determination layer thickness of samples. Therefore in this thesis we limit our discussion to E^1_{2g} and A_{1g} modes of vibrations.

In order to understand the variation in the frequency of these two modes in single and few layer MoS_2 short and long range interaction terms need to be considered. For the E^1_{2g} mode, from Figure 2.7, it can be seen that the sulphur atoms of different sheets move

in-plane but in opposite directions (out of phase), and thus the frequency of this mode reduces with the number of layers due to a reduction in long range Coulomb interactions. On the other hand, in the A_{1g} mode, the sulphur atoms vibrate in phase with sulphur on neighbouring layers, and therefore, the short range term increases due to the weak interlayer interaction, which lead to an increase of the A_{1g} mode frequency with the number of layers. However, whilst the position of the Raman modes for mechanically exfoliated MoS_2 provide a good measure of the number of layers in a sample [12], this does not appear to be the case for material grown by CVD [13].

2.2.2 Scanning electron microscopy (SEM)

A Scanning Electron Microscope (SEM) allows the microstructure of a solid to be revealed by scanning the specimen surface with a narrowly-focused electron beam (with energy typically in the range of $\sim 1 - 30$ keV [14]. A SEM comprises an electron gun and a stack of electromagnetic lenses and apertures, as shown in Figure 2.8 [15]. The electron beam emitted from the gun is demagnified by a condenser lens and then focused to a specific diameter by the objective lens. Deflection plates enable the beam to be scanned over the surface in a raster scan pattern and the image is built up using signals gathered from the interaction between the beam and the specimen. A high-vacuum environment is needed in SEM to allow electrons to travel without being scattered by the specimen environment and to avoid contamination.

2.2.2.1 Electron-sample interactions

In SEM an image is produced by elastic and inelastic interactions between the electron beam and specimen atoms. Elastic scattering is caused by the interaction between the incident electron and either the atomic nucleus or outer shell electrons of the sample. In some cases the incident beam direction changes by more than 90° with negligible energy loss. The electron returns back to the surface of the specimen and escapes with the majority of its energy. This process is called backscattering and the electrons escaping the specimen are known as backscattered electrons (BSE). Inelastic scattering is a result of interactions between the primary beam and the atomic electrons of the specimen. This process requires a transfer of energy from the primary beam electrons to the atom. The excitation of the electron in the specimen during the interaction generates what are called secondary electrons (SE), which have less energy than the primary beam. In general, microscopists define secondary electrons as those with an energy less than ~ 50 eV. In addition to BSE and SE, when an electron beam hits the sample other signals such as X-ray emission, Auger electrons, and cathodoluminescence are also produced [14]. Although these signals form the basis of powerful analytical tools, the intensities obtained from the monolayer

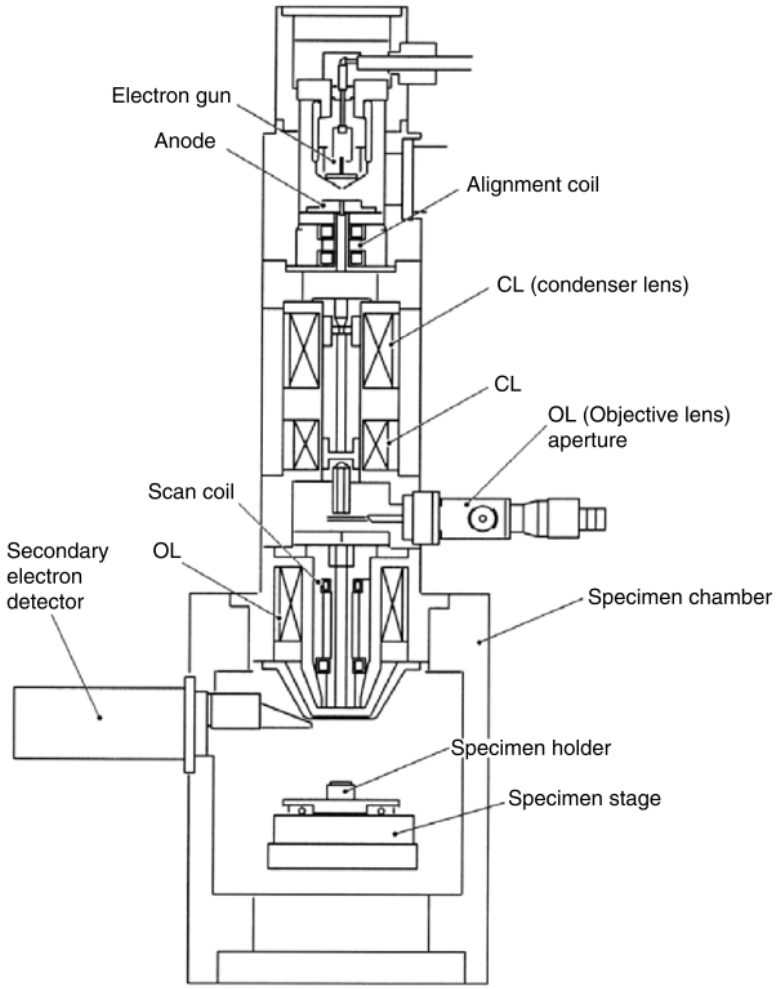

Figure 2.8: *Schematic of a scanning electron microscope (SEM) [14].*

and few-layer films examined in this thesis with the apparatus available are insufficient for sample characterisation and hence they will not be considered further.

When the primary beam hits the surface of the sample, electrons can travel for some distance inside the sample, producing an interaction region beneath the surface from which of the above-mentioned signals are generated. The depth of interaction volume generated by the incident beam increases with beam energy and decreases with specimen atomic number. The interaction volume has the shape of a hemisphere for specimens with high atomic numbers and a "tear drop" for specimens with low atomic numbers. This sample-beam interaction volume is shown in Figure 2.9 with different modes of scattering being produced from different depths within the sample [14, 16].

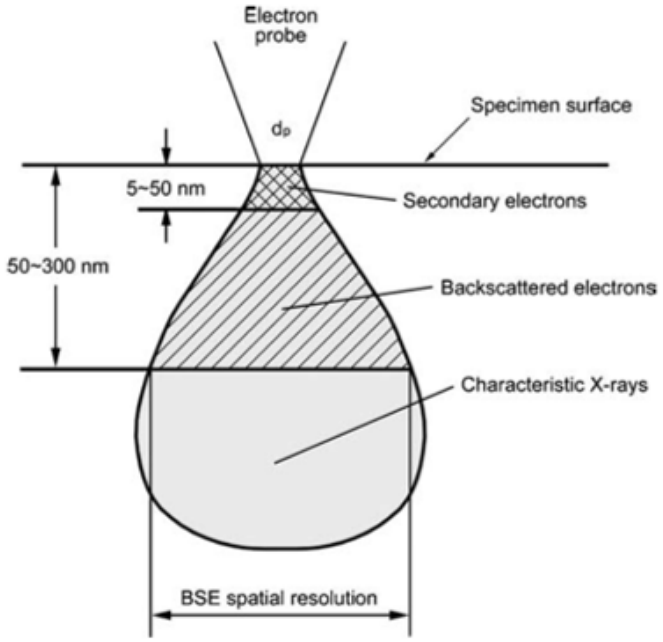

Figure 2.9: *The interaction volume of an incident electron beam with a specimen showing the origin of the various signals produced [14].*

2.2.2.2 Secondary Electron (SE) imaging

Inelastic scattering arises when electrons from the incident beam ionize specimen atoms resulting in loosely bound electrons leaving the sample, a process known as Secondary Electron (SE) emission. Secondary electrons have energies of less than ~ 50 eV and as such can only escape from regions close to the surface. Hence, secondary electrons are mainly used for topographic imaging. Figure 2.10 illustrates how the secondary electron intensity reaching a detector is influenced the sample surface topography [14, 16]. It can be seen that secondary electron emission from the edges of topographic features is much stronger than that from flat regions. Therefore, by scanning the primary electron beam over the surface and plotting the secondary electron intensity as a function of beam position a topographic image of the sample can be built up.

2.2.2.3 Back Scattered Electron (BSE) Imaging

Back Scattered Electrons (BSEs) are a direct result of the (quasi-) elastic scattering of primary beam electrons by specimen atoms. This kind of scattering is characterised by a small energy loss and a large scattering angle which re-directs the electrons back from the surface of sample, so enabling them to escape. Since the energy of BSEs is near to that of the incident electron beam, they can escape from deep in within the

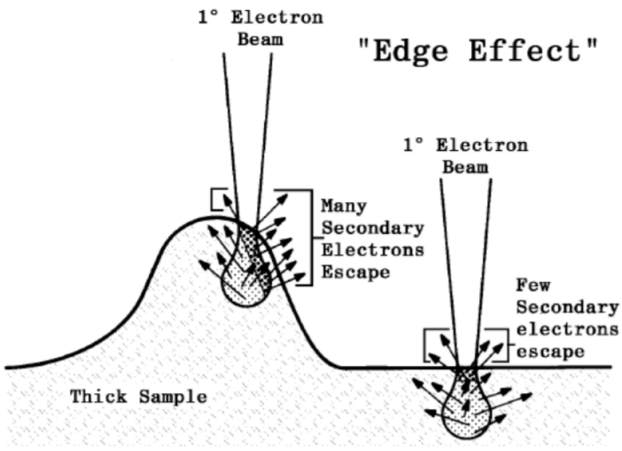

Figure 2.10: *The effect of surface topography on secondary electron detection. Secondary electrons are generated in greater number from the edges of raised topographical features of the sample in comparison with a flat surface [16].*

interaction volume, with depths typically ranging from 50 to 300 nm below the surface. The efficiency of back scattering, and thus the BSE signal, is dependent on the atomic number (Z) of the material; thus, BSEs can provide information about chemical composition variation across the sample [14]: an area with elements of a higher atomic number (Z) will generate more back scattered electrons and appear brighter in a SEM image.

2.2.3 X-ray Photoelectron Spectroscopy

X-ray Photoelectron Spectroscopy (XPS), also known as electron spectroscopy for chemical analysis (ESCA), is considered an excellent technique for surface analysis [17, 18, 19]. It can be used for a wide range of materials to provide information about the elemental composition and chemical state of the surface being analysed. Such information may be qualitative or, with the appropriate calibration and/or the use of reference samples, quantitative.

The principle of XPS, as shown in Figure 2.11, involves an (x-ray) photon impinging on a material, it is absorbed and then an electron is emitted from the surface with kinetic energy (E_K) given by:

$$E_K = h\nu - BE, \tag{2.5}$$

where $h\nu$ is the energy of the incident photon, and BE is the binding energy of the energy level in the atom, with respect to an appropriate reference, from which the electron is ejected. The reference is usually the Fermi energy in a metal, valence band maximum in a semiconductor or the vacuum level in the case of an insulator [19].

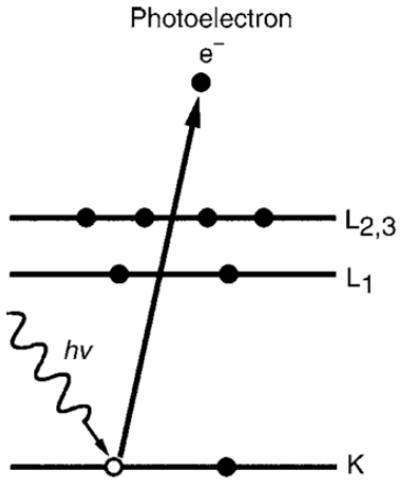

Figure 2.11: *The photoemission process in XPS. An incident X-ray is absorbed by an electron, ejecting it from the atom [14].*

As this equation illustrates, the kinetic energy, (E_K), is equal to the difference in energy between the binding energy (BE) and that of the incident light ($h\nu$). The energy of the X-ray is known, so it is possible to measure the energy of the emitted electron, allowing the binding energy to be calculated [14, 20]. A typical XPS spectrum plots the number of photoelectrons versus their binding energy. The peaks in the spectra represent the distribution of electrons in the sample. The collected spectra represent only species at the sample surface (to a depth of $\sim$ 2-10 nm, sometimes known as the 'selvedge' [17]) because the detected photoelectrons are only able to escape from outermost surface layers of a sample without experiencing inelastic scattering. Figure 2.12 shows the 'universal curve' of the mean free path of an electron (λ), in nm, as a function of the electron kinetic energy. When an incident photon is absorbed by electron, the excited electron can travel some distance in the solid and may scatter many times before leaving the surface. The inelastic mean free path (IMFP) is the average distance that a photoelectron can travel through the material without losing energy. Therefore, λ represents the depth sensitivity of the instrument being used, with $\sim 95\%$ of the signal originating from a depth of $\leq 3\lambda$.

A typical XPS instrument is illustrated in Figure 2.13 and comprises of a photon source and an electron analyser. The photons can be generated by a number of sources with Mg K_α or Al K_α x-ray sources most common in a laboratory context since these produce relatively narrow x-ray lines with small satellites (which may be further improved by monochromation) and the targets used to produce the x-rays are inexpensive and robust. A spherical electron analyser which comprises a lens column, concentric hemispheres and an electron detector [20] is the most usual apparatus for measuring the energy distribution

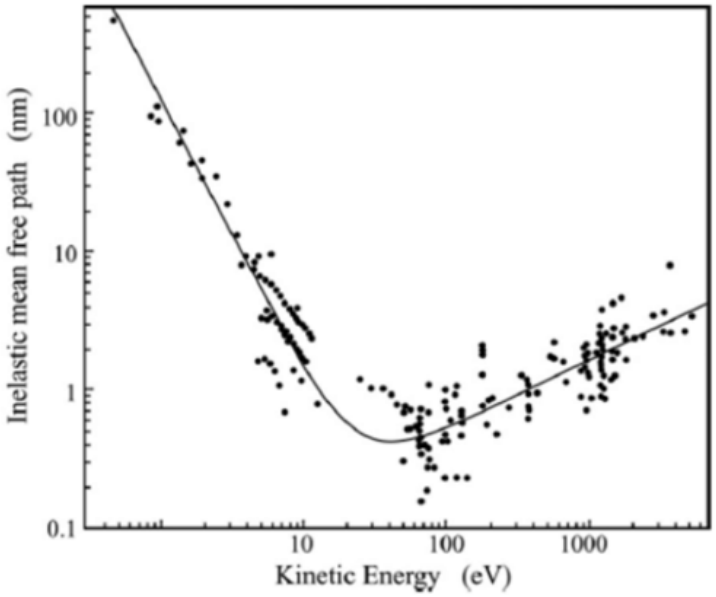

Figure 2.12: *The 'universal curve' of inelastic mean free path (IMFP) of electrons in a solid as a function of their kinetic energy for different elements [21].*

of the photoemitted electrons and is used to acquire the data presented in this thesis, but other types of electron analyser are occasionally employed [17]. An emitted photoelectron passes through a focusing lens to create a narrow, collimated beam, a retarding lens to decelerate the electron and then passes into the hemispherical analyser. This analyser contains two charged co-hemispherical plates and allows only electrons within a narrow energy range to pass through. Electrons with too small energy hit the inner plate and those with too high energy collide with the outer plate [22]. The narrow range of energies (the pass energy) allowed into the detector, gives an excellent spectral resolution. The electron analyser, sample and often the source are housed in an ultra-high vacuum system, which is required to create a clean environment for the sample and the instrument during the measurement and also to enable electrons to reach the detector without inelastic scattering

A typical XPS spectrum consists of a number of clearly defined peaks associated with core levels of the atoms present in the near-surface region of the sample, along with Auger electron peaks and, at very low binding energy, associated with the valence states of the sample. Since atomic core levels have well-defined binding energies, the simplest application of XPS is to determine which atomic species are present in the near surface region of the sample from the peaks present. However, as discussed below, XPS has the potential to obtain far deeper insight into the nature of a sample [23].

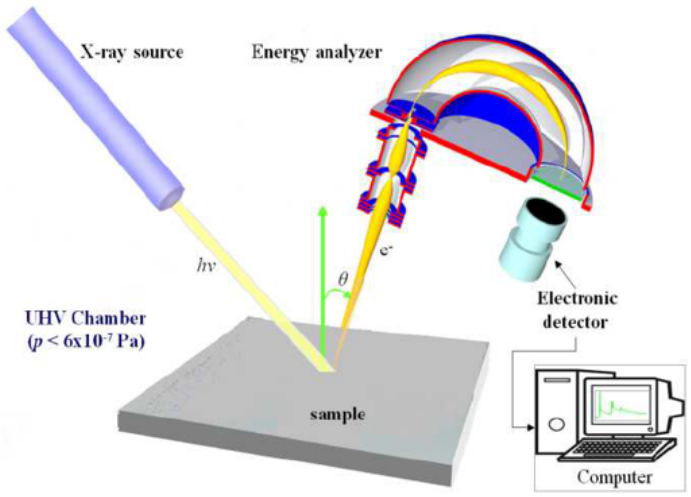

Figure 2.13: *A diagram showing the basic components of an XPS instrument [20].*

2.2.3.1 Chemical shift

In XPS, information can be obtained on chemical state from the variation in atomic core-level binding energy with chemical environment (the chemical shift) of the photoelectron peaks. The chemical shift is small in comparison with the electron binding energy and is caused by the change in local chemical environment or oxidation state such that an element bonded to electropositive species has a core-level line which is shifted down by up to a few eV in binding energy while those bonded to electronegative species are usually shifted up in energy [22]. An example of chemical shift in a core line is provided by the $1s$ levels in lithium metal and lithium oxide, as shown in Figure 2.14. In lithium oxide each Li atom donates its $2s$ electron almost totally into the $2p$ orbital of oxygen. Although, the $2s$ level is higher in energy than the $1s$ there is still some probability density of this state lying within the 'boundary' of the $1s$ orbital, screening the latter from the nucleus. Thus, when the $2s$ electron is transferred from the Li atom, the $1s$ electron feels a greater attraction to the nucleus, resulting in a higher binding energy than the same electron in Li metal [23]. This difference in binding energy between the Li metal and Li_2O can be seen clearly in the $1s$ photoelectron spectrum as illustrated in Figure 2.14.

2.2.3.2 Quantitative analysis

XPS can be used as a quantitative technique, to determine the elemental concentration of different species in the near surface region of a sample, under the assumption that there is either no depth dependence in composition or that the depth dependence is known by some other means. In XPS quantification [20, 19], The XPS spectrum of material has peaks

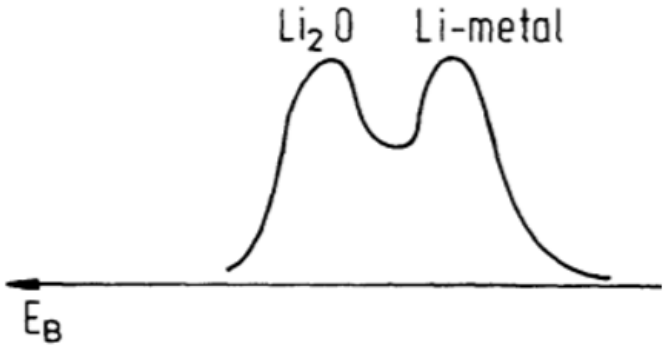

Figure 2.14: *A diagram showing the chemical shift in Li metal and Li_2O. The Li 1s line in Li_2O shifts to higher binding energy, in comparison with that of Li metal [23].*

that correspond to different elements. The area under these peaks is proportional to the element's concentration. The percentage of each element can be determined by measuring the peak areas and adjusting them for proper instrumental factors. This is based on the following equation of photoelectron line intensity:

$$I_{ij} = T(E)L_{ij}\sigma_{ij}N_i\lambda(E)\cos\theta \tag{2.6}$$

where I_{ij} is the intensity of a photoelectric peak (or the area) for a given element, $T(E)$ transmission function at the energy E of the electron passing through the analyzer, L_{ij} is the orbital asymmetry factor, σ_{ij} is the cross-section for photoionization of the atomic orbital of interest, $N_i(z)$ is the concentration of the element at depth z below the surface, $\lambda(E)$ is the photoelectron mean free path in the sample at energy E and θ is the angular efficiency factor for the instrumental arrangement based on the angle between the photon path and detected electron.

In XPS, the intensity can be calculated from the area of the peak after subtracting an appropriate inelastic background, usually a Shirley or Tougaard type background [24]. From the equation above we can easily calculate elemental concentration N_i as follows:

$$N_i = \frac{I_{ij}}{T(E)L_{ij}\sigma_{ij}\lambda(E)\cos\theta}. \tag{2.7}$$

If we consider the elements in the material to be homogeneously distributed through its near surface region, then the percentage concentration of each element can be given by:

$$\%n_i = \frac{N_i}{\sum n_i} * 100, \tag{2.8}$$

where $\%n_i$ is the atomic percent of any element in a sample.

References

[1] Hugh O Pierson. *Handbook of Chemical Vapor Deposition: principles, technology and applications*. William Andrew, 1999.

[2] Anthony C Jones and Michael L Hitchman. Overview of Chemical Vapour Deposition. *Chemical Vapour Deposition: Precursors, Processes and Applications*, pages 1–36, 2009.

[3] Chisung Ahn, Jinhwan Lee, Hyeong-U Kim, Hunyoung Bark, Minhwan Jeon, Gyeong Hee Ryu, Zonghoon Lee, Geun Young Yeom, Kwangsu Kim, Jaehyuck Jung, et al. Low-temperature synthesis of large-scale molybdenum disulfide thin films directly on a plastic substrate using plasma-enhanced chemical vapor deposition. *Advanced Materials*, 27(35):5223–5229, 2015.

[4] Tamie AJ Loh and Daniel HC Chua. Growth mechanism of pulsed laser fabricated few-layer MoS_2 on metal substrates. *ACS Applied Materials & Interfaces*, 6(18):15966–15971, 2014.

[5] ACZ Nano. Applications of Metal Halide Precursors in CVD/ALD Processes. www.azonano.com/article.aspx?ArticleID=3432, 16/06/2022.

[6] JR Creighton and P Ho. Introduction to Chemical Vapor Deposition (CVD). *Chemical vapor deposition*, 2:1–22, 2001.

[7] Ewen Smith and Geoffrey Dent. *Modern Raman Spectroscopy: A Practical Approach*. Wiley, 2019.

[8] John R Ferraro. *Introductory Raman Spectroscopy*. Elsevier, 2003.

[9] LM Malard, Marcos Assunção Pimenta, Gene Dresselhaus, and MS Dresselhaus. Raman spectroscopy in graphene. *Physics Reports*, 473(5-6):51–87, 2009.

[10] Mildred S Dresselhaus, Ado Jorio, Mario Hofmann, Gene Dresselhaus, and Riichiro Saito. Perspectives on carbon nanotubes and graphene raman spectroscopy. *Nano Letters*, 10(3):751–758, 2010.

[11] AH Castro Neto, Francisco Guinea, Nuno MR Peres, Kostya S Novoselov, and Andre K Geim. The electronic properties of graphene. *Reviews of Modern Physics*, 81(1):109, 2009.

[12] Changgu Lee, Hugen Yan, Louis E Brus, Tony F Heinz, James Hone, and Sunmin Ryu. Anomalous lattice vibrations of single-and few-layer MoS_2. *ACS Nano*, 4(5):2695–2700, 2010.

[13] William M Parkin, Adrian Balan, Liangbo Liang, Paul Masih Das, Michael Lamparski, Carl H Naylor, Julio A Rodríguez-Manzo, AT Charlie Johnson, Vincent Meunier, and Marija Drndić. Raman shifts in electron-irradiated monolayer MoS_2. *ACS Nano*, 10(4):4134–4142, 2016.

[14] Yang Leng. *Materials characterization: introduction to microscopic and spectroscopic methods*. John Wiley & Sons, 2009.

[15] Weilie Zhou and Zhong Lin Wang. *Scanning microscopy for nanotechnology: techniques and applications*. Springer Science & Business Media, 2007.

[16] Bob Hafner. Scanning Electron Microscopy Primer. *Characterization Facility, University of Minnesota-Twin Cities*, pages 1–29, 2007.

[17] D.P. Woodruff and T.A. Delchar. *Modern Techniques of Surface Science: Second Edition*. Oxford University Press, 1994.

[18] J.F. Watts and J. Wolstenholme. *An Introduction to Surface Analysis by XPS and AES*. John Wiley & Sons, 2003.

[19] John C Vickerman and Ian S Gilmore. *Surface Analysis: The Principal Techniques*. John Wiley & Sons, 2011.

[20] Lorenzo Calvo Barrio and Gardenia Vargas. Photoelectron spectroscopy for surface analysis: X-ray and UV excitation. *Capítol del llibre: Handbook of instrumental techniques for materials, chemical and biosciences research, Centres Científics i Tecnològics. Universitat de Barcelona, Barcelona, 2012. Part I. Materials technologies (MT), MT. 1, 12 p.*, 2012.

[21] MP Seah and WA Dench. Quantitative electron spectroscopy of surfaces: A standard data base for electron inelastic mean free paths in solids. *Surface and Interface Analysis*, 1(1):2–11, 1979.

[22] Cody V Cushman, Shiladitya Chatterjee, George H Major, Nicholas J Smith, Adam Roberts, and Matthew R Linford. Trends in advanced xps instrumentation. *Vacuum Technology and Coating Novermber*, 2016.

[23] Stephan Hufner. *Photoelectron Spectroscopy: Principles and Applications*. Springer Science & Business Media, 2003.

[24] Dave A Shirley. High-resolution X-ray photoemission spectrum of the valence bands of gold. *Physical Review B*, 5(12):4709, 1972.

Chapter 3

Experimental Instrumentation and Sample Preparation

This chapter provides a summary of the equipment and techniques used to gather data for this thesis. The sample preparation and experimental approaches used in this work are also outlined.

3.1 Custom Built Chemical Vapour Deposition Systems

The monolayer and few-layer films of graphene and MoS_2 studied in this thesis are produced by Chemical Vapour Deposition (CVD). The physics and chemistry of the CVD process is discussed in detail in Chapter 2. CVD was chosen over the other methods available for the growth of two-dimensional solids, briefly discussed in Chapter 1, as it has the advantage of producing consistent, high-quality films with controlled layer thickness. Two home-built 'hot-wall' CVD systems were constructed for the work presented in this thesis – one for graphene growth and one for MoS_2 growth. Both CVD systems utilise low-cost, readily available equipment and precursors. The systems were designed to operate at atmospheric pressure with an inert carrier gas in order to eliminate the requirement for expensive vacuum pumps, gauging and associated accessories.

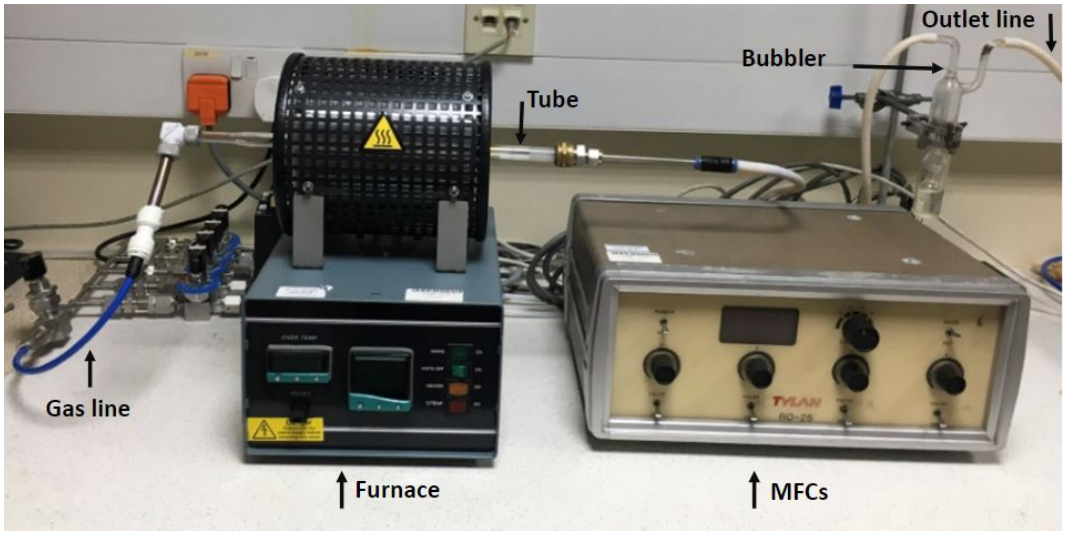

Figure 3.1: *The hot-wall CVD graphene growth system in the Department of Physics at Durham University is made up of several components, as labelled. It consists of a gas line connected to the furnace tube inlet to supply precursors to the reactor chamber, which leads to the formation of graphene. This is described in detail later in the text.*

Typically, a CVD system consists of several basic components: a gas delivery system for the supply of precursors to a heated reactor chamber and a means of exhausting the gas flow. The system used for CVD graphene growth is shown in Figure 3.1. Precursors and carrier gas were introduced into the growth region by a stainless steel gas handling line with VCR connectors. The gas line consists of a number of branches each connected to a separate gas supply, the flow through which can be regulated by Tylan FC-2600 mass flow controllers (MFCs), matched to the desired flow rate range of the gaseous precursors. The MFCs were controlled by a Tylan RO-28 controller, which is capable of regulating the

flow through four separate channels independently. For the purposes of graphene growth two branches of the gas handling line were used, one connected to a cylinder supplying 5% H_2 in Ar (with both gases of 99.99% purity) and the second pure CH_4 (99.995% purity). This arrangement enables a continuous flow of the reducing H_2/Ar gas while enabling the methane to be introduced only when the reactor chamber is within the desired temperature range. The reactor consists of a quartz tube of 1 cm internal diameter which is placed within a horizontal cylinder tube furnace (Vecstar VCTF1 with CAL9400 PID controller). Prior to use the temperature distribution within the furnace was measured and calibrated with respect to the nominal set-point temperature to ensure that the sample temperature is known exactly and that the sample is placed in a region where the temperature distribution is uniform as shown in Figure 3.2. Variables such as growth temperature, ramp rate, and cooling rate can be controlled by the furnace controller. The furnace temperature can be measured from room temperature to 1100°C with a variable ramp rate. The temperature profile used to prepare a typical graphene sample is shown in Figure 3.3.

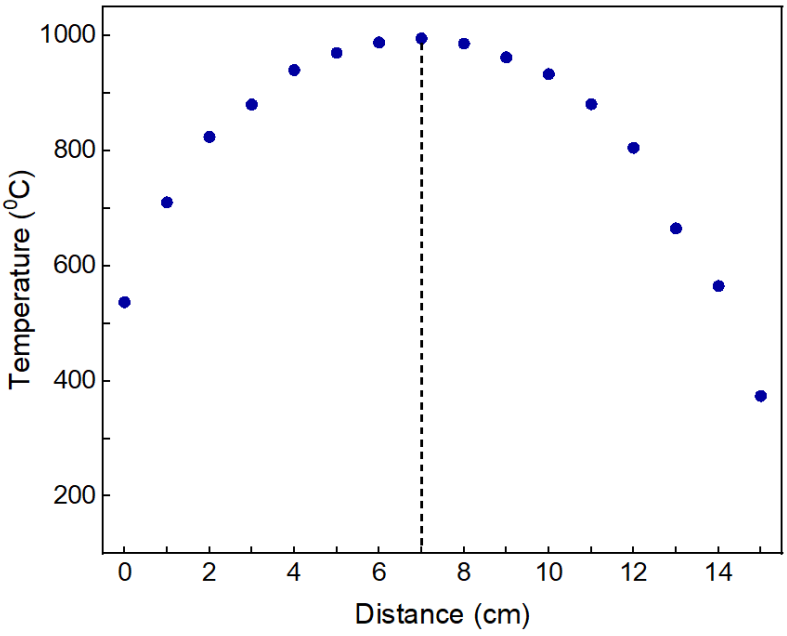

Figure 3.2: *Temperature distribution measured within the Vecstar VCTF1 furnace at a nominal setpoint of 1000 °C. The horizontal axis indicates the position of the thermocouple within the furnace and the dotted line the point at which maximum temperature was found to occur.*

MoS_2 samples were grown in a similar CVD system using a Carbolite furnace in which a single gas line regulated by a Vacuum General UltraFlow MFC controlled by a Tylan RO-32 controller was used to supply pure N_2 as a carrier gas, the system is shown in Figure 3.4. The precursors for MoS_2 growth consist of solid sulphur powder and MoO_3 powder which,

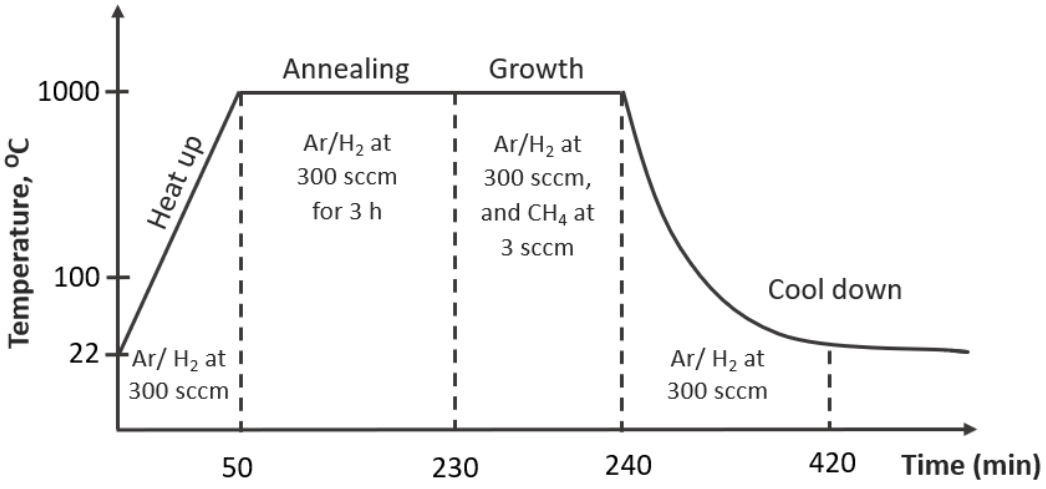

Figure 3.3: *Schematic of the temperature profile used for the CVD growth of graphene.*

due to their high boiling temperatures were vaporised within the quartz reaction tube. The sulphur was heated by two approaches, either by sliding a boat containing sulphur powder forward within the furnace when a chosen temperature was reached or by the use of a 'pre-heating' stage, consisting of a region of the quartz tube immediately outside the body of the furnace heated by a glass-fibre insulated heating tape and controlled by a PID temperature controller (CAL9200) linked to a thermocouple in direct contact with the quartz tube. The different approaches to the growth of MoS_2 growth are discussed in more detail below.

3.2 Sample Preparation

3.2.1 Monolayer and few-layer graphene on copper

One of the key parameters affecting the quality of graphene films is the condition of the substrate surface, which can be expected to influence nucleation density, defect concentration, and the growth of multilayers [1, 2, 3]. Polycrystalline copper foils (0.2 mm thick and 99.9% purity) were used in all graphene growth experiments. Three surface treatment procedures were used to investigate the effect of surface state on graphene growth, which are described below.

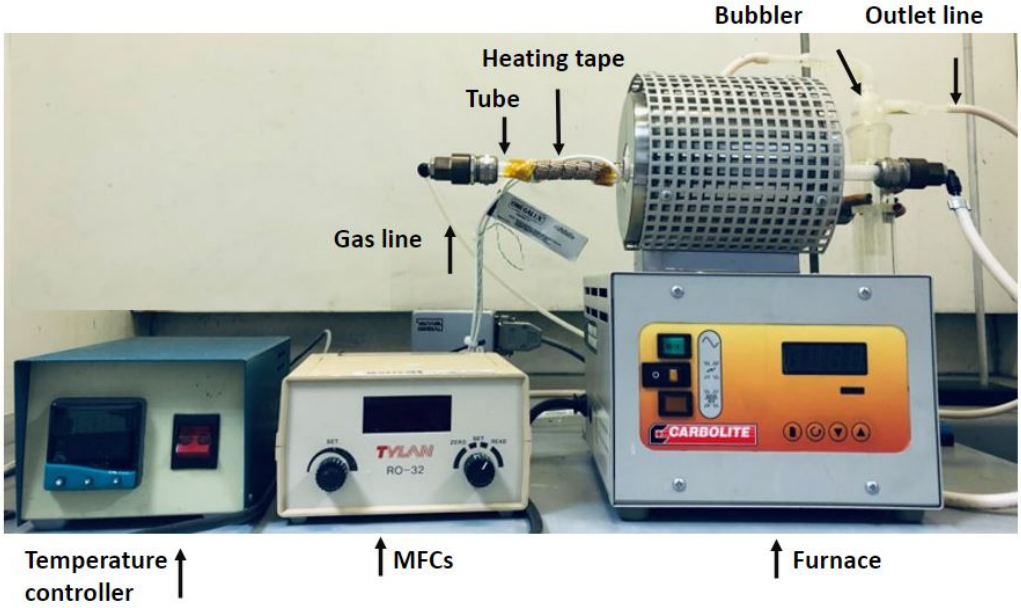

Figure 3.4: *The hot-wall CVD MoS_2 growth system in the Department of Physics at Durham University is made up of several components as labelled. The primary differences with that used for graphene growth are a simplified gas-line and the incorporation of a second heated zone outside the main body of the furnace.*

Etching with acetic acid

Polycrystalline Cu substrates were prepared and cleaned by sonication for ten minutes in acetone and then for the same amount of time in isopropanol. The substrates were then dipped in acetic acid for 15 s, washed in ultra high purity (UHP) water (15 MΩ cm) and dried under nitrogen. Etching using acetic acid was chosen rather than hydrochloric acid (HCl) because acetic acid directly targets copper oxide without significant etching of the copper surface [4]. The chemical equations for reaction between copper oxide and acetic acid are:

$$CuO + 2CH_3COOH \rightarrow Cu(CH_3COO)_2 + H_2O \tag{3.1}$$

$$Cu_2O + 4CH_3COOH \rightarrow 2Cu(CH_3COO)_2 + H_2O + H_2 \tag{3.2}$$

Etching using concentrated HCl would be faster and potentially more efficient. However, it is likely to lead to pitting of copper the surface because it not only removes the oxide layer but also removes large amounts of copper, whereas dilute HCl neither etches copper nor etches the oxide layer [5]. Rather dilute HCl will react with copper oxide and convert it to copper chloride as shown in Equation 3.3. The resulting chloride is difficult to remove it

by acetone, water or even with high temperature.

$$Cu_2O + 2HCl \rightarrow 2CuCl + H_2O \tag{3.3}$$

Electropolishing

Electropolishing, also known as electrochemical polishing or electrolytic polishing, is an electrochemical process that aims to reduce micro roughness, thereby reducing the risk of residues that adhere to the surface [6]. It can be used for brightening and passivating. In the electropolishing process, metal is removed from a sample by passing an electric current through an appropriately chosen solution. Electropolishing can be described as the reverse of electroplating, in which metal ions are deposited on to the sample from the solution; in an electropolishing system, the sample itself is dissolved and then adds metal ions to the solution.

Figure 3.5 illustrates a typical electropolishing cell. Both terminals of a DC power supply are immersed in the electrolyte, forming a complete electrical circuit. When current passes from the anode, which is usually the sample and is attached to the positive terminal, metal on the surface is oxidized and dissolved in the solution, which then passes to the cathode, attached to the negative terminal. The conditions of electropolishing, such as time and quantity of current, determine the amount of metal removed from the sample. Concentrated acid solutions, such as mixtures of sulphuric acid and phosphoric acid, which have a high viscosities, are typically the electrolytes used for electropolishing.

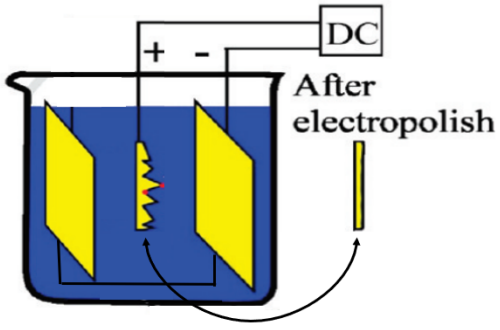

Figure 3.5: *Schematic illustration of a typical electropolishing cell. The cell has two electrodes (cathode and anode) that are both in an electrolyte and connected to each other electrically. As the current from the power source passes from the anode to the cathode, the metal on the surface is oxidized and dissolved in the solution, which then passes to the cathode. After the proper electropolishing process, the sample or anodic surface becomes clean and smooth. Adapted from [6, 7].*

Electropolishing (EP) of Cu foil samples was carried out with 85% H_3PO_4 [8, 9] with an applied bias of 5 V and a current of 3 A for 2 min [5]. Copper foils were used as both anode and cathode. The electrolyte solution was obtained by mixing 50 ml of ethanol, 50 ml of 85% phosphoric acid, 100 ml of deionized water, 10 ml of isopropanol, and 1 g of urea. After cleaning, the copper foils were rinsed in ultra-high purity (UHP) water (15.0 MΩ cm) to remove any residual solution. This step is very important as otherwise these impurities will act as nucleation sites during CVD growth and therefore affect the structure of the graphene film. The samples were then dipped in ethanol to remove the UHP water and dried under a pure N_2 gas flow.

Etching with Nitric Acid (NA)

A number of copper surfaces were also prepared by etching with dilute nitric acid (25%) for durations of 30, 45, 60 and 90 s followed by an immediate rinse in UHP water. This process was repeated three times for each sample, using fresh UHP water each time. After rinsing with water the copper foil sample was washed with acetone and isopropanol and then dried under a N_2 flow. Etching with nitric acid occurs following the scheme in Equation 3.4 [2].

$$4HNO_3(l) + Cu(s) \rightarrow Cu(NO_3)_2(aq) + 2NO_2(g) + 2H_2O(l) \tag{3.4}$$

During this reaction, the top of Cu surface is dissolved in the solution and NO_2 gas is generated, which in turn pushes any impurity particles away from the surface [2]. The resulting copper surface is clean but the surface is rough and an annealing step is employed to create a smooth surface. Figure 3.6 shows the copper pre-cleaning procedure with nitric acid etchant for each step.

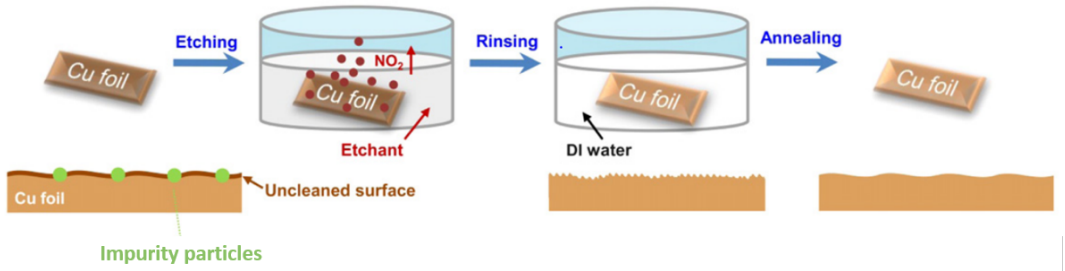

Figure 3.6: *A schematic depiction of the copper cleaning procedure with a nitric acid etchant. The copper surface is roughened during this process. The copper surface can subsequently be smoothed by thermal annealing [2].*

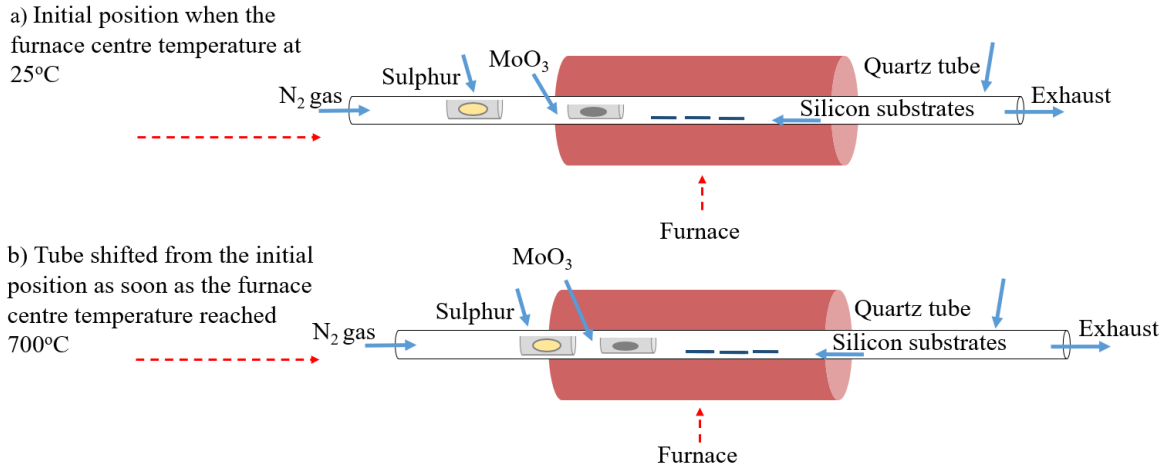

Figure 3.7: *Schematic of the chemical vapour deposition (CVD) of MoS_2 by Method #1.(a) Initial position when the furnace centre temperature is at 25°C. (b)Tube shifted from the initial position as soon as the furnace centre temperature reached 700°C. MoO_3 and S powders were used as solid precursors for MoS_2 growth. MoO_3 was placed inside a quartz boat close to the center of the furnace. S was placed in another quartz boat upwind in the quartz tube and pushed inside the furnace for MoS_2 growth. The silicon substrates was placed next to the powder, downwind for deposition.*

3.2.2 Growth of MoS_2

MoS_2 was grown on silicon(111) substrates with native oxide supplied by Compart Technology Ltd. cut into 7×5 mm^2 samples. Before introduction into the CVD system, silicon substrates and boats were cleaned by ultrasonication first in acetone and then in isopropanol (each for 10 min). To eliminate remaining solvents, the Si substrates and boats were rinsed with UHP water (15 MΩ cm) and dried with pure nitrogen gas before being introduced into the CVD system. Three different methods were used to optimise the growth of MoS_2 which are described in the following sections.

3.2.2.1 Initial approach (Method #1)

MoS_2 samples were produced following the general method of Balendhran and co-workers [10]. A schematic of MoS_2 outlining this approach to MoS_2 growth is shown in Figure 3.7. Silicon samples, prepared in the manner described above, were used as substrates and MoO_3 and sulphur powder were used as precursor sources. The temperatures of MoO_3 and sulphur powders were controlled by their position within the furnace. A quartz boat containing MoO_3 (0.05 g) was placed inside the quartz furnace tube and positioned 6 cm upstream of furnace centre. Sulphur powder (0.6 g) was placed in a second quartz boat and positioned upwind with respect to the gas flow direction, which was outside of the heating

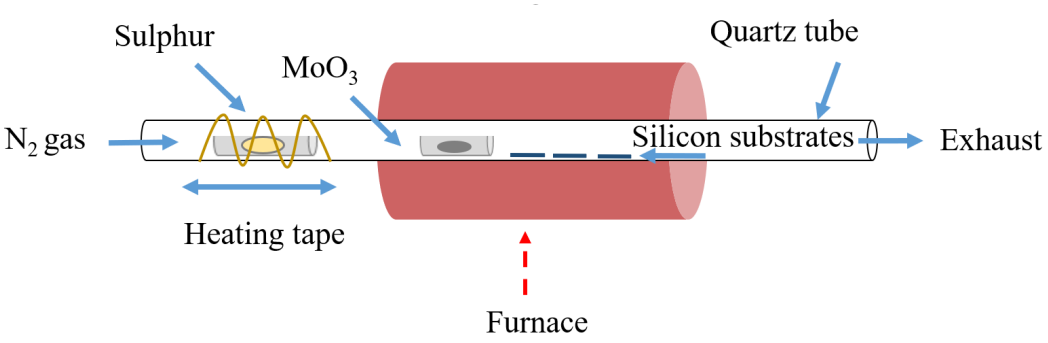

Figure 3.8: *Schematic of the chemical vapour deposition (CVD) system. Sulphur was placed in quartz boat upwind in the quartz tube and heated by external heating.*

center by 10 cm. In all growth approaches the sulphur powder was melted in the quartz boat before introduction into the furnace to produce a solid sulphur source to ensure a uniform and constant sulphur evaporation rate throughout the growth cycle. If the sulphur remained in powder form it was found that the initial rate of evaporation was high, due to the high surface area of the precursor. The rate of evaporation would then slow as the remaining sulphur melted into liquid form.

Silicon substrates were placed next to the MoO_3 for deposition Figure 3.7a. Before the reaction, the furnace tube was flushed with nitrogen N_2 at a rate of 250 sccm for 20 minutes, regulated with the mass-flow controller, this flow rate was then maintained throughout the growth cycle. The furnace tube containing the silicon substrates and the MoO_3 powder was then heated to the growth temperature, 700 °C, at a rate of 20 °C min^{-1}. When the furnace reached 700 °C, the quartz tube was pushed manually as seen in Figure 3.7b such that half the sulphur boat was moved into the furnace. Sulphur vapour was carried by the N_2 gas flow into the growth zone. The substrates were held at temperatures of 700 °C, 650 °C or 550 °C, depending upon their position in the furnace for 20 minutes while deposition occurred, while the MoO_3 was always held at 650 °C. The estimated temperature of the sulphur sources was 250-300 °C. After the growth period the furnace was switched off to cool the furnace to room temperature at a natural rate with the N_2 maintained to prevent sample oxidation. Once cool, samples were taken from the quartz tube and stored under ambient conditions until characterization was carried out.

3.2.2.2 Growth with external heating (Method #2)

The second method used for the growth of MoS_2 in this thesis employed additional external heating to the furnace localised to the region containing the sulphur precursor [11]. A schematic of the modified MoS_2 growth system is shown in Figure 3.8. In this case, the

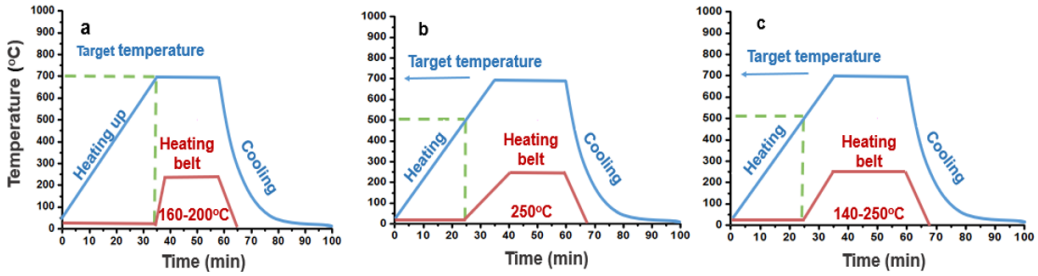

Figure 3.9: *Temperature profiles used in MoS_2 growth. The green dashed line shows the temperature of the furnace when the sulphur started being heated. The red line shows the time it took for sulphur to reach the desired temperature, which we had full control over. The blue line indicates the furnace temperature.*

temperatures of the MoO_3 and sulphur powders were separately controlled by the furnace temperature and the heating belt respectively. The furnace tube containing the silicon substrate and the MoO_3 powder was heated to the growth temperature, 700 °C, at a rate of 20 °C min^{-1} with the MoO_3 placed at a position within the furnace at a temperature of 650 °C. The sulphur was heated using heating tape to the selected target temperature after the furnace reached the growth temperature as depicted in Figure 3.9a and/or before the furnace reached the target temperature as shown in Figure 3.9b [12]. Sulphur vapour was carried by the N_2 gas flow into the growth zone. The substrate was held at a temperatures between 550 and 700 °C dependent upon its position within the furnace tube. Growth times of up to 2 h were used after which the furnace was allowed to cool naturally to room temperature under N_2 flow, as before.

In a final variation in which direct control was exercised over the sulphur temperature, the sulphur heating rate was chosen so that it reached its desired temperature at the same time as the furnace reached its target temperature see Figure 3.9c. The other parameters such as MoO_3 and N_2 gas flow remained the same.

3.2.3 Growth of MoS_2 on graphene and graphite

3.2.3.1 Method #1

Graphene/Cu substrates of about 10×7 mm^2 in area were grown in the graphene CVD system, fully characterised and then transferred to the second CVD system for MoS_2 growth. Initial attempts for MoS_2 growth on graphene/Cu followed Method #1 used for MoS_2 on Si, as described above. Graphene/Cu samples were placed face down on the MoO_3 boat for the deposition as illustrated in Figure 3.10a. When the furnace reached the target

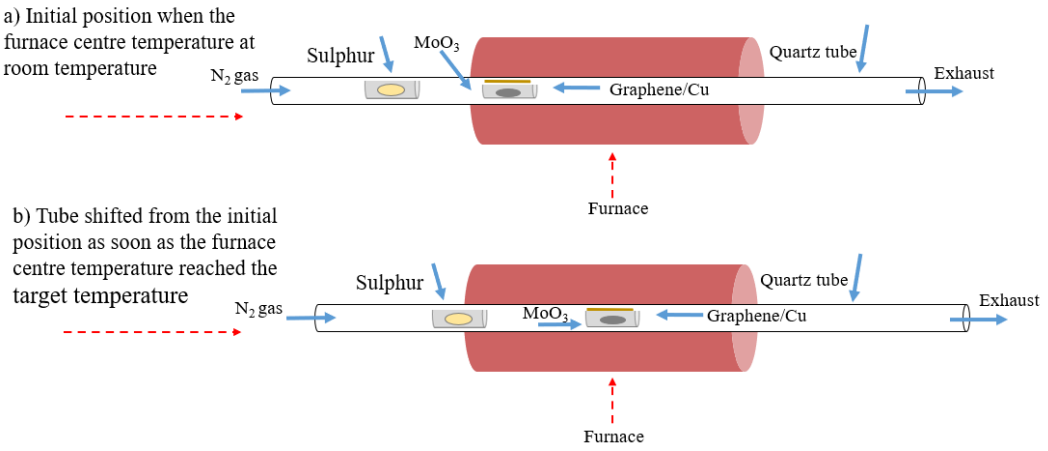

Figure 3.10: *Schematic of the chemical vapor deposition (CVD) growth of MoS_2 on graphene/Cu. (a) Initial position when the furnace centre temperature is at room temperature. (b) Tube shifted from the initial position as soon as the furnace centre temperature reached the target temperature. The graphene/Cu was face down on the MoO_3 powder.*

temperature, the quartz tube was pushed manually as shown in Figure 3.10b such that the graphene/Cu and MoO_3 moved to the centre, and half the sulphur boat was moved into the furnace. The substrate was held at temperatures of either 700 °C, 650 °C or 550 °C for 2 hours while deposition occurred.

3.2.3.2 Method #2

A second approach for MoS_2 growth on graphene/Cu was also trialled. This method involved keeping the position of the two precursors fixed such that the sulphur boat was kept next to the edge of the furnace rather than inside it as shown in Figure 3.11 to avoid the strong between the sulphur and the copper at high growth temperature

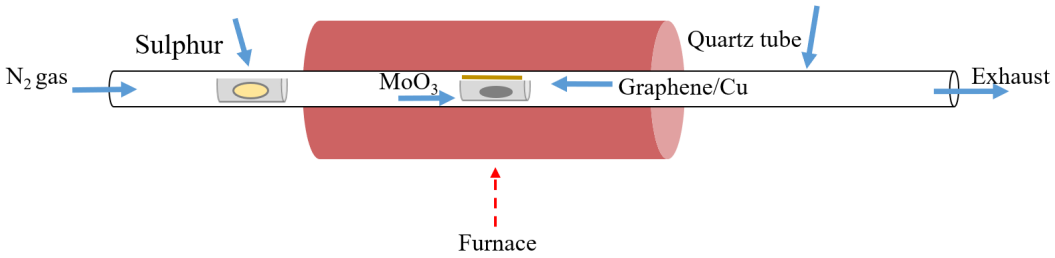

Figure 3.11: *Schematic of the chemical vapour deposition (CVD) system. Sulphur was placed in quartz boat upwind in the quartz tube next to the edge of the furnace. The final temperatures used for the sulphur were 140 °C and 200 °C.*

3.2.3.3 Growth of MoS_2 on graphite, graphene 'paper' and commercial graphene powder

In order to compare the growth of MoS_2 on bulk graphite with that on CVD-produced graphene and, ideally, to have an opportunity to optimise MoS_2 on graphene-like surfaces while using more readily available substrates that were simple to prepare, CVD with external heating (MoS_2/Si Method #2, 3.9a) was used to grow MoS_2 on highly oriented pyrolytic graphite (HOPG), graphene powder (Morsh) and a graphene 'paper' produced by the vacuum filtration of the Morsh material. The HOPG samples, ZYA grade supplied by SPI, were cleaved with Scotch Magic tape immediately prior to growth, which is an effective technique for producing a clean, contaminant-free surface and then inserted into the CVD growth system. Apart from the changes of substrate, other growth parameters were the same as those employed for MoS_2 growth on Si.

3.3 Raman spectrometer

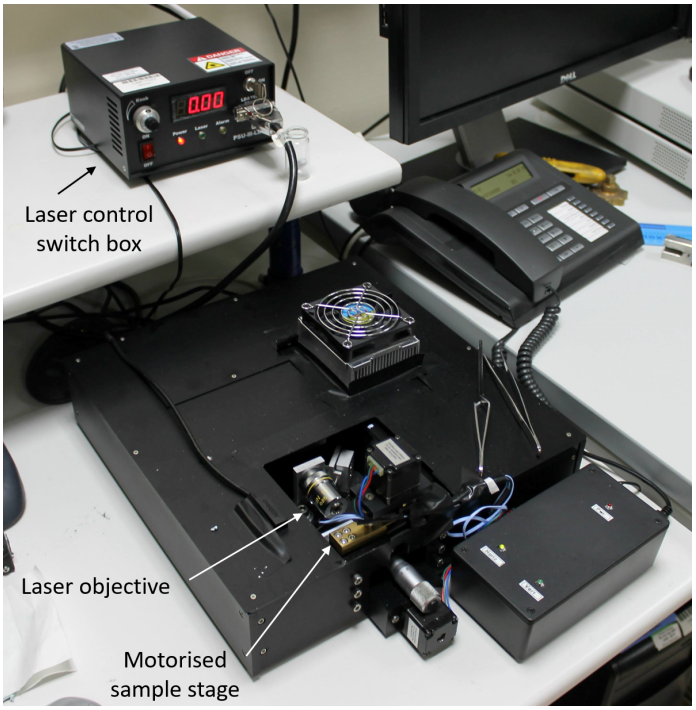

Figure 3.12: *The ASEQ RM-1 Raman Spectrometer in the Physics Department at Durham University [13].*

The Raman spectra of graphene, MoS_2 samples and precursor materials presented in this thesis were obtained in the Physics Department of Durham University using an ASEQ Instruments RM-1 spectrometer [14] modified with a stepper-motor driven sample stage

which enables the area under examination to be selected without opening the spectrometer casing, Figure 3.12. Light from a 532 nm wavelength laser is focussed onto the sample via a 10x objective lens which has a 10 mm working distance. The intensity of the laser light incident on the sample was generally kept below 4 mW in order to prevent thermally induced changes to the samples. The footprint of the laser light of $\approx 3 \times 10^{-4}$ cm^2 results in power densities similar to those typically employed in the literature [15]. Extended measurements demonstrated that no changes in spectra could be observed over any acquisition times used. Scattered light is collected by the same objective and passes through a Semrock long-pass filter, which eliminates all wavelengths below 537 nm, so removing Rayleigh scattered light which would otherwise dominate the spectrum. As a result of the use of a long-pass, rather than notch, filter only Stokes-scattered photons may be detected.

After passing through the long-pass filter the Stokes scattered light is incident on a HR1-T spectrometer with a thermoelectrically-cooled charge coupled device (CCD) detector and the signal acquired by a computer system. As the CCD system can be affected by drift, spectra were corrected appropriately. For samples of monolayer/few-layer graphene on copper and for precursor materials a spectrum from a SiC sample (which has several well-defined Raman peaks of known Raman shift) was obtained immediately prior to spectrum acquisition from the sample of interest. In the case of the MoS_2 samples grown on silicon the substrate signal was sufficiently strong to always be observed and the Γ_{25} symmetry Raman peak at 520.5 cm^{-1} [16, 17] was used an 'internal' wavenumber calibration.

3.4 FEI-Helios Nanolab 600 dual beam microscope

Scanning electron microscopy (SEM) characterisation of the graphene and MoS_2 samples presented in this thesis was performed using a FEI Helios Nanolab 600 dual beam microscopy system located in the G.J. Russell Microscopy Facility of Durham University, Figure 3.13. The instrument can operate in both ion beam and electron beam modes, but only the electron beam mode was used to image the samples in this work. The Helios Nanolab microscope can produce an incident electron beam with an energy between 50 eV and 30 keV with a current that can reach 22 nA. A lateral resolution of 0.9 nm can be acheived for images obtained at a beam energy of 15 keV [18]. An image of the FEI-Helios Nanolab's sample chamber that indicates major components is presented in Figure 3.14. Samples were directly mounted on microscope stubs using double-sided carbon tape, with no further sample preparation required. Images were typically acquired with primary electron energy of 3 keV and current of 0.17 nA.

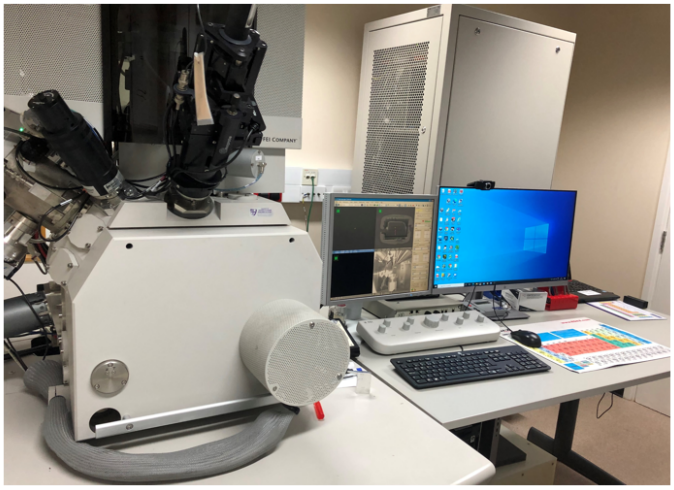

Figure 3.13: *The FEI-Helios Nanolab 600 dual-beam microscope in the G.J. Russell Microscopy Facility at Durham University.*

3.5 X-ray Photoelectron Spectrometer

X-ray photoelectron spectroscopy (XPS) measurements were undertaken at the NEXUS mid-range facility [19] in the faculty of Science, Agriculture and Engineering (SAgE) an Newcastle University. Spectra were acquired using a ThermoScientific K-Alpha X-ray photoelectron spectrometer, Figure 3.15, operating under ultra-high vacuum (UHV) conditions. The spectrometer consists of a monochromated Al K_α x-ray source, four-axis sample stage and a 180° double focusing hemispherical electron energy analyser with a 128-channel CCD detector [20].

X-ray photoelectron spectra were taken with a pass energy of 150 eV, step size of 0.4 eV and dwell time of 0.3 sec per point for survey spectra and 40 eV for high-resolution data with a step size of 0.05 eV and a dwell time of 1 s per point. All samples were sufficiently conductive to obviate the need for charge compensation and multiple spectra were taken from different regions of each sample.

A consistent energy reference is important in determining the precise binding energy of core-level photoelectron peaks, particularly as their position may be influenced by their local chemical environment, leading to a 'chemical shift', as discussed in Chapter 2. These subtle changes in binding energy provide extremely valuable insight in the chemical, as opposed to merely elemental, structure of the material under investigation. For the data presented here energies were referenced to the Si $2p_{3/2}$ core level, with binding energy taken as 99.50 eV, which is the modal value from twenty references in the U.S. National Institutes of Standards and Technology XPS database [21] (the average value of binding

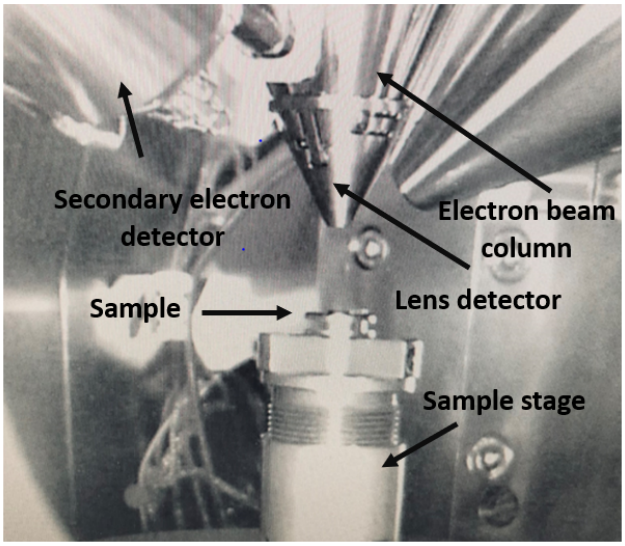

Figure 3.14: *Image of sample chamber in the FEI-Helios Nanolab system, several key components are labelled.*

energies, 99.53 eV agrees with the modal value to within the binding energy error in our measurements). The exact position of the Si 2p lines was obtained by fitting a doublet peak consisting of the convolution Gaussian-Lorenztian lineshapes combined with an inelastic electron background calculated by the method of Shirley [22].

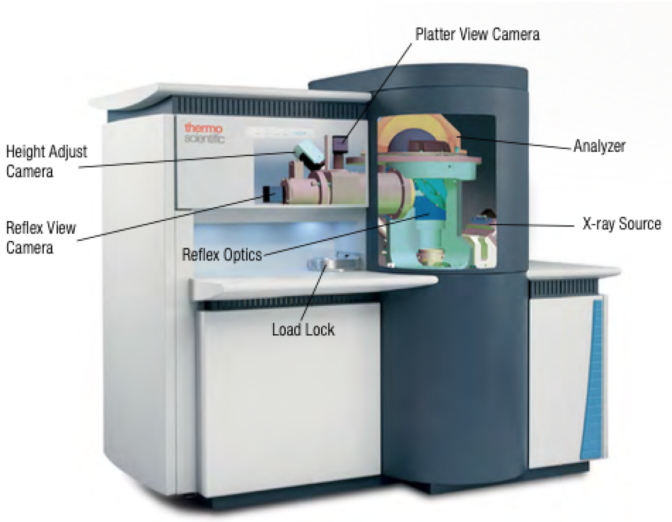

Figure 3.15: *ThermoScientific K-Alpha x-ray photoelectron spectrometer with key components labelled [20].*

References

[1] Gang Hee Han, Fethullah Gunes, Jung Jun Bae, Eun Sung Kim, Seung Jin Chae, Hyeon-Jin Shin, Jae-Young Choi, Didier Pribat, and Young Hee Lee. Influence of copper morphology in forming nucleation seeds for graphene growth. *Nano Letters*, 11(10):4144–4148, 2011.

[2] Soo Min Kim, Allen Hsu, Yi-Hsien Lee, Mildred Dresselhaus, Tomás Palacios, Ki Kang Kim, and Jing Kong. The effect of copper pre-cleaning on graphene synthesis. *Nanotechnology*, 24(36):365602, 2013.

[3] HoKwon Kim, Cecilia Mattevi, M Reyes Calvo, Jenny C Oberg, Luca Artiglia, Stefano Agnoli, Cyrus F Hirjibehedin, Manish Chhowalla, and Eduardo Saiz. Activation energy paths for graphene nucleation and growth on cu. *ACS nano*, 6(4):3614–3623, 2012.

[4] KL Chavez and DW Hess. A novel method of etching copper oxide using acetic acid. *Journal of The Electrochemical Society*, 148(11):G640, 2001.

[5] Alvin Lynghi Lee. *Towards reproducible graphene synthesis on optimized copper substrates*. PhD thesis, 2016.

[6] G Yang, B Wang, K Tawfiq, H Wei, S Zhou, and G Chen. Electropolishing of surfaces: theory and applications. *Surface Engineering*, 33(2):149–166, 2017.

[7] Zhengtang Luo, Ye Lu, Daniel W Singer, Matthew E Berck, Luke A Somers, Brett R Goldsmith, and AT Charlie Johnson. Effect of substrate roughness and feedstock concentration on growth of wafer-scale graphene at atmospheric pressure. *Chemistry of Materials*, 23(6):1441–1447, 2011.

[8] Sake Van Gils, Christophe Le Pen, Annick Hubin, Herman Terryn, and Erik Stijns. Electropolishing of copper in h3po4: Ex situ and in situ optical characterization. *Journal of The Electrochemical Society*, 154(3):C175, 2007.

[9] Shyamala Shivareddy, Sang Eun Bae, and Stanko R Brankovic. Cu surface morphology evolution during electropolishing. *Electrochemical and Solid-State Letters*, 11(1):D13, 2007.

[10] Sivacarendran Balendhran, Jian Zhen Ou, Madhu Bhaskaran, Sharath Sriram, Samuel Ippolito, Zoran Vasic, Eugene Kats, Suresh Bhargava, Serge Zhuiykov, and Kourosh Kalantar-Zadeh. Atomically thin layers of MoS_2 via a two step thermal evaporation–exfoliation method. *Nanoscale*, 4(2):461–466, 2012.

[11] Xinsheng Wang, Hongbin Feng, Yongmin Wu, and Liying Jiao. Controlled synthesis of highly crystalline MoS_2 flakes by chemical vapor deposition. *Journal of the American Chemical Society*, 135(14):5304–5307, 2013.

[12] Shanshan Wang, Youmin Rong, Ye Fan, Mercè Pacios, Harish Bhaskaran, Kuang He, and Jamie H Warner. Shape evolution of monolayer MoS_2 crystals grown by chemical vapor deposition. *Chemistry of Materials*, 26(22):6371–6379, 2014.

[13] Alina Talmantaite. Kinetics of cvd graphene growth on polycrystalline copper and the influence of surface texture. Master's thesis, Dept. of Physics, Durham University, 2018.

[14] http://www.aseq-instruments.com/rm1_spec_full.pdf, 20/06/2022.

[15] M.R.C. Hunt (private communication).

[16] Raphael Tsu and Jesus Gonzalez Hernandez. Temperature dependence of silicon raman lines. *Applied Physics Letters*, 41(11):1016–1018, 1982.

[17] Rajesh Kumar and Manushree Tanwar. Effect of some physical perturbations and their interplay on raman spectral line shapes in silicon: A brief review. *Journal of Raman Spectroscopy*, 52(12):2100–2118, 2021.

[18] Helios nanolab 600i technical report, https://www.microscop.ru/uploads/helios-nanolab-600i-ds-web.pdf, 2014.

[19] https://www.ncl.ac.uk/sage/researchfacilities/analytical-services/nexus/, 08/06/2022.

[20] https://assets.thermofisher.com/tfs-assets/msd/brochures/br52586-k-alpha-brochure.pdf, 11/05/2022.

[21] https://srdata.nist.gov/xps/main_search_menu.aspx, 07/02/2022.

[22] Dave A Shirley. High-resolution X-ray photoemission spectrum of the valence bands of gold. *Physical Review B*, 5(12):4709, 1972.

Chapter 4

Chemical vapour deposition growth of monolayer, few-layer and multi-layer graphene on copper substrates

This chapter discusses experiments performed to explore the growth of graphene films via hot-wall atmospheric-pressure chemical vapour deposition (AP-CVD). In particular, the effects of different substrate cleaning protocols, precursor flow rates and growth temperatures were examined. Graphene, few-layer graphene (FLG) and multilayer graphene (MLG) films produced by AP-CVD were studied with Raman spectroscopy (RS) and Scanning Electron Microscopy (SEM) to determine thickness, relative defect density and morphology.

4.1 Introduction

As discussed in Chapter 1, high-quality graphene can be obtained by a variety of different approaches. Chemical Vapour Deposition (CVD) on metal substrates (e.g. copper foils), the principles of which are discussed in Chapter 2, has proven to be a highly effective approach for production of graphene and FLG due to its relative simplicity, low cost and scalability. This method was pioneered by Li *et al.* in 2009, and it has become the most promising method for the development of large-scale production of graphene [1]. The growth of graphene and FLG by CVD depends on a variety of different growth parameters each of which needs to be understood in order to optimise growth. These include substrate morphology [2], growth temperature [3], growth time [3, 4] and carbon precursor gas [5, 6].

Graphene growth by CVD requires the thermal decomposition of carbonaceous gaseous species at elevated temperatures (typically around 1000 °C) on a heated catalytic substrate (such as a metal film or foil), as shown in Figure 4.1. The carbon atoms resulting from catalytic dissociation of the gas molecules will diffuse on/dissolve in the surface and, if the conditions chosen are appropriate, can nucleate to form a graphene lattice. However, such growth is affected by many factors, such as the carbon solubility limit in the metal, the metal surface state, and thermodynamic parameters including temperature and pressure [7]. Copper is widely utilized as a substrate for CVD growth of graphene as it is inexpensive. Moreover, as discussed below, in many cases the growth of graphene on copper is a self-limiting process owing to the low carbon solubility in copper, which can help produce a uniform single-layer graphene overlayer [8]. Metals with a significant carbon solubility, such as nickel tend to precipitate carbon upon cooling, which often leads to the formation of a graphene multilayer and makes the production of a single or few layer graphene film difficult [9, 10]. As described in Chapter 3, we use a polycrystalline copper surface as a catalyst and CH_4 as a carbon-containing precursor gas.

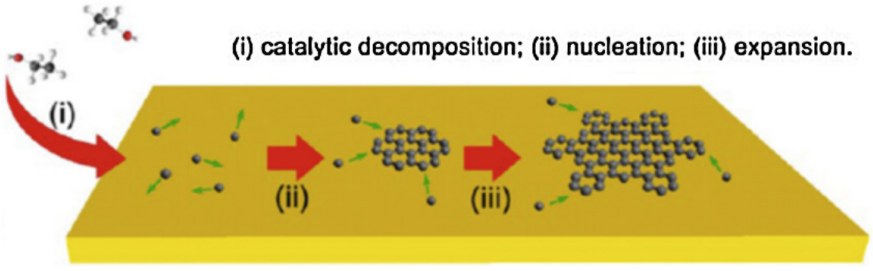

Figure 4.1: *Schematic of CVD graphene grown on Cu foil with low carbon solubility [11].*

The stages required for the growth of graphene and FLG on copper foils can be considered to be as follows: An initial cleaning or surface pre-treatment step is used to remove contamination and ensure that the copper foil becomes smooth and free from copper oxide. This, coupled with the presence of a reducing atmosphere in the growth system, enables the the carbon precursor to adsorb on the copper surface and catalytically decompose. The cleaning procedures used in this work are explained in detail in Chapter 3. The copper foil catalyzes decomposition of the methane precursor and the resulting carbon atoms migrate over the copper surface and diffuse until they find the nucleation sites. After nucleation, additional carbon species present on the surface are incorporated into the pre-existing graphene nuclei and form graphene islands. The graphene islands increase in dimension through growth and coalescence together at boundaries. Figure 4.1 shows the stages required for graphene growth. Under appropriate conditions, discussed later in this chapter, graphene growth on copper is self-limiting – when the copper surface is completely covered catalytic decomposition of the methane precursor can no longer occur and, as a result, no further graphene growth will take place [8].

As the gaseous precursors decompose, three surface conditions can be formed for the concentration of carbon species on the copper surface: undersaturated, saturated or supersaturated [12]. In the first condition, an insufficient supply of precursor and/or rate of precursor decomposition limits the concentration of carbon species on the surface, preventing the formation of stable graphene nuclei on the Cu surface. However, at saturation, enough carbon accumulates on the surface to cause stable nucleation and graphene growth. Island-like graphene structures are created in this situation. However, under these conditions the amount of carbon present is still insufficient to form a complete layer of graphene. Finally, when the surface becomes supersaturated, there is a high enough concentration of carbon species such that the graphene grows to fully cover the surface and produce a complete monolayer of graphene.

Hydrogen appears to play a significant role in CVD graphene growth. Vlassiouk and co-workers suggest that the presence of hydrogen during the growth step is a requirement for graphene CVD [13], while Yong *et al.* reported growth of graphene without adding any hydrogen to the methane source [14]. It is argued that the role of hydrogen on the surface during the growth process is that it contributes to the dehydrogenation of methane [13]. However, it is notable that when the hydrogen partial pressure is too high, the reactants will desorb, and the deposited layer will etch during graphene growth [4, 15].

4.2 Few-Layer and Multilayer graphene growth at high methane flow rates

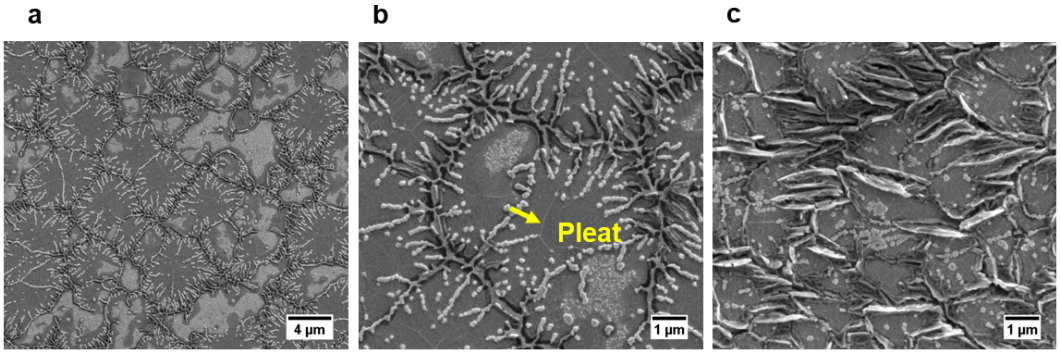

Figure 4.2: *SEM images of 'graphene' films grown on electropolished copper at growth times of 5 min (a,b) and 10 min (c) at a temperature of 1000* °C *and* CH_4 *flow rate of 3 sccm.*

Graphene samples were grown by AP-CVD on electropolished copper foil substrates at a fixed temperature (1000 °C) and methane flow rate (3 sccm) but with increasing growth times to understand the influence of this parameter on film thickness, morphology and quality. As discussed below, this choice of methane flow rate can be regarded as leading to a 'high' precursor concentration at the copper substrate. The SEM micrographs presented in Figure 4.2 show the morphology of a 'graphene' film grown at a temperature of 1000 °C, for growth times of 5 min Figure 4.2(a,b) and 10 min Figure 4.2(c). It can be seen that when the temperature is low and the concentration of methane is high, graphene growth is highly non-uniform, and there is clear evidence of multilayer graphene growth, demonstrated by the contrast variation over the sample. At the lower growth time shown, the coverage is clearly incomplete and light, granular features which can be identified as copper oxide can be observed after exposure of the samples to ambient atmosphere. The 'finger-like' structures of the copper oxide indicate that the graphene islands are dendritic, which implies limited diffusion of carbon precursor species over the surface under the growth conditions employed.

At longer growth times, Figure 4.2(c), clear evidence of film delamination is observed in the SEM micrographs. We refer to this film as 'multilayer graphene' (MLG) as Raman spectra, discussed below, indicate turbostratic layer stacking - i.e., stacking in which there is no well-defined relationship between the position and orientation of layers, unlike *AB* (Bernal) or *ABC* stacking. This terminology can be justified by reference to scanning tunnelling spectroscopy (STS) experiments performed on 'graphene on graphite', in which there is no well-defined stacking relationship between the outermost layer and the bulk [16]. In this study graphene-like behaviour was observed in the outermost layer due to the

inter-layer decoupling brought about by the disorder in the spatial relationship with the layer below.

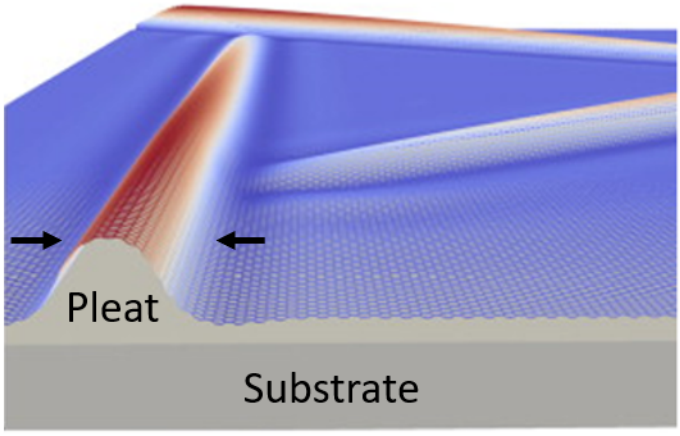

Figure 4.3: *Schematic diagram of a pleat defect in graphene on a substrate [17].*

It is most likely that the observed delamination of MLG at larger thickness originates from the differences in thermal expansion coefficient of graphene ($\alpha_{graphene} = -6 \times 10^{-6}$ K^{-1}) [18] and copper ($\alpha_{Cu} = 24 \times 10^{-6}$ K^{-1} [19]. At lower MLG coverage the greater reduction of the surface area of the copper substrate with respect to the FLG/MLG overlayer can be accommodated by the formation of a 'wrinkle' or 'pleat' within the overlayer, as can be seen by the thin line in the centre of Figure 4.2(b). Such pleats, shown schematically in Figure 4.3, have often been observed in monolayer and few-layer graphene films grown on a number of different substrates and are the most usual mode of strain-relief in these films. For example, pleat defects have been observed in single or few-layer graphene grown on copper [1, 2, 20], nickel [21, 22], platinum [23], and on SiC [24, 25, 26].

At longer growth times the thickness of the MLG films is such that it is no longer energetically favourable to form pleats as the strain energy in deforming multiple graphene layers will become too great. In this case the strain resulting from differential thermal expansion needs can be accommodated by a different mechanism and instead rupture occurs and the edges of MLG domains lift off the substrate surface. The pattern of rupturing observed in Figure 4.2(c) can be seen to follow the domain boundaries between MLG and is likely mediated by the edges of microcrystallites buckling as neighbours become too closely packed together. By such a mechanism strain can be relieved by minimal deformation of the MLG layers and the cost in adhesion energy of rupturing the bond between the substrate and the basal layer is smaller than that which would be incurred by forming a pleat defect in multiple graphene layers.

As discussed in Chapter 2, Raman spectra of graphene Figure 2.5 possess three main peaks, known as the D, G, and $2D$ (or $G^{'}$) bands at Raman shifts of approximately 1350 cm^{-1}, 1580 cm^{-1}, and 2717 cm^{-1}. The D peak can be associated with any defects or impurities which break symmetry and provides an indication of the relative perfection of graphene, FLG or MLG films provided they are measured under identical conditions (the dispersive, double resonant behaviour of the D band results in changes in relative intensity if measurement conditions, such as photon energy, are altered [27]. Typical Raman spectra from the sample presented in 4.2, are shown in Figure 4.4. Raw spectra, such as that shown in Figure 4.4(a) include considerable fluorescent background intensity, originating from the polycrystalline copper foil substrate which is fitted by a smooth polynomial background (shown in red) and subtracted in Figure 4.4(b) so that the shape and intensity of the MLG Raman lines can clearly be observed.

We find that when graphene is grown with a high methane flow rate, as here, a large D band intensity is present in the Raman spectra, in agreement with the results of Luo and co-workers [6]. However, the intensity of the D band with respect to the G band, I_D/I_G, which is commonly used as a metric for the relative defect density within graphene materials [1, 28], remains constant with growth time, to within experimental error, at 0.32 ± 0.01 indicating that the change in strain accommodation from pleat formation to delamination is not associated with, or due to, an increase in relative defect density within the MLG films as growth continues.

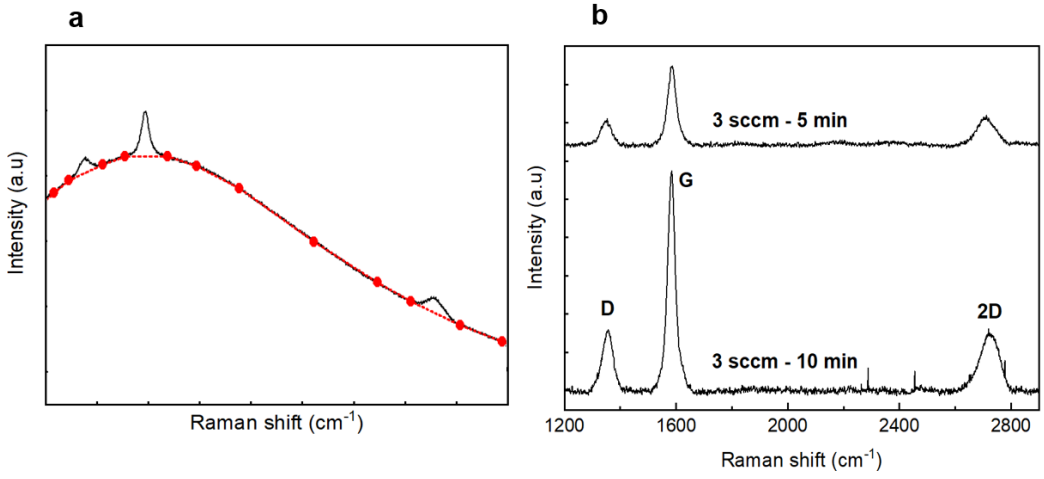

Figure 4.4: *(a) A typical Raman spectrum obtained from a FLG/MLG film grown at 1000 °C with 3 sccm methane flow rate. (b) Raman spectra for samples grown on electropolished copper at growth times of 5 min and 10 min at a temperature of 1000 °C and CH_4 flow rate of 3 sccm after removing the fluorescent background.*

It was initially thought, on the basis of results from micromechanically exfoliated graphene/FLG that the relative intensity of the G and $2D$ peaks, I_{2D}/I_G, could be used to determine the number of graphene layers within a sample. In particular the Raman spectrum of monolayer graphene spectrum was determined by a strong $2D$ intensity that is greater than the G peak, with the ratio I_{2D}/I_G greater than 2. However, subsequent studies demonstrate that even for micromechanically exfoliated graphene the intensity and position of the G and $2D$ peaks can be influenced by defects [29] and doping [30]. It was discovered that the intensity of the G and $2D$ peaks decreases as the defect density increases [29]. Moreover, it is possible to have different G peak positions and full-width at half maximum (FWHM) for different positions within the same graphene sample. This suggests that inhomogeneous self-doping is possible in graphene films.

It is therefore important to distinguish between monolayer, few-layer and multilayer graphenes not through examination of the I_{2D}/I_G ratio but through examination of the 2D peak shape [27]. The change in $2D$ peak content of samples prepared by micromechanicaly cleaving was explained by Ferrari [31]. For example, in the case of monolayer graphene, the $2D$ Raman peak is symmetric and composed of a single Lorentzian line, while for multilayer graphene with Bernal stacking, the peak is asymmetric and exhibits several overlapping Lorentzian peaks. Figure 4.5 shows the differences in this band shape between a single and a few layers of graphene.

However, in the case of CVD growth or epitaxial graphene, this change in the $2D$ peak while transitioning from MG to BLG is typically not observed. This has been explained by the formation of non-AB stacked bilayers in CVD grown graphene samples, resulting in the $2D$ peak retaining its single Lorentzian shape when it transitions from MG to BLG, despite a blueshift in peak position and an expansion of the peak width up to 90 cm^{-1} [10, 32, 33]. Kim *et al.* [34] demonstrated that the shape of the $2D$ peak is dependent strongly on the coupling between the two layers for non-AB stacked double layers and on the orientation angle between these layers. The Raman spectra in Figure 4.4 show a single, somewhat symmetric lineshape, with a FWHM of 80 cm^{-1}, consistent with disordered (often termed 'turbostratic') stacking of layers in our FLG/MLG samples. Hence, although the samples clearly consist of multiple layers it is not possible to determine their precise thickness by means of the tools of Raman spectroscopy and SEM available for the work presented here.

The growth of graphene on copper is in principle self-limiting, as discussed at the start of this Chapter: as the copper becomes covered by the graphene, it is no longer available to catalytically decompose the hydrocarbon precursor and create active carbon species for further growth [1]. The growth of more than a single graphene layer has, however, been observed in a number of studies [7, 35]. It has been suggested that second layer islands may in fact grow underneath the first layer due to diffusion of precursor gases through grain

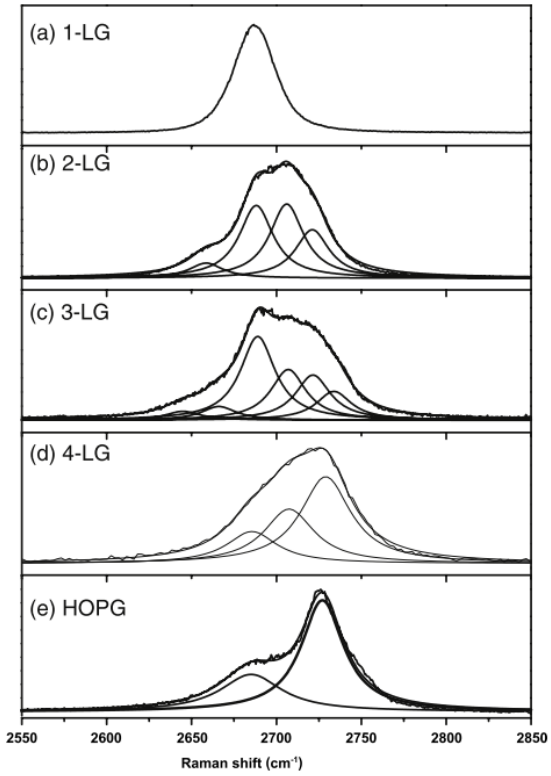

Figure 4.5: *The shape of the 2D Raman peak as a function of the number of graphene layers in a sample From [27].*

boundaries and similar defects (such as voids) where they may reach the copper surface and decompose [1, 36]. The relatively high defect density evidenced in Raman spectra under the growth conditions used to produce the samples in Figure 4.2 is therefore the likely origin of the enhancement of MLG formation over self-limiting monolayer graphene growth, due to the relative ease that the carbon feedstock can still reach the catalytically active surface even when the copper surface is fully covered with graphitic carbon. As a result, in the limit of longer growth times, we observe thicker films than in the literature and a mode of delamination which, to the best of our knowledge, has not been reported before.

4.3 Effect of growth temperate on graphene film formation

It has been demonstrated that growth temperature plays a vital role in determining the thickness of graphene/FLG films and the film coverage. Xing and co-workers [37] studied the effect of temperature and growth time on graphene films grown by ambient pressure CVD on copper foils, Figure 4.6. This study suggested that bilayer or few-layer graphene are formed at relatively low growth temperatures (900–1000 °C), while high temperatures (1050 °C) promote the growth of monolayer films. Graphene could not be grown when the substrate temperature was below 850 °C, even with a very long growth time. Other studies [12] have found that at high growth temperature, very low methane concentration and low partial pressure, the nucleation density of graphene is low with larger domain size.

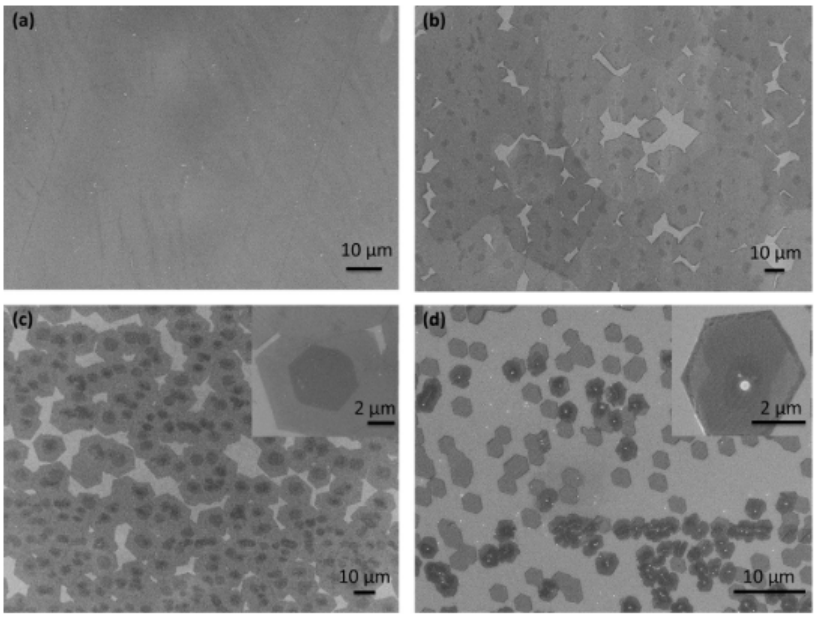

Figure 4.6: *SEM images of graphene films and grains grown on a Cu surface at various temperatures and times:(a) film grown for 30 minutes at 1050* °C*; (b) grains grown for 20 minutes at 1000* °C*; (c) grains grown for 60 minutes at 950* °C*; and (d) grains grown for 60 minutes at 900* °C *[37].*

The samples presented in this Chapter so far have been grown at substrate temperatures of 1000 °C and a 'high' methane flow rate (3 sccm), and we now explore the results as growth temperature is increased from 1000 °C to 1065 °C and above using a lower methane flow rate of 1 sccm. In this series of experiments the surfaces were pre-treated with acetic acid, as described in Chapter 3. SEM micrographs of typical samples grown with a methane flow rate of 1 sccm and a growth time of 4 min for temperatures of 1065, 1070 and 1075 °C

are shown in Figure 4.7. Figure 4.8 shows how the areal coverage of graphene varies between samples grown at these temperatures.

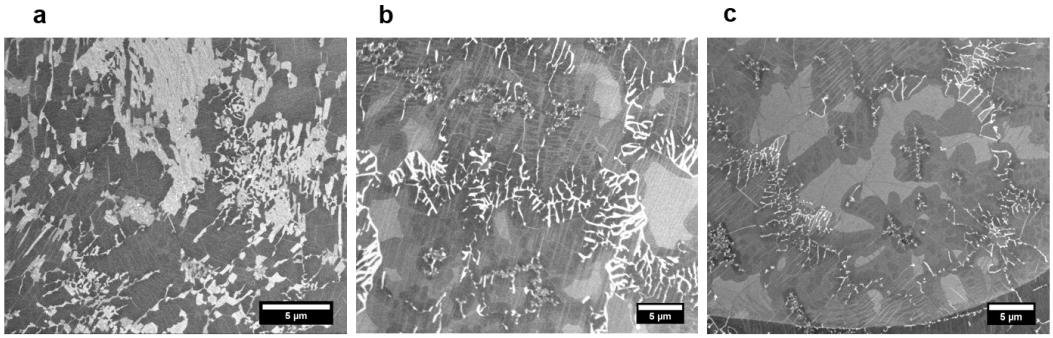

Figure 4.7: *Graphene were grown on acetic acid etched copper foils at a growth time of 4 minutes using different growth temperature (1065 °C, 1070 °C, and 1075 °C) a,b,c respectively.*

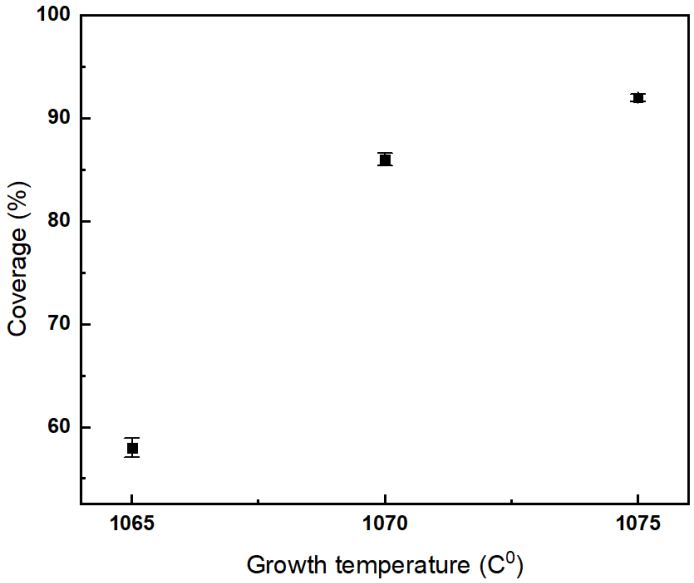

Figure 4.8: *Graphene coverage on Cu etched with acetic acid as a function of growth temperature with a CH_4 flow rate of 1 sccm and a growth time 4 min.*

Graphene films produced on acetic acid-treated foils at 1075 °C, shown in Figure 4.7(c), can be seen to be substantially different from those grown at 1065 °C Figure 4.7(a). There are several reasons by which substrate growth temperature can influence film morphology. For example, for growth close to the melting point of the copper the morphology of the foil surface is likely to change [38]. For example surface reconstruction could occur to smooth the

surface, leading to fewer dislocations and surface defects. Evidence of such behaviour was observed by Talmantaite and Hunt [39] who observed, using Electron Backscatter Diffraction (EBSD) that differences between copper grains presenting various surface planes dramatically reduced as surface temperature increased to just below the melting point of copper. With increasing growth temperature the areal graphene coverage can be observed to increase from 58% to 93% as shown in Figure 4.8. The coverage at a given growth temperature will be determined by a delicate balance between rates of adsorption and desorption of precursors and their rate of reaction at the metal surface. With increasing substrate temperature it can be expected that residence time of precursors at the metal surface would decrease and the rate of dehydrogenation increase. Thus, is can be concluded from the variation in coverage shown in Figure 4.8 that the latter dominates as substrate temperature increases.

4.4 Influence of surface pre-treatment on graphene growth

The condition of the catalytic surface, hence substrate treatment prior to growth, plays a key role in defining the morphology and defect density, the latter playing an role in film thickness as described above. In order to explore this aspect of graphene film growth substrates prepared by three different approaches – etching with acetic acid (AA), electropolishing (EP) and nitric acid (NA) – were prepared as previously detailed in Chapter 3.

As shown in the SEM micrographs of Figure 4.9, prior to cleaning the polycrystalline copper foil is rough and has significant striations and evidence of extrinsic impurities. After electropolishing, the foils are considerably smoother and contrast can be seen to emerge due to differing grain orientations within the foil. Annealing further improves the smoothness and uniformity of the foil, although a few (impurity) particles can be seen to remain on the surface. In contrast, etching the copper foil with nitric acid leads to a significant increase in surface roughness. However, this is ameliorated by annealing and the density of foreign particles remaining on the surface is substantially lower than that for an electropolished, annealed sample.

Figure 4.10 (a,b, and c) shows graphene islands for growth under 1 sccm of CH_4 flow for 2 min at a substrate temperature of 1065°C. Histograms showing the distribution of island areas, derived from a large number of SEM images taken at multiple positions over the samples are shown in Figure 4.10(d,e, and f). Graphene islands grown on electropolished and nitric acid Cu substrates have areas that can reach several hundred μm^2 and thousands of μm^2 whereas those grown on acetic acid-etched surfaces typically have areas that are less than 100 μm^2. The average island size is 40, 250, and 2000 μm^2 on etching with acetic

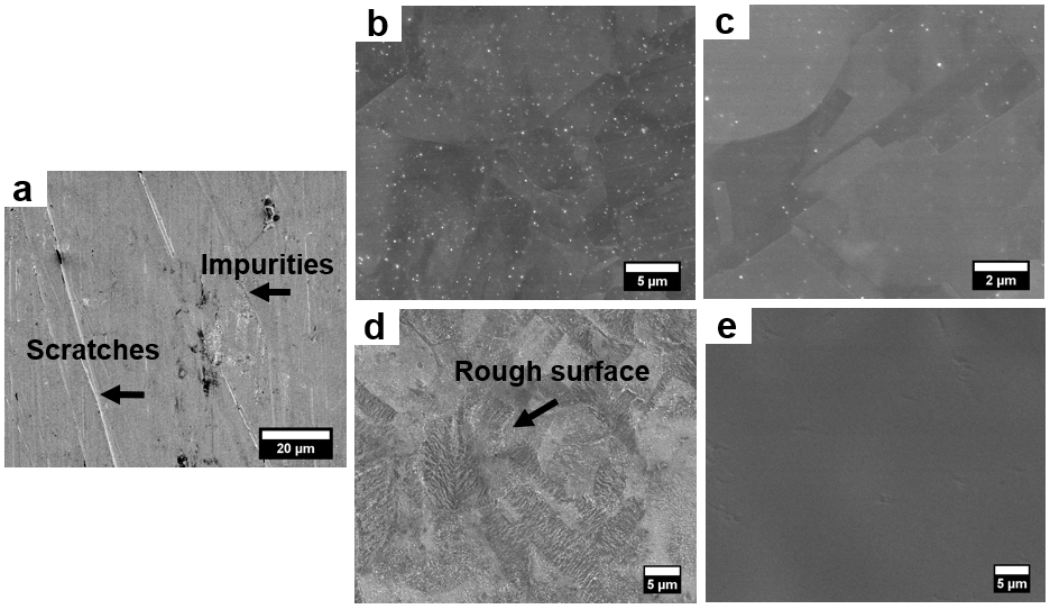

Figure 4.9: *SEM micrographs of (a) as-received copper foils prior to surface treatment showing striations due to rolling; (b) electropolished Cu before and (c) after annealing, (d) NA etched foil before and (e) after annealing.*

acid, electropolishing and etching with nitric acid respectively. The islands formed on the electropolished and nitric acid etched samples clearly have a much larger size than those which grow on the AA treated surface. The nucleation density at submonolayer coverages for samples produced by the three different surface treatment approaches is 0.008 ± 0.001 μm^{-2}, 0.0001 ± 0.0001 μm^{-2}, and 0.0005 ± 0.0001 μm^{-2} for acetic acid, electropolishing, and nitric acid treatments, respectively.

Increased island size and decreased nucleation density can be related to the increased mobility of carbon-containing pre-cursors over the graphene surface during the growth process and a lower concentration of defects which can act as 'trapping' sites for the adsorbed carbon species and so initiate island nucleation. A close examination of the island shapes in Figure 4.10 (a,b, and c) indicates a compact, close to hexagonal, morphology for all three surface treatments, consistent with a high degree of structural perfection within the islands themselves (and is noticeably different from the dendritic morphologies observed at lower growth temperatures). Thus, these results suggest that the primary cause of the differences in graphene island growth arises not from differences in mobility/diffusion but in the differing concentration of impurities and defects capable of acting as nucleation sites on the treated copper foils.

Typical Raman spectra of the submonolayer graphene films grown by CVD on substrates treated with acetic acid (AA), electropolishing (EP) and nitric acid (NA) are shown in Figures 4.10 (g, h, and i). In both cases the relative intensity of the D bands is rather small and, averaged over spectra from several different regions of each sample, the I_D/I_G ratios of 0.17 ± 0.05, 0.09 ± 0.03 and 0.18 ± 0.04 just agree to within experimental uncertainty with the suggestion that, with further measurements to reduce the statistical uncertainty in the data, the graphene islands may have a lower defect density on the electropolished surface.

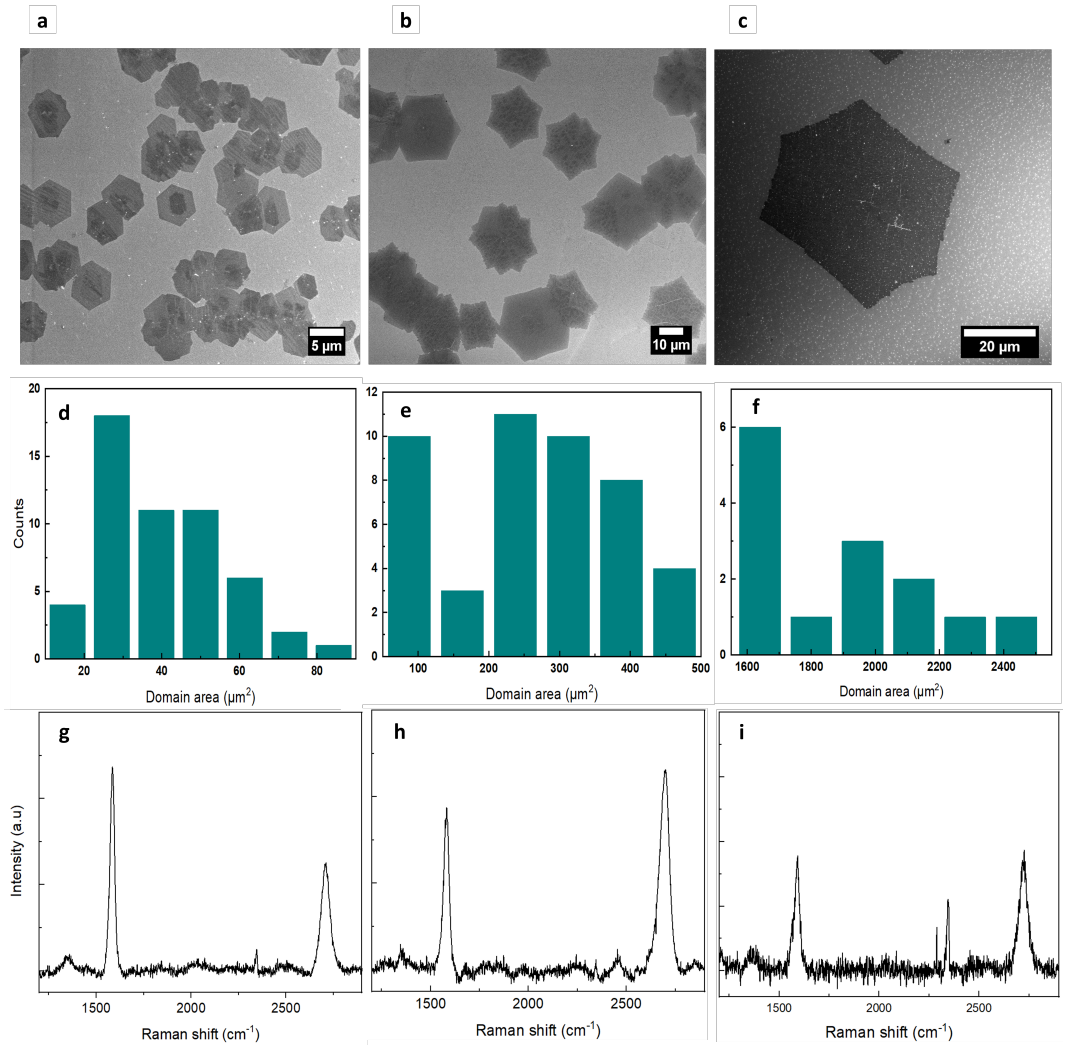

Figure 4.10: *SEM micrographs of graphene islands grown on (a) acetic acid etched; (b) electropolished; and (c) and nitric acid etched copper substrates. The growth temperature was 1065 °C, CH_4 flow rate 1 sccm and growth time 2 min for each sample. Corresponding island size distributions are shown in (d,e,f) and Raman spectra in (g,h,i).*

To further examine the effect of the three different cleaning procedures on the properties of the graphene/FLG films revealed by their Raman spectra, typical G band and $2D$ band regions of Raman spectra obtained from films grown under the same conditions are presented in Figure 4.11. It is notable that the G bands of samples grown on electropolished and nitric acid etched samples are blueshifted by 3.7 cm^{-1} and 5 cm^{-1}, respectively, with respect to graphene grown on an acetic acid etched substrate, for which the G band position is found to be 1581.7 ± 0.1 cm^{-1}. An upward shift in the $2D$ peak is also observed. The position of the $2D$ peak on a sample grown on the surface by acetic acid pre-treatment is 2711.1 ± 0.1 cm^{-1}, whereas that measured on the graphene films grown on electropolished and nitric acid samples is shifted up by 5 cm^{-1} and 8 cm^{-1}, respectively. Table 4.1 shows the position of the G and $2D$ peaks for graphene films grown on substrates with different pre-treatment procedures. In all cases the $2D$ band consisted of a broad line which could be fit with a single peak, Figure 4.12. The full-width at half maximum (FWHM) of the $2D$ line for electropolished and nitric acid treated samples are found to be the same, to within error, at between 60 and 70 cm^{-1}, but drops to 47 cm^{-1} for samples produced on acetic acid etch substrates. Raman spectra obtained from different regions of the same sample for each cleaning method showed a small variation in the G peak position which was much smaller than the difference with different cleaning methods.

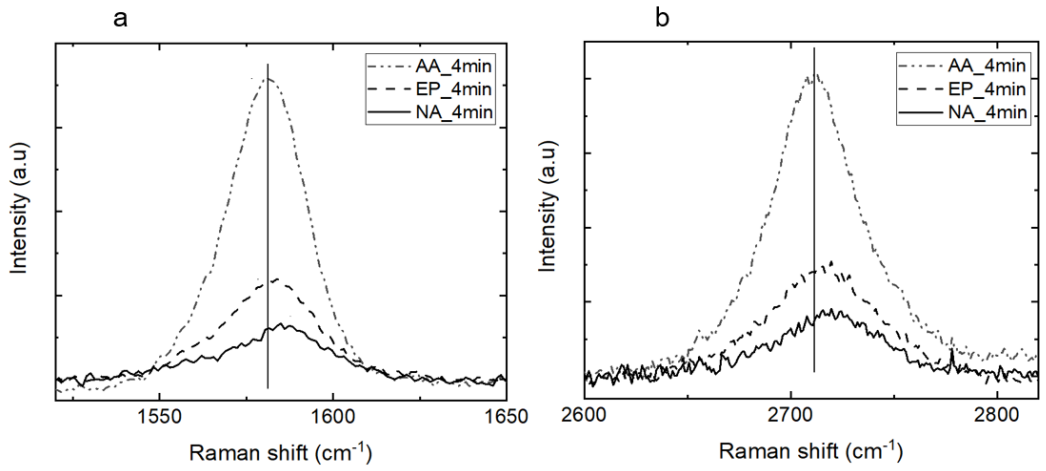

Figure 4.11: *Raman shifts of the: (a) G peak and the (b) 2D peaks for graphene produced with a growth time of 4 min at 1065* °C *and a* CH_4 *at flow rate of 1 sccm for different surface pre-treatments. The G and 2D peaks of graphene grown on the acetic acid treated surface are at* 1581.7 ± 0.1 cm^{-1} *and* 2711.1 ± 0.1 cm^{-1}*, but the G and 2D peaks of the graphene on electropolished and nitric acid are blue shifted, see Table 4.1.*

Figure 4.13 plots the position of the $2D$ Raman lines as a function of the position of the G line for graphene films grown with different the sample pre-treatments, acetic acid

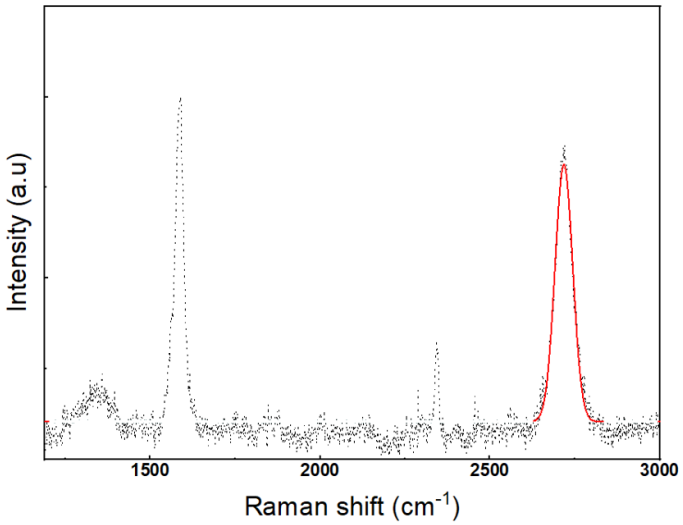

Figure 4.12: *Raman spectrum of as grown graphene on electropolishing Cu for 4 min at 1065 °C, with a single Pseudovoigt peak fit to the 2D peak shown in red.*

Sample	G **peak position** cm^{-1}	**2**D **peak position** cm^{-1}
Acetic acid treated Cu	1581.7 ± 0.1	2711.1 ± 0.1
Electropolishing Cu	1584.9 ± 0.1	2715.3 ± 0.3
Nitric acid treated Cu	1586.6 ± 0.3	2718.4 ± 0.6

Table 4.1: *The position of the G and 2D peaks position for graphene grown on substrates with different surface treatment.*

(AA) etching, electropolishing (EP) and nitric acid (NA) etching. Although there is some scatter within the data, it can be seen that the $2D$ position is directly proportional to that of the G peak, in agreement with Casiraghi [30]. Hence, there is a monotonic relationship between the two. Casiraghi [30] has demonstrated that variations in the Raman shifts of the $2D$ and G bands occur with respect to position even within micromechanically exfoliated samples, which can be attributed to local changes in doping within the graphene. Such shifts in Raman line positions may be attributed to doping from the substrate as suggested by Casiraghi or as a result of adsorbed oxygen or water [40, 41]. Similar changes in Raman line positions have also been deliberately induced by altering the charge carrier (both electron and hole) concentration within graphene embedded in a field effect transistor (FET) structure [42]. The points plotted in Figure 4.13 fall into three distinct regions depending upon the sample surface pre-treatment, indicating that the condition of the surface plays a distinct and reproducible role in the carrier concentration within the graphene film. This variation can be therefore be attributed to the degree of coupling, and

hence charge transfer/doping, between the graphene overlayer and the substrate.

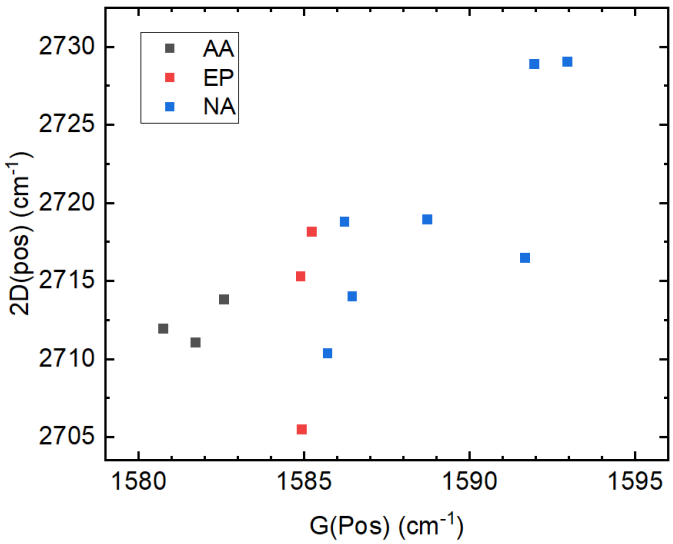

Figure 4.13: *2D position as a function of G position for graphene grown for 4 min at 1065 °C for different substrate treatments: acetic acid (AA) etching (black squares), electropolishing (EP) (red squares) and nitric acid (NA) etching (blue squares).*

Das and Pisana [42] observed that the G peak position blue shifts for both hole and electron doping, while the $2D$ position blue shifts with hole doping and red shifts with electron doping. The differing behaviour of the two Raman modes can be understood by considering the relative impact of two specific effects which originate from a change in the position of the graphene Fermi level (E_F) away from the Dirac point upon doping: (1) a change in the equilibrium lattice parameter with a consequent stiffening of phonon modes for a decrease in E_F (p type doping) and a softening of phonon modes for an increase in E_F (n type doping) due to charge occupation of π^* anti-bonding states; (2) a reduction in the degree of electron-phonon coupling as E_F moves away from the Dirac point.

The G peak is associated with a phonon of wave-vector $q = 0$ which strongly couples to electronic degrees of freedom when E_F is located at the Dirac point. The strong coupling leads to a breakdown of the adiabatic Born-Oppenheimer approximation and hence to a Kohn anomaly which depresses the phonon frequency. Doping either n or p type moves the Fermi energy away from the Dirac point, reducing the degree of electron-phonon interaction and the consequent suppression of frequency. Since this effect dominates over that due to bond stiffening/softening for the G peak phonons, their frequency is observed to increase for both electron and hole doping [42].

The double-resonant $2D$ peak, on the other hand, couples weakly to electrons and the Fermi level as the momenta of the associated phonons are far away from that associated with the Kohn anomaly. Therefore, the behaviour of the $2D$ peak is dominated by bond stiffening/softening leading to the observed blue shift upon hole doping and red shift upon electron doping.

Hence, based on the results shown in Figure 4.13, we can deduce that there is hole doping for graphene grown on copper substrates produced with all three cleaning methods. Moreover, the variation of line positions with different etching protocols can be associated with an increase in graphene doping level (and hence coupling) with surface pre-treatments in the order AA $\rightarrow$ EP $\rightarrow$ NA.

The hole doping of graphene, observed on substrates subject to all three cleaning treatments is consistent with the density functional theory (DFT) calculations of Giovanetti and co-workers [43] who studied the adsorption of graphene on a variety of metal surfaces. In particular, they find for weak adsorption dominated by charge transfer rather than bond formation, such as found on Al, Ag, Cu, Au and Pt, a simple analytic model can be derived for the Fermi level shift,

$$\Delta E_{\mathrm{F}}(d) = \pm \frac{\sqrt{1 + 2\alpha D_0 (d - d_0)|\phi_M - \phi_G - \Delta_c|} - 1}{\alpha D_0 (d - d_0)} \tag{4.1}$$

where ΔE_{F} is the Fermi energy shift observed for graphene adsorption on a metal surface of workfunction ϕ_M at a spacing d between the metal surface and the graphene. D_0 is the linear density of states of graphene (an approximation valid for small ΔE_{F}), d_0 is a constant reflecting the reduction in separation between positive and negatively charged planes from d due to the charge lying predominantly in the region between the metal and graphene, Δ_c is the potential step arising from the formation of an electric double layer upon charge transfer, ϕ_G is the graphene work function and $\alpha = e^2/\epsilon_0 A$ where A is the area of the graphene unit cell. Since d, d_0 and Δ_c are found to be very weakly dependent on the substrate, their values can be found by considering DFT calculations for a single model substrate. Therefore, only the work functions of the substrate (ϕ_M) and graphene (ϕ_G) are required in order to calculate the Fermi level shift of the latter and hence whether the graphene is electron or hole doped.

Assuming a graphene work function of 4.5 eV, which is consistent with values of 4.5 - 4.6 eV determined experimentally [44, 45, 46], the transition from hole to electron doping will happen for substrate work functions greater than $\phi_M \approx 5.4$ eV. Copper surfaces have work functions which vary with the surface face and have been found to lie between 4.48 eV for the (100) plane and 4.94 eV for the close-packed (111) plane by Gartland and co-workers [47], with similar values found by Renault *et al.* [48]. Polycrystalline copper surfaces

have been found to have work functions of between 4.40 eV [49, 50] and 4.55 eV [48]. The model of Giovanetti *et al.* [43] therefore predicts hole doping for graphene adsorbed on copper, in agreement with the interpretation of the Raman data presented in Figure 4.13.

The differences in degree of hole doping with surface treatment can be understood with reference to the increase in work function found with surface oxidation [50] since the texture of the copper foil (the relative contribution of crystal faces to the overall surface) will not be altered by room temperature chemical treatment. Instead, it is likely that the three surfaces treatments differ in their effectiveness in the removal of surface oxidation and other adventitious contaminants, leading to a variation in the average substrate work function. Equation 4.1 indicates that the Fermi level shift in graphene will depend upon $|(\phi_M - (\phi_G + \Delta_c))|^{1/2}$. On this basis, the largest hole doping is likely to occur on the surface with the lowest work function, which corresponds to that with the least contamination. Hence, it can be inferred that the effectiveness of surface treatments increases in the order AA $\rightarrow$ EP $\rightarrow$ NA, in agreement with the conclusions drawn from the increase in submonolayer island size and decrease in nucleation density observed in SEM.

The variation in FWHM of the $2D$ lines between the graphene growth on substrates with differing surface treatments, described above, cannot be easily explained in terms of the presence of bilayer and few-layer material coupled with the presence of turbostratic interlayer stacking – the SEM micrographs in Figure 4.10 do not show a large enough contribution from graphene islands of thickness two layers and above to be consistent with the Raman data. However, it is notable that the doping behaviour evidenced by the blue shift of the G and $2D$ lines with surface treatment correlates strongly with the $2D$ FWHM, with samples showing a greater degree of doping also presenting a larger $2D$ FWHM.

Das and Pisana [42] also noted that doping reduced the I_{2D}/I_G for both hole and electron doping. In Figure 4.13, I_{2D}/I_G ratio for graphene grown on AA, EP, and NA treated surfaces averaged over multiple spectra taken at different points is 1.2 ± 0.1, 1.4 ± 0.1, and 1.1 ± 0.2, respectively. The relatively large variation in I_{2D}/I_G ratio, leading to a substantial standard error in the mean value of this quantity means that it is not possible to effectively correlate the ratio of these two peaks with the doping levels evidenced by their respective positions.

Given the increase in graphene island size for submonolayer coverage, reduction in nucleation density and increase in coupling between the graphene islands with substrate surface treatments in the order AA $\rightarrow$ EP $\rightarrow$ NA, and it can be concluded that nitric acid etching of the copper foil substrate (followed by annealing) produces the optimum surface for graphene growth.

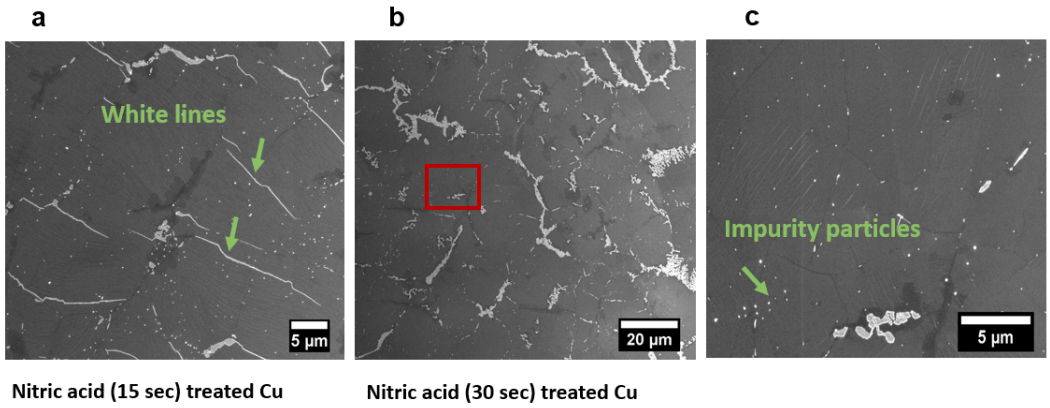

Figure 4.14: *Graphene grown on nitric acid treated surfaces with treatments times of (a) 15 sec and (b,c) 30 sec. Graphene layers were grown at a substrate temperature of 1065* °C *with a 1 sscm CH_4 flow rate for growth time 4 min. The presence of lines of contrast indicate incomplete graphene growth and impurity particles are clearly observed.*

To study the effect of NA etching time on graphene growth, samples were prepared by dipping copper foils in dilute nitric acid (25%) for varying etch times (15, 30, 45, 60 and 90 sec). Graphene was then grown on the samples at 1065 °C, for 4 min using a 1 sccm CH_4 flow rate. After growth all the surfaces are found to be completely covered with a graphene film, as can be seen in the images presented in Figure 4.14. A number of particles can be seen within the images which were found by Kim *et al.* to consist of mostly Si, Pt and Ru [51]. It is possible that these contaminants originate from the bulk of the copper foil and segregate to the surface at the elevated temperatures used for growth. Another possibility is that these impurity particles were already on the surface of the Cu before CVD growth. During graphene growth these impurities have two roles: (1) they serve as nucleation sites for graphene monolayer and bilayer growth, and (2) they can act as obstacles to stop continuous graphene growth. For example, in figure 4.14(a), the white thin lines represent incomplete graphene areas, and some white particles can also be found in these areas as demonstrated by Kim *et al.* [51]. The presence of the impurity particles as shown in figure 4.14(c) stops graphene growth underneath.

Figure 4.15 shows the Raman shifts of the G and $2D$ peaks with respect to the nitric acid etch time. When compared with the graphene grown on foils etched for 30 sec, the G and $2D$ peaks of the graphene grown on samples etched for 90 sec are observed shifted to a higher wave number (blue shift) by 6 cm^{-1} and 10 cm^{-1}. Table 4.2 shows the position of the G and $2D$ peaks position for graphene grown on samples with different nitric acid etching times. As above, the blue shift of the G and $2D$ Raman lines can be attributed to an increased level of graphene doping with etching time, suggesting the longer etch times produce cleaner (and possibly smoother) foil surfaces, so promoting coupling between the

graphene and the copper substrate.

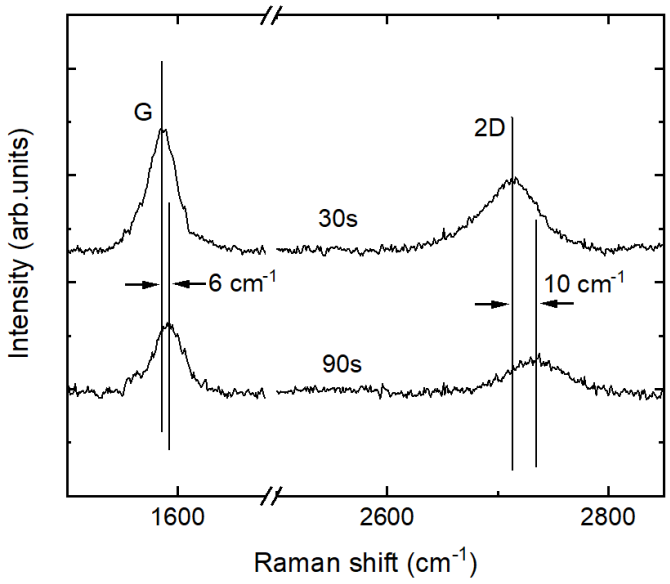

Figure 4.15: *Raman shifts of the G and 2D peaks for graphene grown on copper samples etched with nitric acid for different times.*

Sample	G **peak position** cm^{-1}	**2**D **peak position** cm^{-1}
Nitric acid treated Cu (30s)	1586.6 ± 0.3	2718.4 ± 0.6
Nitric acid treated Cu (45s)	1588 ± 0.1	2720.4 ± 0.4
Nitric acid treated Cu (60s)	1587.6 ± 0.3	2718.4 ± 0.6
Nitric acid treated Cu (90s)	1592 ± 0.1	2728 ± 1

Table 4.2: *The position of the G and 2D peaks position for graphene grown on nitric acid etched Cu.*

4.4.1 Effect of growth time on graphene film formation

To explore the influence of growth time on graphene coverage and film quality, several samples were grown on acetic acid etched copper foils at a growth temperature of 1065 °C using different growth times (4, 6, 9, and 12 minutes) are shown in 4.16. Figure 4.17 shows the evolution of graphene coverage as a function of growth time. Initially coverage increases from 58% to 82% almost linearly, as might be expected. However, the graphene coverage is found not to increase beyond that point. As discussed above, at saturation coverage of carbon precursor we expect the growth of a sub-monolayer, rather than complete monolayer of graphene to occur [12]. Hence, it can be concluded that these conditions of substrate treatment, temperature and flow rate are insufficient to produce a supersaturated surface and hence complete graphene surface coverage.

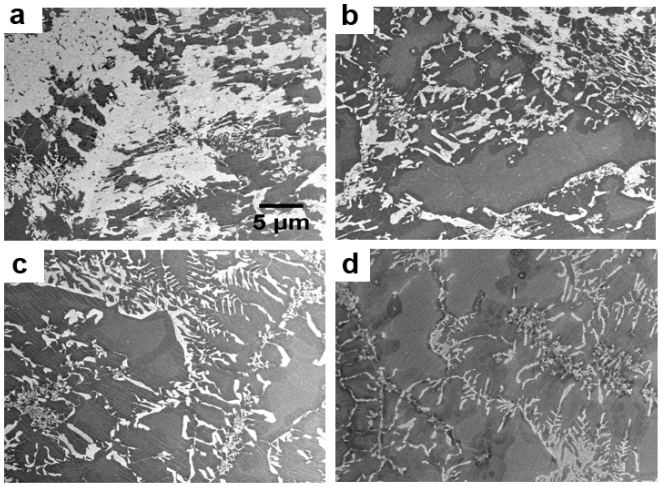

Figure 4.16: *Graphene grown on acetic acid etched copper foils at a growth temperature of 1065* °C *using different growth times (4, 6, 9, and 12 min) a,b,c,d respectively. The scale bar is the same for all images*

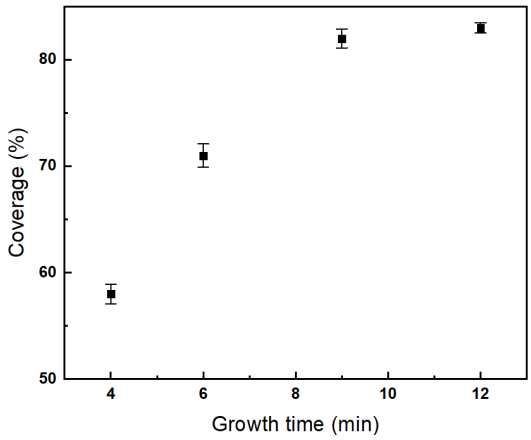

Figure 4.17: *Variation of graphene/FLG coverage on copper foils etched with AA as a function of growth time at a temperature of 1065* °C and CH_4 flow rate of 1 sccm.

4.5 Conclusion

In this work, we have explored the effects of methane flow rate, growth temperature, and the influence of surface pre-treatment on graphene growth. Graphene synthesis at a high concentration of methane results in a graphene multilayer with a high defect intensity which can delaminate from the copper substrate. Under these conditions there is no self-limitation of growth to a single graphene monolayer.

The growth temperature was found to influence graphene film growth. At increasing growth temperature an increase in coverage from 58% at 1065 °C to 93% at 1075 °C was observed on acetic acid treated surfaces, indicating the dominance of the rate of dehydrogenation in determining film coverage. Given that, at lower growth temperatures, it was found that high precursor concentrations led to multilayer growth, the balance between temperature and precursor concentration in order to produce a full coverage of predominantly monolayer graphene is clearly somewhat delicate.

Surface pre-treatments were also found to substantially influence graphene film growth. Submonolayer films were found to have island sizes which increased in the order of acetic acid treatment → electropolishing → nitric acid etching. This behaviour could be understood in terms of a decrease in the number of nucleation sites due to the presence of defects and impurities. Raman spectroscopy demonstrated that improvements in island size correlated with the degree of hole doping within the graphene, demonstrating a increased coupling between the substrate and the graphene which could be understood in terms of improved sample cleanliness. A similar variation in the degree doping was observed for (almost) complete monolayer graphene films on nitric acid etched films as a function of nitric acid treatment time, supporting the assertion that this approach is particularly effective in surface cleaning and indicating that longer treatment times are the most effective.

Finally, the effects of growth time were explored on acetic acid-treated surfaces to determine if the 'best' growth conditions for temperature and precursor flow rate could create complete monolayer films. However, it was found that coverages saturated at 82%, indicating that the growth conditions were insufficient to produce a supersaturated surface.

References

[1] Xuesong Li, Weiwei Cai, Jinho An, Seyoung Kim, Junghyo Nah, Dongxing Yang, Richard Piner, Aruna Velamakanni, Inhwa Jung, Emanuel Tutuc, et al. Large-area synthesis of high-quality and uniform graphene films on copper foils. *Science*, 324(5932):1312–1314, 2009.

[2] Gang Hee Han, Fethullah Gunes, Jung Jun Bae, Eun Sung Kim, Seung Jin Chae, Hyeon-Jin Shin, Jae-Young Choi, Didier Pribat, and Young Hee Lee. Influence of copper morphology in forming nucleation seeds for graphene growth. *Nano Letters*, 11(10):4144–4148, 2011.

[3] HoKwon Kim, Cecilia Mattevi, M Reyes Calvo, Jenny C Oberg, Luca Artiglia, Stefano Agnoli, Cyrus F Hirjibehedin, Manish Chhowalla, and Eduardo Saiz. Activation energy paths for graphene nucleation and growth on cu. *ACS nano*, 6(4):3614–3623, 2012.

[4] Kemal Celebi, Matthew T Cole, Jong Won Choi, Frederic Wyczisk, Pierre Legagneux, Nalin Rupesinghe, John Robertson, Kenneth BK Teo, and Hyung Gyu Park. Evolutionary kinetics of graphene formation on copper. *Nano Letters*, 13(3):967–974, 2013.

[5] Pierre Trinsoutrot, Caroline Rabot, Hugues Vergnes, Alexandru Delamoreanu, Aziz Zenasni, and Brigitte Caussat. The role of the gas phase in graphene formation by CVD on copper. *Chemical Vapor Deposition*, 20(1-2-3):51–58, 2014.

[6] Zhengtang Luo, Ye Lu, Daniel W Singer, Matthew E Berck, Luke A Somers, Brett R Goldsmith, and AT Charlie Johnson. Effect of substrate roughness and feedstock concentration on growth of wafer-scale graphene at atmospheric pressure. *Chemistry of Materials*, 23(6):1441–1447, 2011.

[7] Sreekar Bhaviripudi, Xiaoting Jia, Mildred S Dresselhaus, and Jing Kong. Role of kinetic factors in chemical vapor deposition synthesis of uniform large area graphene using copper catalyst. *Nano letters*, 10(10):4128–4133, 2010.

[8] Kiyeol Lee and Jongpil Ye. Significantly improved thickness uniformity of graphene monolayers grown by chemical vapor deposition by texture and morphology control of the copper foil substrate. *Carbon*, 100:441–449, 2016.

[9] Qingkai Yu, Jie Lian, Sujitra Siriponglert, Hao Li, Yong P Chen, and Shin-Shem Pei. Graphene segregated on ni surfaces and transferred to insulators. *Applied Physics Letters*, 93(11):113103, 2008.

[10] Alfonso Reina, Xiaoting Jia, John Ho, Daniel Nezich, Hyungbin Son, Vladimir Bulovic, Mildred S Dresselhaus, and Jing Kong. Large area, few-layer graphene films on arbitrary substrates by chemical vapor deposition. *Nano Letters*, 9(1):30–35, 2009.

[11] Xiangping Chen, Lili Zhang, and Shanshan Chen. Large area cvd growth of graphene. *Synthetic Metals*, 210:95–108, 2015.

[12] Xuesong Li, Carl W Magnuson, Archana Venugopal, Jinho An, Ji Won Suk, Boyang Han, Mark Borysiak, Weiwei Cai, Aruna Velamakanni, Yanwu Zhu, et al. Graphene films with large domain size by a two-step chemical vapor deposition process. *Nano Letters*, 10(11):4328–4334, 2010.

[13] Ivan Vlassiouk, Murari Regmi, Pasquale Fulvio, Sheng Dai, Panos Datskos, Gyula Eres, and Sergei Smirnov. Role of hydrogen in chemical vapor deposition growth of large single-crystal graphene. *ACS Nano*, 5(7):6069–6076, 2011.

[14] Yong Cheol Shin and Jing Kong. Hydrogen-excluded graphene synthesis via atmospheric pressure chemical vapor deposition. *Carbon*, 59:439–447, 2013.

[15] Xianfeng Zhang, Jing Ning, Xianglong Li, Bin Wang, Long Hao, Minghui Liang, Meihua Jin, and Linjie Zhi. Hydrogen-induced effects on the CVD growth of high-quality graphene structures. *Nanoscale*, 5(18):8363–8366, 2013.

[16] Guohong Li, Adina Luican, and Eva Y. Andrei. Scanning tunneling spectroscopy of graphene on graphite. *Phys. Rev. Lett.*, 102:176804, Apr 2009.

[17] https://shellbuckling.com/presentations/soft shells membranes/pages/page 15.html, 23/03/2022.

[18] Wenzhong Bao, Feng Miao, Zhen Chen, Hang Zhang, Wanyoung Jang, Chris Dames, and Chun Ning Lau. Controlled ripple texturing of suspended graphene and ultrathin graphite membranes. *Nature Nanotechnology*, 4(9):562–566, 2009.

[19] JB Nelson and DP Riley. The thermal expansion of graphite from 15 c. to 800 c.: part i. experimental. *Proceedings of the Physical Society (1926-1948)*, 57(6):477, 1945.

[20] Yimin A Wu, Ye Fan, Susannah Speller, Graham L Creeth, Jerzy T Sadowski, Kuang He, Alex W Robertson, Christopher S Allen, and Jamie H Warner. Large single crystals of graphene on melted copper using chemical vapor deposition. *ACS Nano*, 6(6):5010–5017, 2012.

[21] AN Obraztsov, EA Obraztsova, AV Tyurnina, and AA Zolotukhin. Chemical vapor deposition of thin graphite films of nanometer thickness. *Carbon*, 45(10):2017–2021, 2007.

[22] Shaahin Amini, Javier Garay, Guanxiong Liu, Alexander A Balandin, and Reza Abbaschian. Growth of large-area graphene films from metal-carbon melts. *Journal of Applied Physics*, 108(9):094321, 2010.

[23] Peter Sutter, Jerzy T Sadowski, and Eli Sutter. Graphene on pt (111): Growth and substrate interaction. *Physical Review B*, 80(24):245411, 2009.

[24] George Wells et al. *Growth and Defect Formation in Graphene*. PhD thesis, Durham University, 2016.

[25] Farhana Zaman. *Characterization of selective epitaxial graphene growth on silicon carbide: Limitations and opportunities*. Georgia Institute of Technology, 2012.

[26] GF Sun, JF Jia, QK Xue, and L Li. Atomic-scale imaging and manipulation of ridges on epitaxial graphene on 6h-sic (0001). *Nanotechnology*, 20(35):355701, 2009.

[27] LM Malard, Marcos Assunção Pimenta, Gene Dresselhaus, and MS Dresselhaus. Raman spectroscopy in graphene. *Physics Reports*, 473(5-6):51–87, 2009.

[28] Ye Xiao, HoKwon Kim, Cecilia Mattevi, Manish Chhowalla, Robert C Maher, and Lesley F Cohen. Influence of cu substrate topography on the growth morphology of chemical vapour deposited graphene. *Carbon*, 65:7–12, 2013.

[29] EH Martins Ferreira, Marcus VO Moutinho, F Stavale, Márcia Maria Lucchese, Rodrigo B Capaz, Carlos Alberto Achete, and A Jorio. Evolution of the Raman spectra from single-, few-, and many-layer graphene with increasing disorder. *Physical Review B*, 82(12):125429, 2010.

[30] Cinzia Casiraghi, S Pisana, KS Novoselov, Andre K Geim, and AC Ferrari. Raman fingerprint of charged impurities in graphene. *Applied Physics Letters*, 91(23):233108, 2007.

[31] Andrea C Ferrari, Jannik C Meyer, Vittorio Scardaci, Cinzia Casiraghi, Michele Lazzeri, Francesco Mauri, Stefano Piscanec, Dingde Jiang, Konstantin Sergeevich Novoselov, Siegmar Roth, et al. Raman spectrum of graphene and graphene layers. *Physical Review Letters*, 97(18):187401, 2006.

[32] Hye Jin Park, Jannik Meyer, Siegmar Roth, and Viera Skákalová. Growth and properties of few-layer graphene prepared by chemical vapor deposition. *Carbon*, 48(4):1088–1094, 2010.

[33] Zhenhua Ni, Yingying Wang, Ting Yu, and Zexiang Shen. Raman spectroscopy and imaging of graphene. *Nano Research*, 1(4):273–291, 2008.

[34] Kwanpyo Kim, Sinisa Coh, Liang Z Tan, William Regan, Jong Min Yuk, Eric Chatterjee, MF Crommie, Marvin L Cohen, Steven G Louie, and A Zettl. Raman spectroscopy study of rotated double-layer graphene: misorientation-angle dependence of electronic structure. *Physical Review Letters*, 108(24):246103, 2012.

[35] Alex W Robertson and Jamie H Warner. Hexagonal single crystal domains of few-layer graphene on copper foils. *Nano Letters*, 11(3):1182–1189, 2011.

[36] Shu Nie, Wei Wu, Shirui Xing, Qingkai Yu, Jiming Bao, Shin-shem Pei, and Kevin F McCarty. Growth from below: bilayer graphene on copper by chemical vapor deposition. *New Journal of Physics*, 14(9):093028, 2012.

[37] Sirui Xing, Wei Wu, Yanan Wang, Jiming Bao, and Shin-Shem Pei. Kinetic study of graphene growth: Temperature perspective on growth rate and film thickness by chemical vapor deposition. *Chemical Physics Letters*, 580:62–66, 2013.

[38] Ivan Vlassiouk, Pasquale Fulvio, Harry Meyer, Nick Lavrik, Sheng Dai, Panos Datskos, and Sergei Smirnov. Large scale atmospheric pressure chemical vapor deposition of graphene. *Carbon*, 54:58–67, 2013.

[39] Talmantaite Alina. *Kinetics of CVD graphene growth on polycrystalline copper and the influence of surface texture*. PhD thesis, Durham University, 2018.

[40] Robert M Jacobberger and Michael S Arnold. Graphene growth dynamics on epitaxial copper thin films. *Chemistry of Materials*, 25(6):871–877, 2013.

[41] Fredrik Schedin, Andrei Konstantinovich Geim, Sergei Vladimirovich Morozov, Ew W Hill, Peter Blake, Mi I Katsnelson, and Kostya Sergeevich Novoselov. Detection of individual gas molecules adsorbed on graphene. *Nature Materials*, 6(9):652–655, 2007.

[42] Anindya Das, Simone Pisana, Biswanath Chakraborty, Stefano Piscanec, Srijan K Saha, Umesh V Waghmare, Konstantin S Novoselov, Hulikal R Krishnamurthy, Andre K Geim, Andrea C Ferrari, et al. Monitoring dopants by raman scattering in an electrochemically top-gated graphene transistor. *Nature Nanotechnology*, 3(4):210–215, 2008.

[43] G. Giovannetti, P. A. Khomyakov, G. Brocks, V. M. Karpan, J. van den Brink, and P. J. Kelly. Doping graphene with metal contacts. *Physical Review Letters*, 101(2):026803, 2008.

[44] Rusen Yan, Qin Zhang, Wei Li, Irene Calizo, Tian Shen, Curt A. Richter, Angela R. Hight-Walker, Xuelei Liang, Alan Seabaugh, Debdeep Jena, Huili Grace Xing, David J. Gundlach, and N. V. Nguyen. Determination of graphene work function and graphene-insulator-semiconductor band alignment by internal photoemission spectroscopy. *Applied Physics Letters*, 101(2), 2012.

[45] T. Yoon, Q. Wu, D. J. Yun, S. H. Kim, and Y. J. Song. Direct tuning of graphene work function via chemical vapor deposition control. *Scientific Reports*, 10(1):9870, 2020.

[46] C. Klein, D. Cohen-Elias, and G. Sarusi. Controlling graphene work function by doping in a mocvd reactor. *Heliyon*, 4(12):e01030, 2018.

[47] P. O. Gartland, S. Berge, and B. J. Slagsvold. Photoelectric work function of a copper single crystal for the (100), (110), (111), and (112) faces. *Physical Review Letters*, 28(12):738–739, 1972.

[48] O. Renault, R. Brochier, A. Roule, P. H. Haumesser, B. Krömker, and D. Funnemann. Work-function imaging of oriented copper grains by photoemission. *Surface and Interface Analysis*, 38(4):375–377, 2006.

[49] Paul A. Anderson. The work function of copper. *Physical Review*, 76(3):388–390, 1949.

[50] Mouna Rafei, Vladimir Miranda La Hera, Hamid Reza-Barzegar, Eduardo Gracia-Espino, and Thomas Wågberg. Study on the electronic and structural properties of oxidized copper films. *AIP Advances*, 12(10), 2022.

[51] Soo Min Kim, Allen Hsu, Yi-Hsien Lee, Mildred Dresselhaus, Tomás Palacios, Ki Kang Kim, and Jing Kong. The effect of copper pre-cleaning on graphene synthesis. *Nanotechnology*, 24(36):365602, 2013.

Chapter 5

Chemical vapour deposition growth of monolayer and few-layer MoS_2 on Silicon substrate

This chapter discusses experiments performed to explore the growth of MoS_2 via hot-wall atmospheric-pressure chemical vapour deposition (AP-CVD). MoS_2 samples produced by this method were studied with Raman spectroscopy (RS) to determine the uniformity and the number of the layers, Scanning Electron Microscopy (SEM) to determine the morphology and the shape of the MoS_2, and X-ray photoelectron spectroscopy (XPS) to study the composition of the films. The influence of substrate growth temperature and sulphur partial pressure were explored and it was found that in the latter case the growth of MoS_2 can be described by Langmuir-Hinshelwood growth kinetics.

5.1 Introduction

Since the first production of monolayer and few-layer MoS_2 by micromechanical exfoliation there has been an enormous amount interest in this material [1]. One of the reasons that MoS_2 is highly promising is that, as discussed in Chapter 1, it possesses a tunable band gap with thickness, with an indirect band gap of 1.2 eV in the bulk evolving into a direct band gap of 1.9 eV in a single layer [2]. Such behaviour opens up many potential applications in nanoscale opto-electronics. In comparison, graphene is a zero-gap semiconductor, which makes it difficult to apply as an active layer in digital electronics as a result of its low ON:OFF ratio, while the ON:OFF ratio in MoS_2 is 1×10^8 [3].

As mentioned in detail in Chapter 1, monolayer and few-layer TMDCs can be prepared using either 'top-down' or 'bottom-up' methods. Several efforts have been reported which produce MoS_2 layers from a bulk 'parent' material. These methods include micromechanical exfoliation [1] and liquid phase exfoliation [4]. Bottom up techniques include direct sulphurization of a variety of Mo-based precursors, which include $(NH_4)_2MoS_4$ solutions deposited on substrates by dip-coating [5], thermally evaporated Mo [6] or MoO_3 [7] thin films. Thermolysis of a solid precursor containing Mo and S atoms [8] has also been reported. The MoS_2 thin films produced by the above-mentioned methods produce grains which are several micrometres in lateral size. The first synthesis of large area MoS_2 thin films was reported by Lee *et al.* in 2012 [9]. In their experiment the chemical vapour deposition (CVD) method was adopted to produce MoS_2 layers directly on substrates using MoO_3 and S powders as precursors. The substrate was first coated with reduced graphene oxide (rGO) solution, with the rGO platelets acting as seeds to facilitate the MoS_2 growth. MoO_3 and S powders were evaporated in a tube furnace at 650 °C under a N_2 flow. The resulting MoS_2 islands displayed an ordered triangular morphology with star-shaped edges and displayed significant thickness variations. The mobility of the resulting MoS_2 sheets was examined and measured to be approximately 0.02 $cm^2\ V^{-1}\ s^{-1}$ in bottom-gated transistors. This value is a few orders of magnitude less than measured in comparable exfoliated samples. Lee and co-workers attributed the lower mobility in CVD grown MoS_2 to the presence of structural defects, such as grain boundaries. However, treating the growth substrate with aromatic molecular seeds is not necessary to facilitate MoS_2 growth. Lou *et al.* first demonstrated the growth of ordered MoS_2 monolayer islands without using surface treatment [10]. Triangular MoS_2 islands produced in their experiment were identified as single crystal flakes with an edge length of 10 μm. Nevertheless, it was found that the MoS_2 islands and films nucleated at the substrate edges, dust particles, scratches or rough areas.

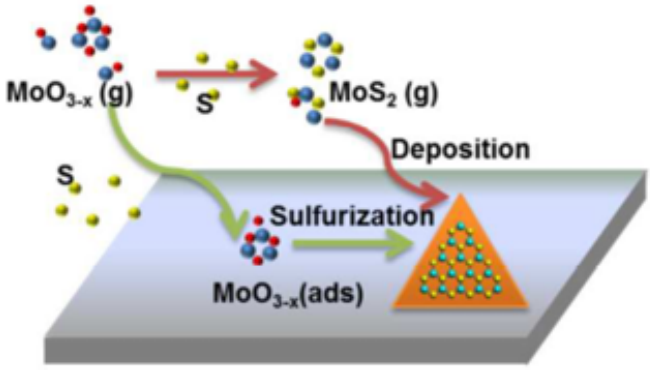

Figure 5.1: *Possible growth processes of MoS_2 by the reaction of MoO_3 and S vapour phase precursors [13].*

Significant efforts have been devoted to explain the mechanism of MoS_2 growth via CVD from MoO_3 and S precursors and there are two models which have been reported. In the first, MoO_3 and S precursors react to form volatile $MoO_{3-X}S_Y$ nanoparticles, which then adsorb and diffuse on the substrate. Further annealing and sulphurization are required for the particles to be fully converted into MoS_2 sheets [11, 12]. In the second model the reaction between MoO_3 and S occurs in the gas phase, and MoS_2 flakes directly nucleate on the substrate to produce the MoS_2 islands [13]. Figure 5.1. schematically represents the possible growth processes of MoS_2 resulting from the reaction of MoO_3 and S within these models.

In this work, we used a simple method for the synthesis of MoS_2 layers, through the direct reaction of MoO_3 powder with S powder on clean, but otherwise untreated silicon substrates with native surface oxides. This approach to CVD synthesis can, depending on the conditions selected, yield isolated MoS_2 islands or continuous films directly on a Si substrate. The MoS_2 growth process we use is similar to those which have been previously reported in the literature [14]. These studies examined the impact of varying the MoO_3 temperature and the substrate temperature but do not change the sulphur partial pressure, which is the main focus of this Chapter. We initially examine the impact of sample temperature and growth time in a similar manner to the literature in order to find 'baseline' parameters for MoS_2 monolayer and few-layer film growth and to gain insight into the growth mechanism. We then turn our attention to the effect of sulphur partial pressure (through evaporation temperature) on MoS_2 growth while keeping the temperature of MoO_3 and substrate constant. Details of the sample preparation methods are provided in Chapter 3.

5.2 Influence of substrate temperature on MoS_2 film growth

Figure 5.2 shows a series of SEM images of MoS_2 grown using Method #1, described in Chapter 3, which is based upon the approach of Balendhran and co-workers [8]. A series of samples produced at increasing substrate temperatures with that of the MoO_3 and S precursors fixed. In the SEM micrographs presented in Figure 5.2 it can be seen that the density of MoS_2 nucleation sites increases with temperature, as does coverage, and is accompanied with a deterioration in the uniformity of the MoS_2 film thickness [14], with the presence of particles (white dots) on the surface at 700 °C and 650 °C, which are claimed to be molybdenum oxysulphides, $MoO_{3-X}S_Y$ [12]. An example is shown yellow arrow in figure 5.2a. In contrast, when the substrate temperature is reduced to 650°C as shown in Figure 5.2b and c, a flatter, more uniform, surface morphology becomes apparent and there is improved homogeneity in the film thickness. When substrate temperature is further reduced to 550 °C, the nucleation density of MoS_2 decreases further with the formation of isolated triangular-shaped monolayer islands, reflecting a high degree of internal structural order, with a 3 μm^{-2} island density Figure 5.2d.

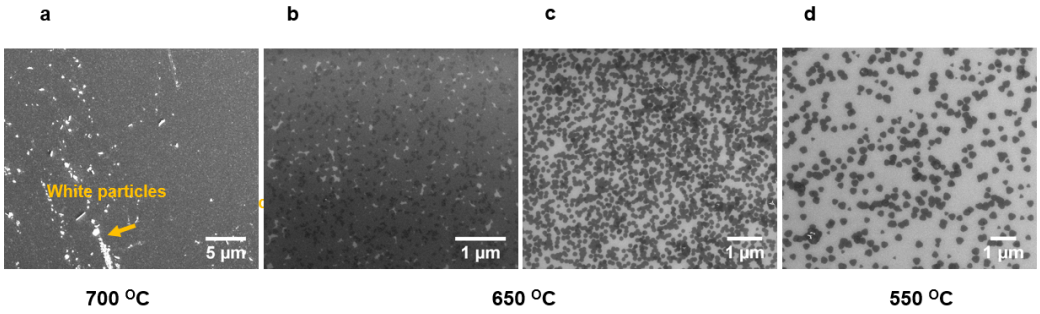

Figure 5.2: *Morphology of deposited films at substrate temperatures of (a) 700 °C, (b,c) 650 °C, and (d) 550 °C. Crystals of $MoO_{3-X}S_Y$ are not converted into MoS_2 through post-deposition reaction with sulphur, and therefore, they are deposited on the surface and grow as shown on a.*

A Raman spectrum from a the bulk sample of MoS_2, sourced commercially, is shown in Figure 5.3a and displays the characteristic E^1_{2g} and A_{1g} vibrational peaks at 382.8 cm^{-1} and 408.4 cm^{-1} respectively, which were discussed in Chapter 2. For monolayer and few-layer MoS_2, the positions of these modes shift with respect to their bulk counterpart 5.4 [15]. Raman spectra obtained from samples grown at a substrate temperature of 700 °C show peaks at the same position for the bulk MoS_2, indicating that the film is more than 5 layers thick. As the substrate temperature decreased there was a shift in frequency indicating the number of layers reduced. In Figure 5.3b, a spectrum is presented obtained from a MoS_2 film grown at a sample temperature of 650 °C. The position of peaks indicates the

formation of a few-layered MoS_2 film with a thickness of 2-3 layers.

The dependence of MoS_2 coverage and thickness on substrate temperature in AP-CVD growth is a strong indication of the role the substrate plays in the growth process. As discussed in section 5.1, two models have been proposed for the mechanism by which MoS_2 nucleates and grows at the surface of a substrate - namely by either surface or gas phase reaction. The results reported here support the concept of a surface-based reaction process in which precursors adsorb on the silicon native oxide surface and react. In particular, if the MoS_2 formation were to occur in the gas phase, one would expect the rate of desorption versus adsorption of precursor species to increase with temperature and hence lead to a decrease in surface coverage.

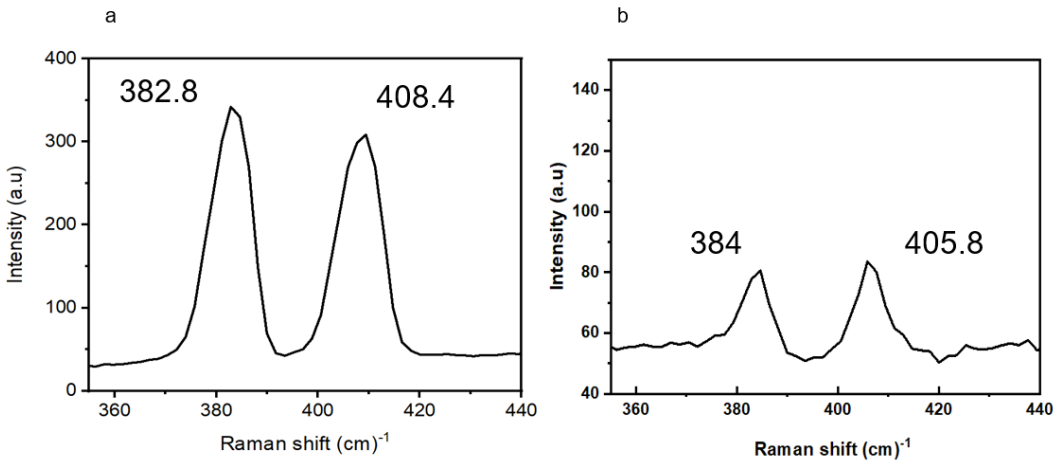

Figure 5.3: *(a) Raman spectrum obtained from a bulk MoS_2 sample. (b) Raman spectrum obtained from sample in Figure 5.2 grown at a substrate temperature of 650 °C. Numbers indicate the positions of the peaks in* cm^{-1}.

Although a high surface coverage of thin MoS_2 was found using this condition, the samples were found not to be uniform and contained oxysulphide particles. The growth process was uncontrolled, making it unlikely that a uniform continuous film can be made under these conditions. To solve this problem, external heating was applied to the furnace to control the temperature of the sulphur. For more details on external heating and the modified MoS_2 growth system see Chapter 3.

The effects of growth conditions on the deposition of MoS_2 films on silicon substrates using Method #2 described in chapter 3 was also investigated. Initial growth of MoS_2 using external heating was made by introducing sulphur to the system after the furnace reached its target (growth) temperature of 700°C [12]. Growth was controlled using the

technique of 'staggered' evaporation of precursors, represented graphically in Figure 3.9a in chapter 3. SEM images taken from such samples are shown in Figure 5.5 and indicate that films grown under this set of conditions contain patches of $MoO_{3-X}S_Y$ on samples grown at a substrate temperature of 700°C and 650°C, which is similar to observations made on samples grown by Method #1. An example is shown circled in yellow in figure 5.5. From this result we can draw the conclusion that if MoO_3 is allowed to deposit on the substrate before a sufficient sulphur flux is available, crystals of $MoO_{3-X}S_Y$ grow on the surface, which cannot be converted to MoS_2 via post-deposition sulphurisation reactions under the conditions of sulphur flux employed.

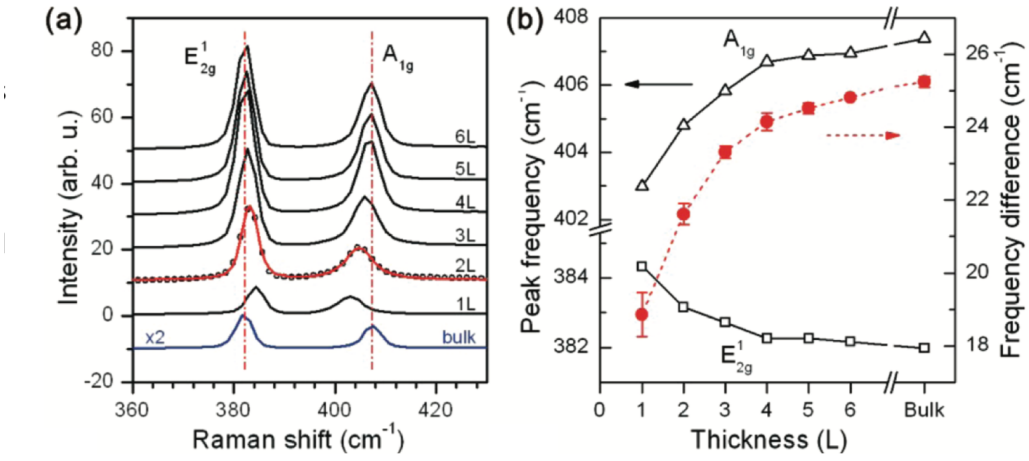

Figure 5.4: *(a) Raman spectra for bulk and micromechanically exfoliated MoS_2 as a function of thickness. (b) Variation of the position of the E^1_{2g} and A_{1g} vibrational modes of MoS_2 as a function of thickness [15].*

In Figure 5.6, the coverage (a, d), island area (b, e), and the number density (c, f) of MoS_2 films are plotted as a function of substrate temperature for two different sulphur evaporation temperatures, 160 and 200 °C. For a constant sulphur temperature and various sample temperatures, as shown in figure 5.6, coverage and average island size increase with increasing sample temperature. However, there is insufficient data to determine the variation of nucleation density, in particular for a sulphur temperature of 160 °C, due to the high coverage leading to island coalescence which prevents an accurate determination of the density of islands (or equivalently nucleation density). With a fixed sample temperature, coverage and area are reduced with increasing sulphur temperature, but the nucleation density is increased, an observation which will be examined more closely in section 5.3. From the continued presence of particulate structures on the surface after growth, highlighted in yellow in Figure 5.5, it was realized that although the density of

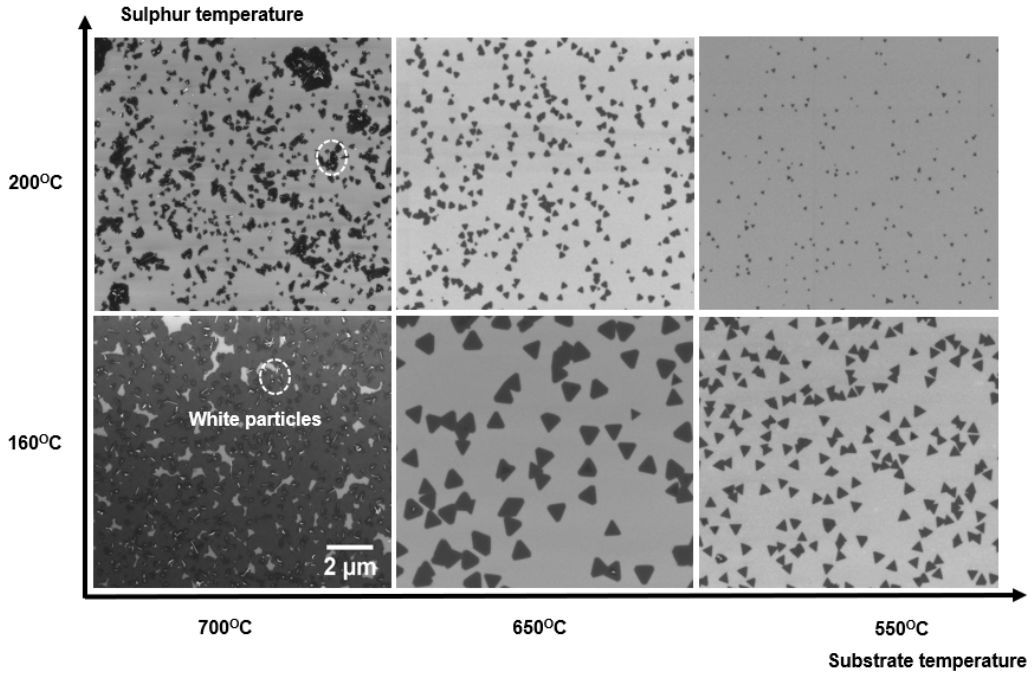

Figure 5.5: *SEM images showing the morphology of deposited films at substrate temperatures of 700* °C*, 650* °C*, and 550* °C *and sulphur temperatures of 160* °C*, 200* °C*. Crystals of* $MoO_{3-X}S_Y$ *are not converted into* MoS_2 *through post-deposition reaction with sulphur and therefore, they deposited on the surface and grow. The scale bar is the same for all images.*

$MoO_{3-x}S_Y$ particles is lower than that for samples grown by Method #1 they cannot be eliminated using this approach.

To mitigate the presence of $MoO_{3-x}S_Y$, the importance of the control and timing of evaporation of the precursor materials was investigated. This was achieved by controlling the time of sulphur temperature and introducing it into the growth zone ten minutes before the furnace reaches the target temperature. As illustrated in the temperature profile shown in Figure 3.9(b) in chapter 3, sulphur vapour was introduced to the growth area when the furnace temperature reached 500 °C with the expectation that the temperature of the MoO_3 precursor upstream was enough to evaporate it.

The results of applying the temperature profile for 'co-evaporation' Figure 3.9(b) in chapter 3, are demonstrated by the SEM images shown in Figure 5.7(a-i) with different growth temperatures and a different growth times. It can be seen that there is an absence of the particulate species associated with partially sulphurised molybdenum oxides under all the growth conditions studied. When the growth temperature is at 700°C, for a growth

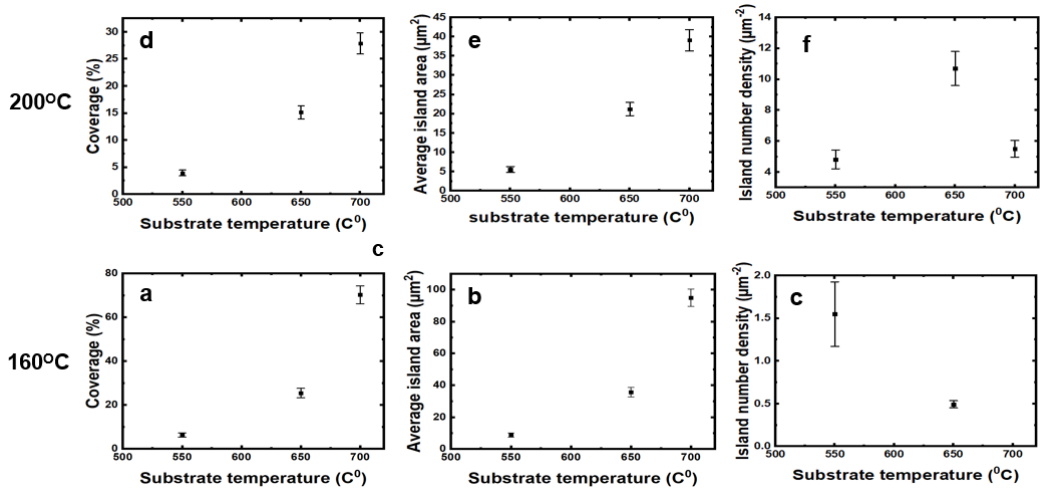

Figure 5.6: *MoS_2 coverage (a, d), island area (b, e), and number density (c, f) of samples grown at various sulphur temperatures and substrate temperatures. Coverage and average island size increase with increasing sample temperature with a fixed sulphur temperature and varying sample temperatures, but nucleation density decreases. With a constant sample temperature, raising sulphur temperature reduces coverage and area size while increases nucleation density, see the difference on scales.*

time of 20 min, the coverage is low at 11%, with a 16 μm^2 average island size. Figure 5.7(a) shows that the surface of the substrate is partially covered by isolated MoS_2 islands. When the growth time is increased to 60 min, the MoS_2 film still does not cover the substrate surface, as shown in figure 5.7(d). The average island area increases to 34 μm^2, with a surface coverage of about 25%. When the growth time was increased to 120 min in (g), the surface coverage decreased to 23%, with 32 μm^2 being the average size. However, the density of the islands for 120 min growth was 2 μm^{-2}, higher than at the other growth times.

SEM measurements on MoS_2 grown at various growth times and substrate temperatures show that there is a significant variation in the results. In Figure 5.8 the coverage (a, d, g), island area (b, e, h), and the number density (c, f, i) of MoS_2 islands are plotted as a function of growth time for the three different substrate temperatures. When the substrate temperature is increased from 550°C to 700°C for a fixed growth time, the coverage slowly increases as seen in (a, d, g). MoS_2 island area increases with growth time from 20 min to 120 min, Figure 5.8 (b, e, h), accompanied by an increase in the nucleation density as displayed in Figure 5.8 (c f, i). At a substrate temperature of 700°C, the nucleation density increased with growth from 60 min to 120 min of growth time in Figure 5.8 (c), but the coverage and island area were still the same to within experimental uncertainty, as shown in Figure 5.8 a,b. It therefore appears that, under these conditions, a growth time of more than 120 min may not make a significant difference in comparison from 60 min growth time.

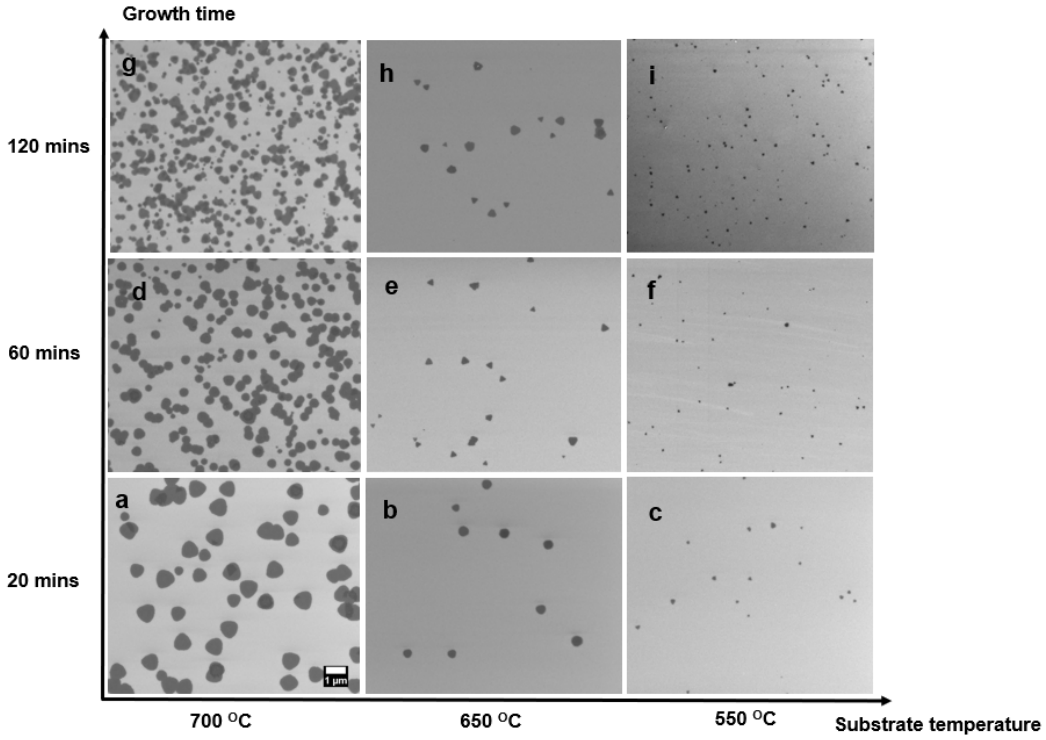

Figure 5.7: *Morphology of MoS_2 films produced at sample temperature of 700* °C*, 650* °C *and 550* °C *at various growth times. The scale bar is the same for all images.*

5.3 The effect of sulphur partial pressure on MoS_2 growth

5.3.1 Morphology and Structure

In order to explore the influence of sulphur temperature and hence partial pressures on the growth of MoS_2 a series of experiments were conducted using the Method #2 and the growth profile illustrated in Figure 3.9(c), chapter 3. The sulphur was introduced into the carrier gas stream by heating to fixed temperatures which lay in the range between (140°C - 250°C). The temperature profile chosen resulted in the sulphur reaching its desired temperature in 10 min, at the same time that the substrate reached its target temperature.

The temperature of the sample plays a crucial role in increasing MoS_2 size and, therefore, increasing the coverage of MoS_2 film [14]. When the temperature of the substrate increases, reactant species that absorbed on the substrate will diffuse around the substrate. The higher the temperature of the substrate, the further they can migrate and nucleate. Figure 5.9 shows SEM images of the as-grown MoS_2 with the corresponding sulphur evaporation

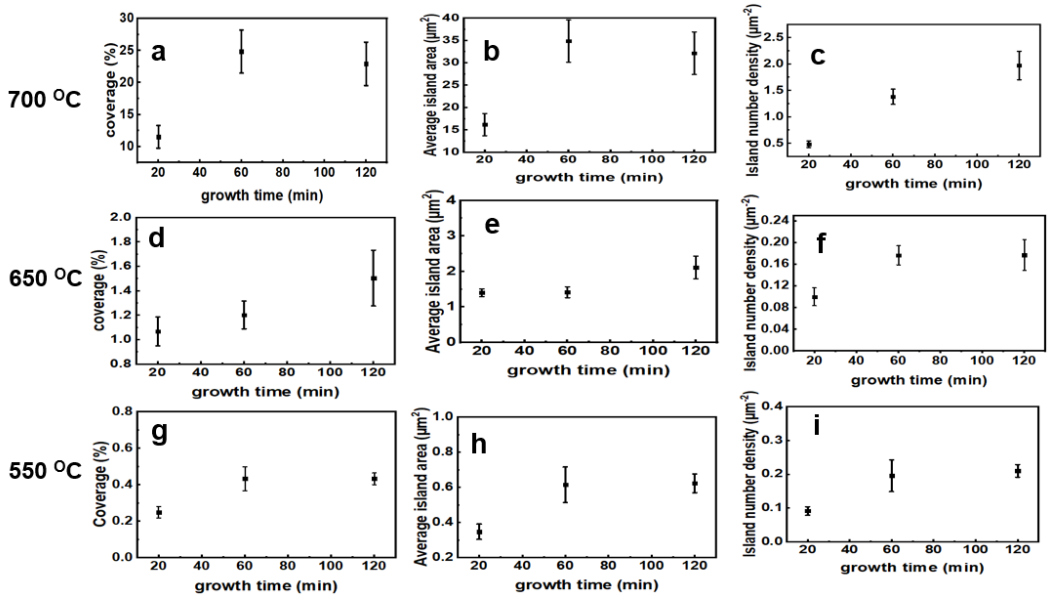

Figure 5.8: *MoS_2 coverage (a, d, g), island area (b, e, h), and number density (c, f, i) of samples grown at various growth times and substrate temperatures.*

temperature and the substrate temperature. We observe that as the substrate temperature increased from 550 °C to 650 °C, the size of the islands increase, and the nucleation density decreases. This could be because, at higher temperatures, precursors can travel further until they meet a neighbouring island rather than starting new nuclei, and therefore the size of the island increases as the substrate gets hotter. Precursors at low temperature (550 °C) on the other hand can only diffuse a smaller distance and are more likely to becomes trapped at surface defects, leading to a high nucleation density when the substrate temperature decerases. For a constant sulphur temperature and varied sample temperatures, as shown in figure 5.9, coverage increases with increasing sample temperature, whereas island size increases but island density decreases. Raman spectra obtained from samples grown by this approach, such as that shown in Figure 5.10 indicate that MoS_2 islands grown under these conditions are typically 3 layers thick as described in Figure 5.4.

In Figure 5.11 the coverage (a, b, e), island area (c, f), and the number density (d, g) of MoS_2 are plotted as a function of each temperature. For constant growth temperatures, the coverage is reduced when the sulphur temperature is increased from 140 °C to 250 °C, while at a constant sulphur temperature, the coverage decreases when the sample temperature reduced as shown in a, b, and e. MoS_2 area size increases from low substrate temperature to high temperature in (f, c), accompanied by low nucleation density as displayed in (d, g). A similar observation regarding the reduction of MoS_2 coverage with increasing sulphur evaporation temperature was made by Kang and co-workers who reported that in their

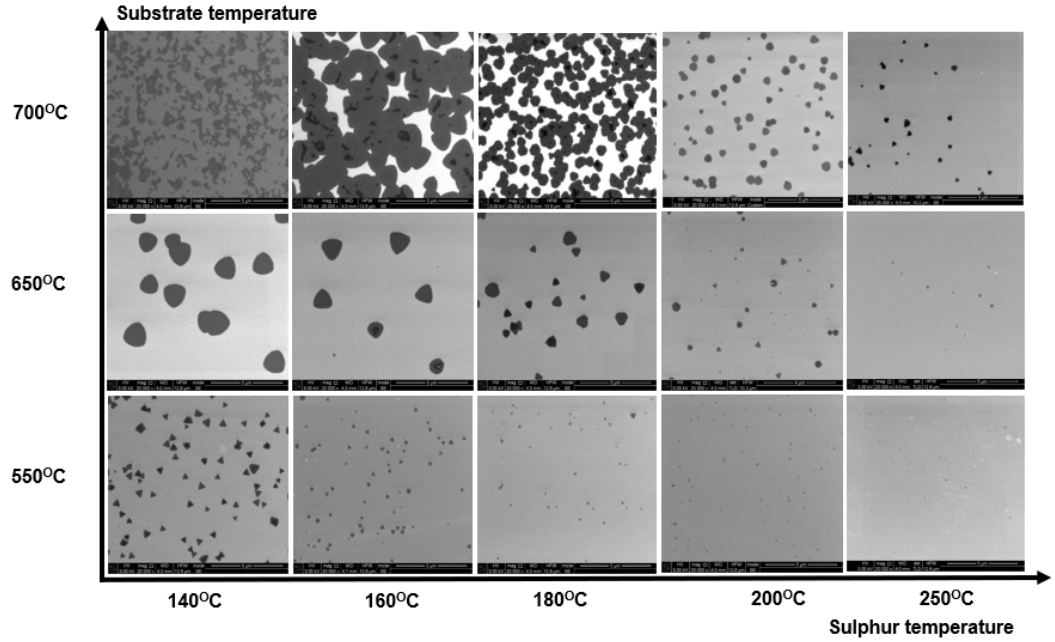

Figure 5.9: *SEM images illustrating how the MoS_2 growth depends on both sulphur evaporation temperature and the substrate temperature.*

study MoS_2 coverage reduced on the surface and island size decreased when concentrations of sulphur were high, but they did not investigate this in detail [16].

Having found the highest MoS_2 coverage for a sulphur evaporation temperature of 140 °C, it was therefore considered logical to reduce this to 120 °C. However, employing a sulphur evaporation temperature of 120 °C resulted in a sharp decrease of coverage on the surface at substrate temperatures of 700 °C and 650 °C, Figure 5.12. The MoS_2 coverage at 700 °C and 650 °C was found to be at 5% and 1.5%, respectively, while the coverage at 550 °C growth substrate was at 16.5%. As before species which could be associated with the formation of molybdenum oxides or oxysulphides could be observed indicating that under these growth conditions insufficient sulphur was available to fully convert molybdenum oxides to MoS_2.

The shapes of the MoS_2 islands observed are influenced by sulphur concentration. Figure 5.5 shows that MoS_2 has a very well-defined triangular island morphology under the 'staggered' evaporation condition. However, when using the co-evaporation condition, the islands are less sharply defined at substrate temperatures of 700 °C and 650 °C, as shown in Figure 5.9. The assumption we make is that as sulphur evaporation temperature decreases the concentration of adsorbed sulphur decreases and precursor species would be

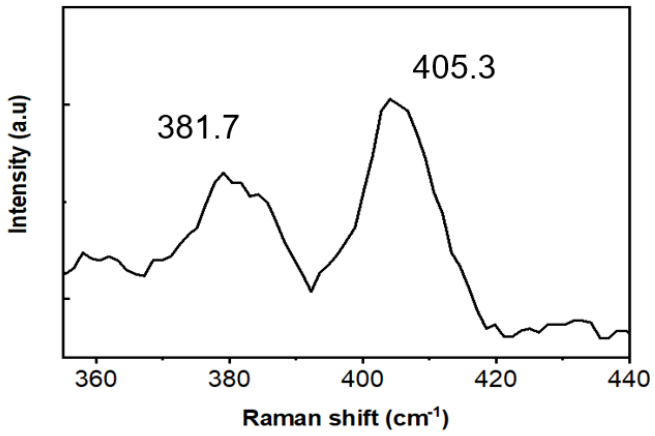

Figure 5.10: *Raman spectra obtained from sample in Figure 5.9a. Numbers indicate the Raman shifts of the two peaks.*

able to diffuse more freely. Species can arrange themselves easily into the most energetically favourable configurations, and the nucleation occurs at the MoS_2 edge [16]. On the other hand, if there is a lot of blocking on the surface site due to a high sulphur concentration, the precursor mobility might be reduced. We conclude that the crystallinity reduces as sulphur concentration increases on the surface.

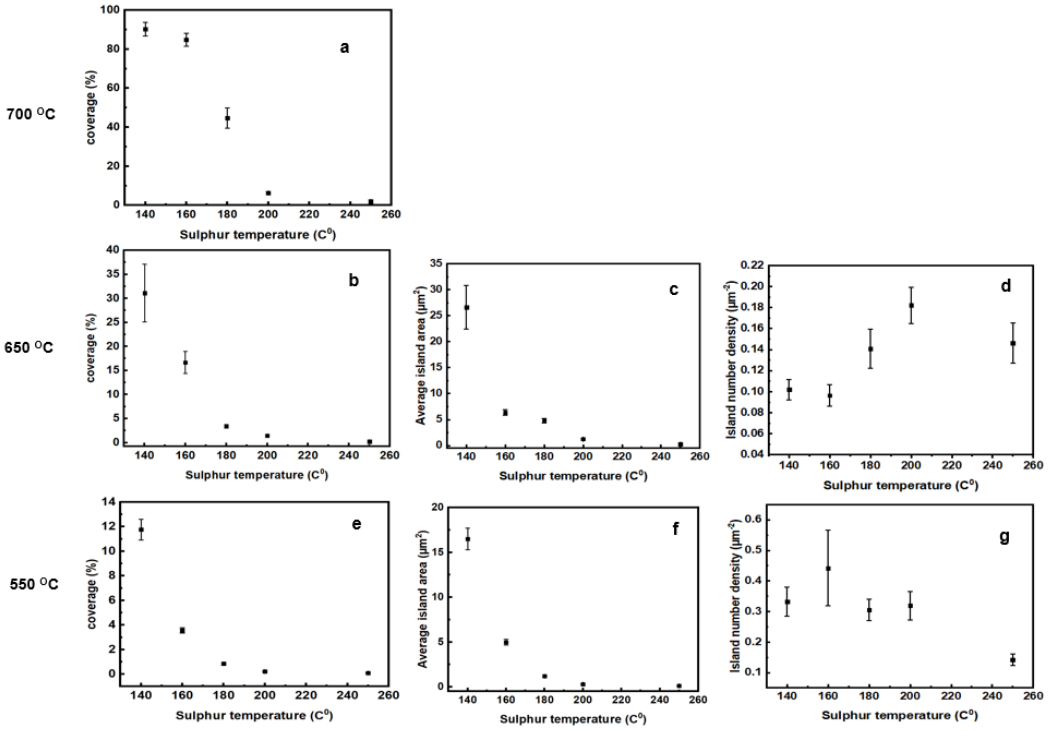

Figure 5.11: *MoS_2 coverage (a, b, e), island area (c, f), and number density (d, g) for samples grown at various sulphur evaporation temperatures and substrate temperatures. The coverage decreases when the sulphur temperature is increased from 140 °C to 250 °C for constant growth temperatures, while the coverage decreases when the sample temperature is reduced at a constant sulphur temperature.*

5.3.2 Langmuir-Hinshelwood mechanism

The Langmuir-Hinshelwood mechanism involves a bi-component reaction in which the two reactant species are adsorbed onto a surface Figure 5.13. The product of this reaction may remain absorbed into the surface, or may desorb from the surface once the reaction is completed.

The Langmuir-Hinshelwood has been extensively used to describe reaction processes in surface chemistry and is used to explain the kinetics of growth where the reactant species are in competition for common adsorption sites. The apparently counter-intuitive reduction of MoS_2 growth with increasing sulphur evaporation temperature can be explained by appeal to this model, as will be described below. Although a reduction in MoS_2 coverage with increasing sulphur growth temperature has previously been observed in the literature, no explanation for this phenomenon has previously been advanced.

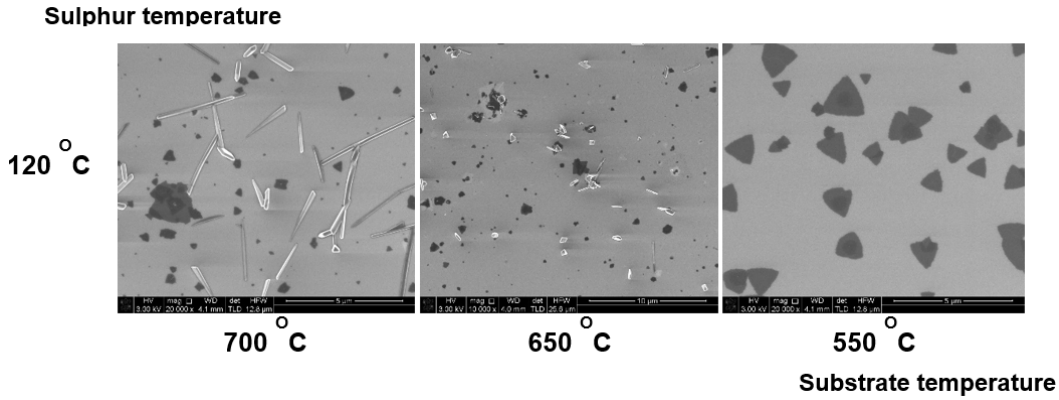

Figure 5.12: *SEM images show how the coverage at high growth temperatures is reduced by reducing the sulphur evaporation temperature to 120 °C. Crystals of $MoO_{3-X}S_Y$ are formed on the surface when the sulphur vapour is insufficient. They do not convert into MoS_2 during reaction growth.*

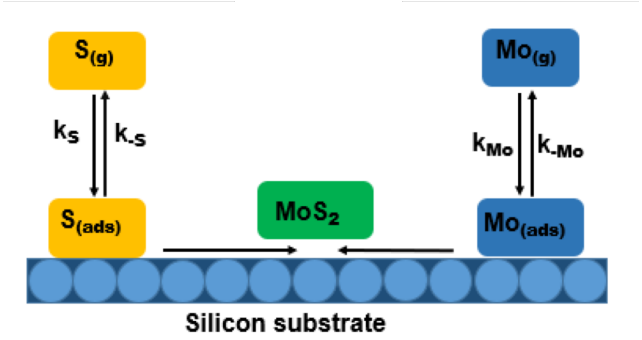

Figure 5.13: *Langmuir-Hinshelwood model, where the two reactant species, Mo and S, compete for the same surface locations on the Si substrate.*

In a surface reaction between the two adsorbed species the reaction rate can be expressed by:

$$Rate = k\theta_{Mo}\theta_S, \tag{5.1}$$

where k is the rate constant for the reaction and θ_{Mo} and θ_S are the fractional surface coverage of Mo and S, respectively. In this treatment, 'Mo' and 'S' are used as shorthand for the Mo and S rich precursor species that react together to form MoS_2 – we do not assume that they are necessarily atomic Mo and S. This reaction is considered to be the rate determining (slowest) step and hence defines k. The surface coverage can be determined by the Langmuir adsorption isotherm which, for a single species, is given by:

$$\theta = \frac{KP}{(1+KP)}, \tag{5.2}$$

where θ is the fractional surface coverage, which can take values between 0 and 1, K is the rate of adsorption onto/desorption from a species on a solid surface and P is the partial pressure of that species (at equilibrium rates of adsorption and desorption will be equal to one another). Although the Langmuir isotherm is relatively simple it is still capable of providing insight into the varation of surface coverage with adsorbant partial pressure. A number of assumptions are made within this model, which include the presence of a fixed number of adsorption sites available to the adsorbant and that saturation of the surface occurs when all these sites are occupied and that the adsorption/desorption process and associated rate constants are independent of coverage.

If two species ('Mo' and 'S') compete for the same surface sites, their individual coverage can be written as:

$$\Theta_{Mo} = \frac{k_{Mo}P_{Mo}}{1 + k_{Mo}P_{Mo} + k_S P_S}$$

and

$$\Theta_S = \frac{k_S P_S}{1 + k_{Mo}P_{Mo} + k_S P_S}.$$

Note that we have used the equality between the rates of adsorption and desorption shown in Figure 5.13, $k_{Mo} = k_{-Mo}$ and $k_S = k_{-S}$. These expression for coverage, when combined with equation 5.1, lead to a MoS_2 formation rate given by:

$$Rate = kC_S^2 \frac{k_S k_{Mo} P_S P_{Mo}}{(1 + k_S P_S + k_{Mo} P_{Mo})^2}, \tag{5.3}$$

where C_S is the concentration of surface adsorption sites. If the product of the rate of adsorption of the Mo-rich species is much lower than that of the S containing species, $k_{Mo}P_{Mo} << k_S P_S$, the rate becomes:

$$Rate = kC_S^2 \frac{k_{Mo} k_S P_{Mo} P_s}{(1 + k_S P_S)^2}. \tag{5.4}$$

If the Mo is only weakly adsorbed, such that $k_S P_S >> 1$, the equation above becomes:

$$Rate = kC_S^2 \frac{k_{Mo} P_{Mo}}{k_S P_S}. \tag{5.5}$$

From this expression for the reaction rate for MoS_2 formation, it can clearly be seen that if the partial pressure of sulphur, P_S increases the reaction rate will decrease, in fact the order of the reaction is minus one with respect to the sulphur partial pressure. This behaviour can be explained in terms of the sulphur 'blocking' adsorption sites and so preventing the adorption of Mo-rich precursor species.

We can test the validity that this simple model, originally derived for bimolecular reactions, can explain the behaviour observed for the dependence of MoS_2 growth on sulphur evaporation temperature by converting the sulphur evaporation temperature to a sulphur partial pressure using equation 5.6.

$$log(p) = 16.83213 - 0.0062238(T) - 5405.1/T, (393\ \text{K} \leq T \leq 598\ \text{K}). \tag{5.6}$$

where p is the sulphur partial pressure in Pa and T is the temperature in K. This relation has been derived from experimental data by Peng and co-workers [17]. Using MoS_2 coverage at a given, fixed growth time of 20 min as a proxy for the rate of MoS_2 formation, we would then expect a linear relationship between MoS_2 coverage and the inverse of the sulphur partial pressure. Such data are presented in Figure 5.11 for the three substrate growth temperatures explored, along with a linear fit to each set of data. It can clearly be seen that the agreement with Langmuir-Hinshelwood model is excellent for substrate temperatures of 550 °C and 650 °C. There is less good agreement between the model and the data for a substrate temperature of 700 °C during growth, which can be understood through examination of the surface coverages of MoS_2 observed under these conditions, which saturate at around 90%. It therefore may be more appropriate to omit the last data point in the linear fit.

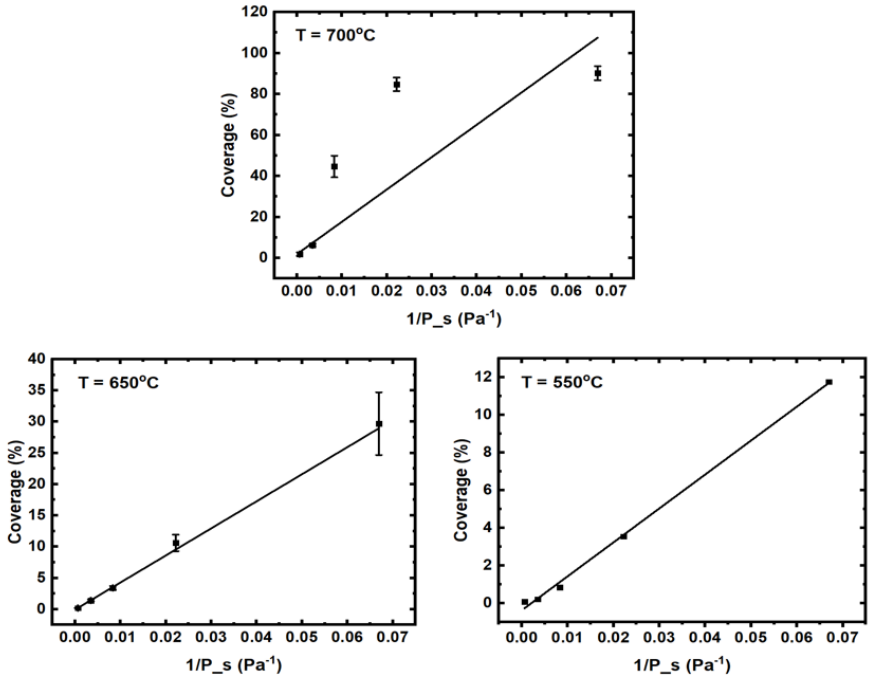

Figure 5.14: *MoS_2 coverage plotted as a function of the inverse of the sulphur vapour pressure for samples grown at various substrate temperatures.*

5.3.3 XPS Analysis

X-ray photoelectron spectra were obtained from at least three separate locations on each of the MoS_2 samples grown at differing sulphur vapour pressure. Survey spectra from as-grown MoS_2 films on silicon wafers with native oxide show a number of distinct peaks associated with silicon, molybdenum, sulphur, oxygen and carbon, Figure 5.15. The presence of the latter two elements is common in core-level spectra obtained from samples which have been exposed to ambient atmosphere prior to measurement and arise primarily from the adsorption of contaminants, such peaks often being referred to as 'adventitious' in the literature.

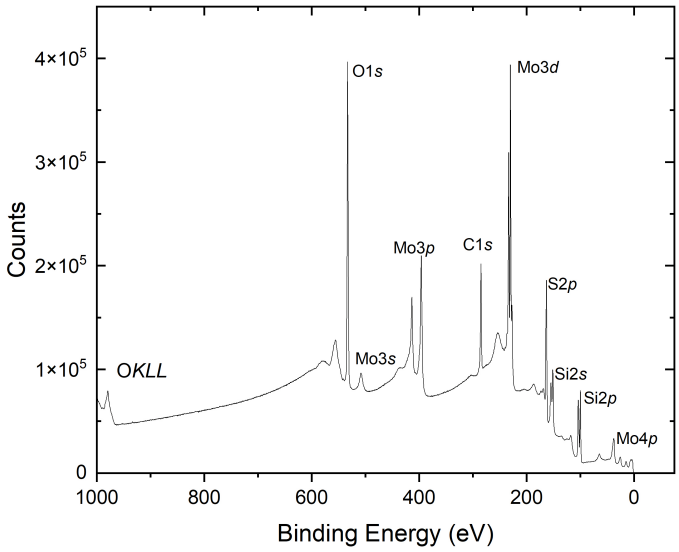

Figure 5.15: *A typical XPS survey spectrum from MoS_2 grown on natively oxidised silicon.*

A consistent energy reference is important in determining the precise binding energy of core-level photoelectron peaks, particularly as their position may be influenced by their local chemical environment, leading to a 'chemical shift', as discussed in Chapter 2. These subtle changes in binding energy provide extremely valuable insight in the chemical, as opposed to merely elemental, structure of the material under investigation. For the data presented here energies were referenced to the Si $2p_{3/2}$ core level, with binding energy taken as 99.50 eV, which is the modal value from twenty references in the U.S. National Institutes of Standards and Technology XPS database [18] (the average value of binding energies, 99.53 eV agrees with the modal value to within the binding energy error in our measurements). The exact position of the Si $2p$ lines was obtained by fitting a doublet peak

consisting of the convolution of Gaussian-Lorenztian lineshapes combined with an inelastic electron background calculated by the method of Shirley [19].

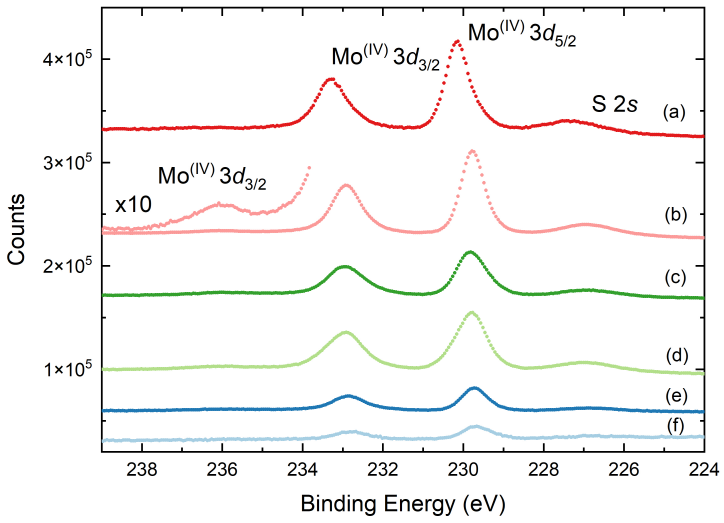

Figure 5.16: *High-resolution XPS spectra obtained from the region of the Mo3d core line in (a) bulk MoS_2 and MoS_2 grown on silicon at (b) 140 °C; (c) 160 °C; (d) 180 °C; (e) 200 °C and (f) 250 °C.*

High-resolution X-ray photoelectron spectra obtained for binding energies between 220 and 240 eV, Figure 5.16, display four distinct peaks which can be assigned as follows [20, 21, 22, 23]: a singlet peak at 227.40 ± 0.05 eV originating from the $2s$ core level of sulphur in MoS_2; a doublet peak at 230.31 ± 0.05 and 233.37 ± 0.05 eV corresponding to the $3d_{5/2}$ and $3d_{3/2}$ core states of Mo in the 4+ oxidation state appropriate for MoS_2 and the Mo $3d_{3/2}$ state of Mo in the 6+ oxidation state of MoO_3 located at a binding energy of 236.69 ± 0.05 eV. The Mo $3d_{5/2}$ line of MoO_3 overlaps with the Mo $3d_{3/2}$ peak of Mo^{4+} and is hence not resolved. Detailed spectra for binding energies between 160 and 174 eV are shown in Figure 5.17 and show a clear doublet due to the S $2p_{1/2}$ and $2p_{3/2}$ lines. As the sulphur evaporation temperature increases to 250°C, the coverage of MoS_2 declines, as shown in Figure 5.9, and as a result the bulk plasmon loss of the Si $2s$ line, Figure 5.18, becomes more prominent.

To obtain more detailed information regarding the chemical state of the AP-CVD grown MoS_2 films spectra were initially fitted with two doublet peaks (with area ratios of 2:3 determined by their multiplicity, $(2J + 1)$) associated with the Mo $3d$ levels in MoS_2 and MoO_3 and a singlet peak corresponding to the sulphur 2 s core level. All peak envelopes

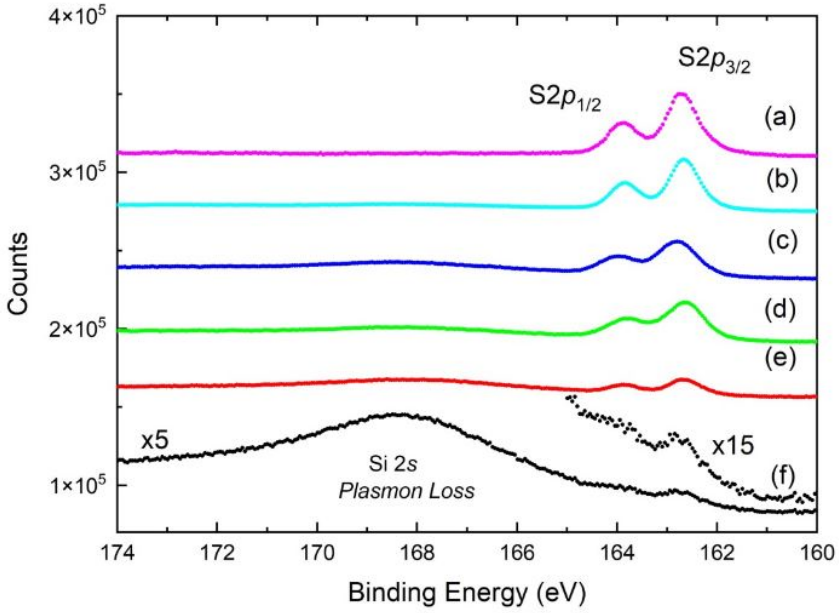

Figure 5.17: *High-resolution XPS spectra obtained from the region of the S 2p core line in (a) bulk MoS_2 and MoS_2 grown on silicon at (b) 140 °C; (c) 160 °C; (d) 180 °C; (e) 200 °C and (f) 250 °C. As the coverage of MoS_2 on the silicon substrate decreases the plasmon loss of the Si 2s line becomes prominent.*

consisted of Gaussian-Lorentzian convolutions and a Shirley background was used. Fitting was carried out using Unifit [24] with the reduced χ^2 statistic and distribution of fit residuals used to determine the goodness of fit. However, despite the fit comparing well with many of those found in the literature, it is clear from Figure 5.19 this combination of peaks was unable to provide a satisfactory fit to the spectrum, with reduced χ^2 for such fits typically above 6 and clear structure visible in fit residuals. Moreover, the ratio of the areas in each peak of the doublet associated with MoS_2 was 0.71 rather than being closer to the ratio of 2:3 expected from their multiplicity.

In order to obtain more a realistic fit to the data an additional, unresolved Mo 3*d* doublet peak, located at a binding energy -0.57 ± 0.05 eV below that of MoS_2 is required. Inclusion of this extra doublet produces fits with reduced χ^2 values typically around 1 and residuals that are free from obvious structure, as shown in Figure 5.20. It is clear that the full width at half maxima of the Mo 3*d* components associated with MoS_2 and the low binding energy component are relatively narrow, indicating a good degree of crystalline order and that the doublet associated with the oxide is broad, which suggests that the MoO_3 is either amorphous or highly disordered. It should be noted that in several publications the MoO_3 3*d* level is fitted only with a singlet, rather than a doublet peak (e.g., Ref. [**?**]), which is unphysical, or this region is omitted from spectra altogether [25].

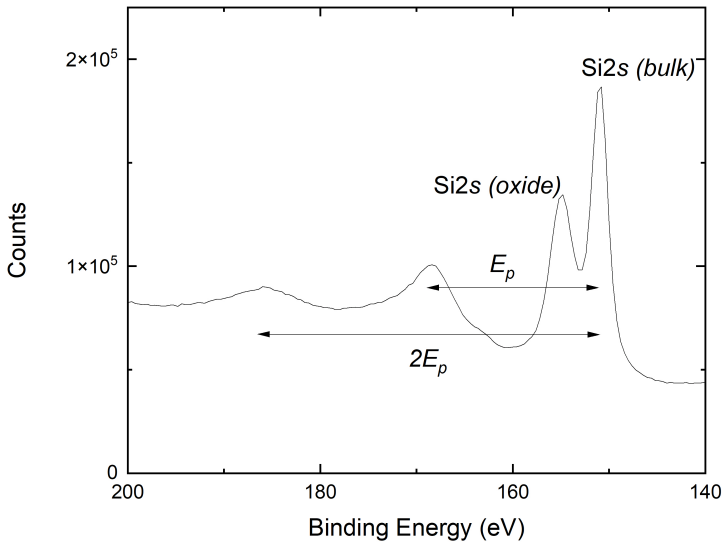

Figure 5.18: *High-resolution XPS spectrum from a natively oxidised silicon substrate showing bulk plasmon losses to the Si 2 s line at energies E_p and $2E_p$. The former becomes prominent in the S 2p spectra shown in Figure 5.17 with decreasing MoS_2 coverage.*

In Figure 5.21 the composition of the as-grown MoS_2 is determined by comparing the areas of the sulphur photoelectron lines and the Mo 3*d* lines associated with MoS_2 combined with the low binding energy component, weighted by the appropriate cross-sections, as discussed in Chapter 2. The results of using the S 2*s* lines, which are shown in Figure 5.16, are presented as red dots and the composition determined by using the S 2*p* lines, Figure 5.17, are presented as black dots. It is clear that under all growth conditions the composition remains constant to within experimental uncertainty, with a sulphur:molybdenum ratio of $\approx$ 2, as would be expected in a material which was at, or close to, stoichiometric. The composition of the commercially sourced bulk MoS_2 is also in agreement to within experimental error, further supporting the assertion that the MoS_2 produced by AP-CVD is stoichiometric within measurement uncertainty. However, while the composition remains approximately constant with respect to growth conditions it can be seen that the intensity of the low binding energy Mo 3*d* doublet decreases significantly in area relative to the main MoS_2 peak as a function of sulphur partial pressure, Figure 5.22 indicating that the species responsible has a concentration which is dependent on growth conditions.

A low energy component to the Mo 3*d* XPS core lines has been observed in several studies of bulk and few-layer/monolayer MoS_2 and a variety of explanations for its origin

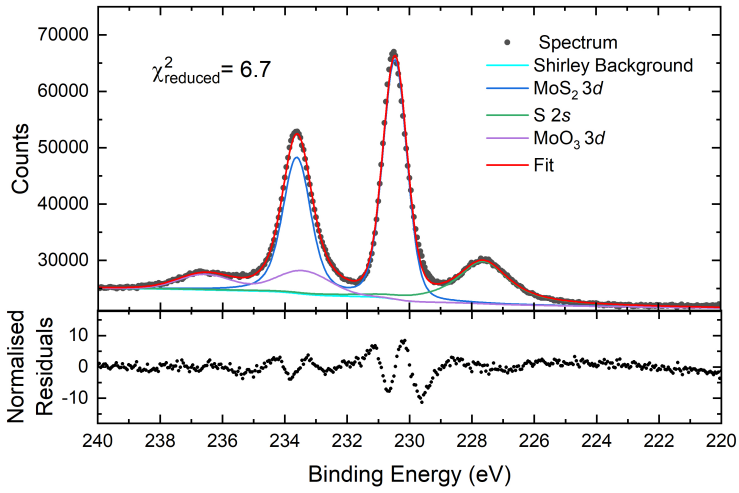

Figure 5.19: *Fit to the Mo 3d and S 2s core levels of as-grown MoS_2 films using two components for Mo, corresponding to MoS_2 and MoO_3. Note that $\chi^2 >> 1$ and there is clear structure in the fit residuals.*

have been advanced, which we now consider. On the basis of an XPS study of ion irradiation of bulk MoS_2, Lince *et al.* [20] suggested that preferential sputtering of S gave rise to metallic Mo islands at a density too small to give rise to detectable $Mo^{(0)}$ 3*d* peaks in the XP spectra, but which were large enough to create band bending at the MoS_2 surface and a commensurate shift in the Mo 3*d* and S 2*p* lines of the bulk material. Such local doping from the presence of metallic Mo is, however, extremely unlikely for the samples grown in this study, which were transported through air from the ambient pressure growth system to the XP spectrometer as we would expect complete oxidation of Mo metal to have occurred during such exposure, which would have the likely outcome of eliminating any MoS_2 band bending.

Several low-binding energy components to both Mo 3*d* and S 2*p* spectra were observed in a high resolution core-level study using synchrotron radiation by Mattila *et al.* [26]. Natural samples of MoS_2 were cleaved either by scraping with a blade or peeling off a layer of Al glued to the surface of the sample under ultra-high vacuum conditions. The latter approach was stated to produce a smoother surface containing fewer steps, an assertion supported by low energy electron diffraction (LEED) measurements. Core-level spectra from the 'smoother' samples were observed to contain a single spin-orbit split doublet for each of the S 2*p* and Mo 3*d* core levels. In contrast S 2*p* spectra from the stepped samples displayed two extra components at relative binding energies of −0.31 and

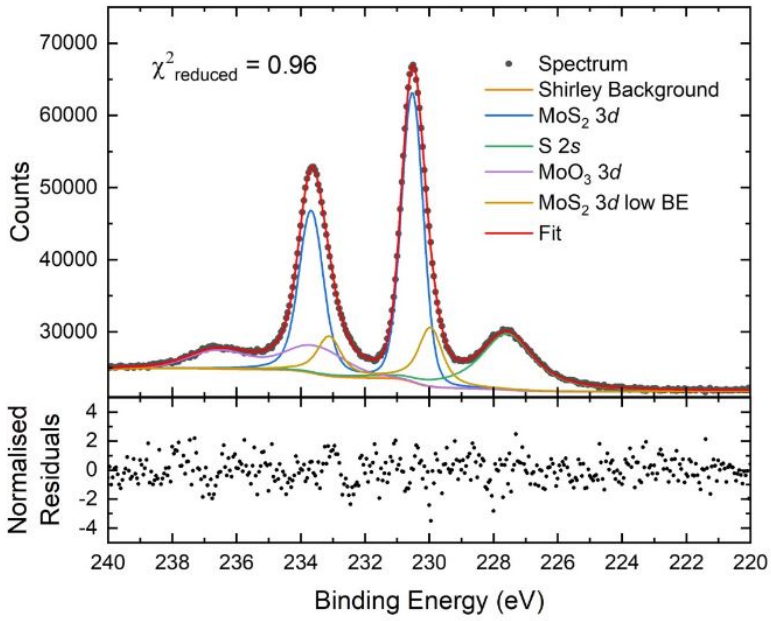

Figure 5.20: *Fit to the Mo3d and S2s core levels of as-grown MoS_2 films using three components for Mo, corresponding to MoS_2, MoS_x and MoO_3. Note that $\chi^2 \approx 1$ and there is no structure to the fit residuals.*

−0.58 eV and the Mo 3*d* three extra low binding energy components at −0.2, −0.4 and −0.6 eV. The presence of the low binding energy peaks was attributed to photoemission from low co-ordination sites at step/terraces formed during scraping, the variation of the intensity of the components with photon energy ruling out their origin from surface core level shifts, such as those seen at the surface of graphite [27]. The lower energy resolution inherent in the laboratory-based XPS measurements presented here does would not allow the distinction between low binding energy components observed by Mattila and co-workers and, in principle, the spectra measured from the AP-CVD grown MoS_2 is therefore consistent with their observations. However, it is straightforward to rule out island edges as the origin of the low-binding energy components to the S 2*p* and Mo 3*d* spectra in this study on the basis of the SEM images of the samples presented earlier, Figure 5.9: Increasing sulphur partial pressure decreases the size of the AP-CVD grown MoS_2 islands, thus *increasing* the ratio of edge to 'bulk' while at the same time the relative intensity of the low binding energy components of the S 2*p* and Mo 3*d* is observed to *decrease*.

An alternative explanation for the presence of the lower binding energy component to the Mo 3*d* XPS peaks is that this component may originate from sub-stoichiometric regions of the MoS_2 overlayer. Such vacancies can lead to a shift in both core and valence states due to pinning of the Fermi level to the top of the MoS_2 valence band. In another

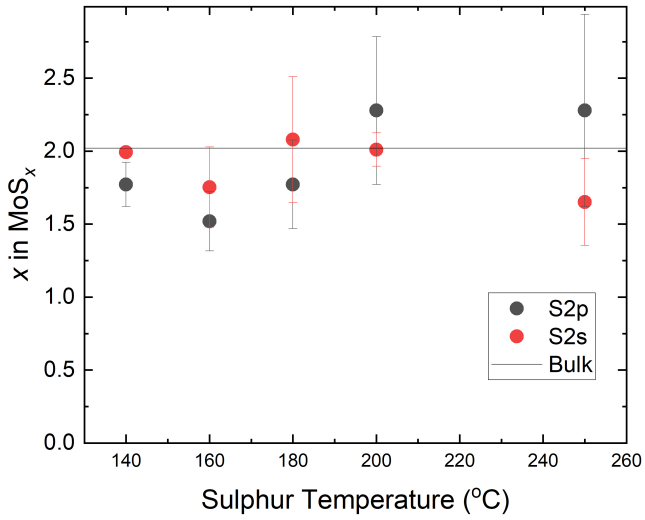

Figure 5.21: *Ratio of S to Mo, x in MoS_x, as a function of sulphur evaporation temperature determined from the ratio of the area of the S2p core levels (black circles) and S2s core levels (red circles) to the Mo3d levels associated with MoS_2 (including the 'low binding energy component'). Appropriate weighting factors for cross-section are applied. The black line is the value for this ratio obtained from a commercially purchased bulk MoS_2 sample.*

XPS study of ion irradiation of bulk MoS_2 Baker *et al.* [23] observed a continuous decrease in Mo $3d_{5/2}$ binding energy as a function of ion dose and hence, due to the preferential sputtering of sulphur, reduction in stoichiometry. On the basis of their analysis they proposed a relationship linking the difference in Mo $3d_{5/2}$ and S $2p_{1/2}$ binding energies and overall stoichiometry. On the basis of their analysis, the low binding energy component of the Mo $3d_{5/2}$ lines obtained from the CVD grown MoS_2 presented here, at a position 0.57 eV lower in binding energy than the main MoS_2 peaks, is indicative of a stoichiometry MoS_x where $x = 1.9$. Examination of the XPS data from our samples demonstrates that the maximum ratio between the areas of the main Mo $3d$ lines and the low binding energy component, which occurs at a growth temperature of 140°C, is approximately 0.2 which results in a global stoichiometry of MoS_x where $x = 1.98$. This interpretation is fully consistent with the results presented in Figure 5.21 since deviations from bulk stoichiometry of the order of 1% would be below the noise level associated with these experiments and is, indeed at or below the limit of precision in stoichiometry typically achieved in XPS measurements. In a later XPS study of the irradiation of MoS_2 McIntyre and co-workers [28] observed a valence band shift of -0.55 eV, remarkably close to the difference in position of the low binding energy component of the MoS_2 Mo $3d$ line of -0.58 eV, which they attributed to Fermi level pinning due to the presence of

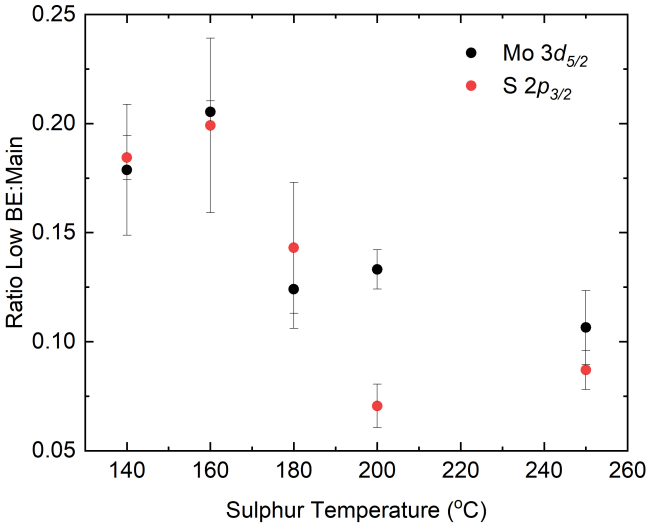

Figure 5.22: *Ratio of the areas of the low $Mo3d_{5/2}$ peaks at low binding energy to that of the main peak associated with MoS_2. The decrease in this ratio with sulphur temperature during growth is clear.*

unspecified 'defects'. Given that preferential sputtering of sulphur is usually observed as the result of irradiation of MoS_2, it is reasonable to draw the conclusion that such defects are associated with sulphur loss and that the low binding energy component of the Mo 3*d* line arises due to a small degree of sub-stoichiometry in the AP-CVD grown MoS_2.

A final possibility is that the low binding energy Mo 3*d* and S 2*p* components arise as a result of either adsorption of ambient species or sample oxidation due to unavoidable exposure to the ambient as the samples are transported from the growth laboratory for XPS analysis. As an example of the former, Kim *et al.* observed a reversible downward shift of the binding energy of the Mo 3*d* and S 2*p* lines coupled with a reduction in work function for both 2 and 12 layer MoS_2 films due to the presence of adsorbed ambient species [25]. It is less obvious how oxidation could play a role, as the binding energy of oxidised species should be greater than those associated with MoS_2. XPS studies of molybdenum oxysulphides, MoO_xS_y present an Mo 3*d* core level component in addition to that associated with Mo^{4+} and Mo^{6+} at a *higher* rather than lower binding energy than that for Mo^{4+} and associated with Mo in a formal oxidation state of 5+ [22]. However, even if adsorption or oxidation plays a yet to be determined role in the formation of the low binding energy Mo 3*d* and S 2*p* features, its intensity variation does not follow the age of the samples at the point of measurement. Likewise there is no correlation with the intensity of the MoO_3 related Mo3*d* peak, Figure 5.23. In contrast, there is a strong correlation

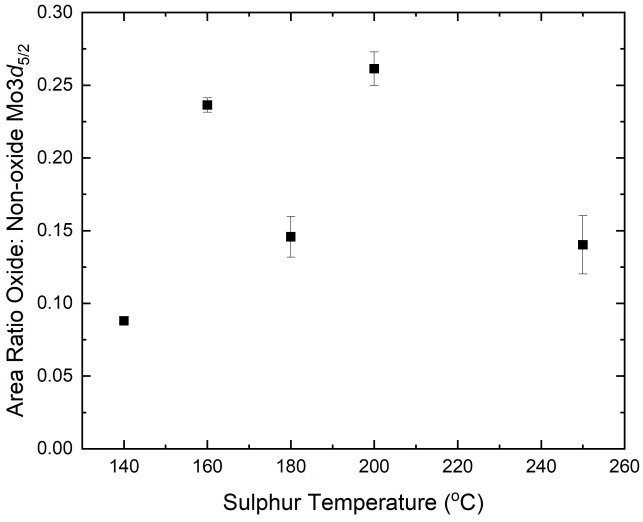

Figure 5.23: *Ratio of the area of the $Mo3d_{5/2}$ line associated with a Mo^{6+} oxidation state (MoO_3) and the areas of the $Mo3d_{5/2}$ lines associated with sulphurised Mo. It can clearly be seen that there is no relationship between sulphur temperature during growth and oxide concentration.*

with sulphur partial pressure during growth, indicating that even if adsorption or oxidation plays a role, that the formation of the species associated with this component is dependent on the conditions of film growth.

The decrease in the relative area of the low binding energy Mo $3d$ component in the core level spectra is therefore consistent with the hypothesis that an increased partial pressure of sulphur should lead to a decrease in sub-stoichiometry within the CVD grown films. In addition to doping, the presence of sulphur vacancies may play a critical role in stability and reactivity of MoS_2 monolayer and few-layer films. It has generally been established that the presence of defects correlates with the reactivity and catalytic activity of MoS_2 and that monolayer and few-layer films are not stable against ambient atmosphere in the long term. These results suggest that if correct fitting of the XP spectra from MoS_2 films is performed the presence of substoichiometry can be detected with a high level of sensitivity and hence provide insight into resulting electronic properties and chemical stability.

5.4 Conclusion

Chemical vapour deposition of MoS_2 from MoO_3 and sulphur precursors has already been demonstrated as an efficient and low-cost method for growing monolayer and few-layer MoS_2 films. Scanning electron microscopy (SEM) and Raman spectroscopy demonstrate the importance of the control and timing of evaporation of the precursor materials: if MoO_3 is allowed to deposit on the substrate before a sufficient sulphur flux is available, crystals of $MoO_{3-X}S_Y$ grow on the surface, which are not converted to MoS_2 by post-deposition reaction. These molybdenum oxides are absent when sufficient sulphur is available at growth initiation. Sample temperature also has a substantial impact on island morphology reflecting disorder associated with reduced diffusion rates during lower temperature growth. The reaction is inhibited by a high precursor concentration of sulphur on the substrate surface, which blocks the adsorbed site of Mo. A model based on Langmuir-Hinshelwood growth kinetics is demonstrated to be able to successfully to explain this phenomenon.

Core level spectroscopy indicates that the sulphur partial pressure does not lead to significant changes in the stoichiometry of the MoS_2 layers, nor is there any observable correlation with the concentration of MoO_3 relative to that of MoS_2. However, a low binding energy component is observed in both S $2p$ and Mo $3d$ spectra, which decreases with increasing sulphur partial pressure during growth. The low binding energy components of these lines are likely to originate either from defects such as sulphur vacancies [23, 28] although doping [20], possibly due to adsorption of ambient atmosphere [25] cannot be completely ruled out.

The existence site blocking at high sulphur partial pressures, leading to incomplete MoS_2 coverage, but lower defect densities leads to a conundrum in AP-CVD growth under the conditions reported in this work, as it would seem that it is possible to have either a high coverage or low defect density, but not both simultaneously as is required if monolayer and few-layer MoS_2 is to play a role in future device electronics. Further detailed investigation of AP-CVD based MoS_2 growth is therefore required in order to meet these conflicting needs.

References

[1] Kostya S Novoselov, D Jiang, F Schedin, TJ Booth, VV Khotkevich, SV Morozov, and Andre K Geim. Two-dimensional atomic crystals. *Proceedings of the National Academy of Sciences*, 102(30):10451–10453, 2005.

[2] Kin Fai Mak, Changgu Lee, James Hone, Jie Shan, and Tony F Heinz. Atomically thin MoS_2: a new direct-gap semiconductor. *Physical Review Letters*, 105(13):136805, 2010.

[3] Branimir Radisavljevic, Michael Brian Whitwick, and Andras Kis. Integrated circuits and logic operations based on single-layer MoS_2. *ACS Nano*, 5(12):9934–9938, 2011.

[4] Jonathan N Coleman, Mustafa Lotya, Arlene O'Neill, Shane D Bergin, Paul J King, Umar Khan, Karen Young, Alexandre Gaucher, Sukanta De, Ronan J Smith, et al. Two-dimensional nanosheets produced by liquid exfoliation of layered materials. *Science*, 331(6017):568–571, 2011.

[5] Keng-Ku Liu, Wenjing Zhang, Yi-Hsien Lee, Yu-Chuan Lin, Mu-Tung Chang, Ching-Yuan Su, Chia-Seng Chang, Hai Li, Yumeng Shi, Hua Zhang, et al. Growth of large-area and highly crystalline MoS_2 thin layers on insulating substrates. *Nano Letters*, 12(3):1538–1544, 2012.

[6] Yongjie Zhan, Zheng Liu, Sina Najmaei, Pulickel M Ajayan, and Jun Lou. Large-area vapor-phase growth and characterization of MoS_2 atomic layers on a SiO_2 substrate. *Small*, 8(7):966–971, 2012.

[7] Yu-Chuan Lin, Wenjing Zhang, Jing-Kai Huang, Keng-Ku Liu, Yi-Hsien Lee, Chi-Te Liang, Chih-Wei Chu, and Lain-Jong Li. Wafer-scale mos_2 thin layers prepared by MoO_3 sulfurization. *Nanoscale*, 4(20):6637–6641, 2012.

[8] Sivacarendran Balendhran, Jian Zhen Ou, Madhu Bhaskaran, Sharath Sriram, Samuel Ippolito, Zoran Vasic, Eugene Kats, Suresh Bhargava, Serge Zhuiykov, and Kourosh Kalantar-Zadeh. Atomically thin layers of MoS_2 via a two step thermal evaporation–exfoliation method. *Nanoscale*, 4(2):461–466, 2012.

[9] Yi-Hsien Lee, Xin-Quan Zhang, Wenjing Zhang, Mu-Tung Chang, Cheng-Te Lin, Kai-Di Chang, Ya-Chu Yu, Jacob Tse-Wei Wang, Chia-Seng Chang, Lain-Jong Li, et al. Synthesis of large-area MoS_2 atomic layers with chemical vapor deposition. *Advanced Materials*, 24(17):2320–2325, 2012.

[10] Sina Najmaei, Zheng Liu, Wu Zhou, Xiaolong Zou, Gang Shi, Sidong Lei, Boris I Yakobson, Juan-Carlos Idrobo, Pulickel M Ajayan, and Jun Lou. Vapour phase growth and grain boundary structure of molybdenum disulphide atomic layers. *Nature Materials*, 12(8):754–759, 2013.

[11] Gang Hee Han, Nicholas J Kybert, Carl H Naylor, Bum Su Lee, Jinglei Ping, Joo Hee Park, Jisoo Kang, Si Young Lee, Young Hee Lee, Ritesh Agarwal, et al. Seeded growth of highly crystalline molybdenum disulphide monolayers at controlled locations. *Nature Communications*, 6:6128, 2015.

[12] Dancheng Zhu, Haibo Shu, Feng Jiang, Danhui Lv, Vijayshankar Asokan, Omar Omar, Jun Yuan, Ze Zhang, and Chuanhong Jin. Capture the growth kinetics of CVD growth of two-dimensional MoS_2. *npj 2D Materials and Applications*, 1(1):1–8, 2017.

[13] Qingqing Ji, Yu Zhang, Yanfeng Zhang, and Zhongfan Liu. Chemical vapour deposition of group-VIB metal dichalcogenide monolayers: engineered substrates from amorphous to single crystalline. *Chemical Society Reviews*, 44(9):2587–2602, 2015.

[14] Shanshan Wang, Merce Pacios, Harish Bhaskaran, and Jamie H Warner. Substrate control for large area continuous films of monolayer MoS_2 by atmospheric pressure chemical vapor deposition. *Nanotechnology*, 27(8):085604, 2016.

[15] Changgu Lee, Qunyang Li, William Kalb, Xin-Zhou Liu, Helmuth Berger, Robert W Carpick, and James Hone. Frictional characteristics of atomically thin sheets. *Science*, 328(5974):76–80, 2010.

[16] Kibum Kang, Saien Xie, Lujie Huang, Yimo Han, Pinshane Y Huang, Kin Fai Mak, Cheol-Joo Kim, David Muller, and Jiwoong Park. High-mobility three-atom-thick semiconducting films with wafer-scale homogeneity. *Nature*, 520(7549):656–660, 2015.

[17] Ding-Yu Peng and Jianjun Zhao. Representation of the vapour pressures of sulfur. *The Journal of Chemical Thermodynamics*, 33(9):1121–1131, 2001.

[18] https://srdata.nist.gov/xps/main_search_menu.aspx, 07/02/2022.

[19] Dave A Shirley. High-resolution X-ray photoemission spectrum of the valence bands of gold. *Physical Review B*, 5(12):4709, 1972.

[20] Jeffrey R. Lince, D.J. Carre, and P.D. Fleischauer. Effects of Argon Ion Bombardment on the Basal Plane Surface of MoS_2. *Langmuir*, 2:805–808, 1986.

[21] N. M. D. Brown, N. Cui, and A. McKinley. An XPS study of the surface modification of natural MoS_2 following treatment in an RF-oxygen plasma. *Applied Surface Science*, 134:11–21, 1998.

[22] L. Benoist, D. Gonbeau, G. Pfister-Guillouzo, E. Schmidt, G. Meunier, and A. Levasseur. X-ray photoelectron spectroscopy characterization of amorphous molybdenum oxysulfide thin films. *Thin Solid Films*, 258:110–114, 1995.

[23] M. A. Baker, R. Gilmore, C. Lenardi, and W. Gissler. XPS investigation of preferential sputtering of S from MoS_2 and determination of MoS_x stoichiometry from Mo and S peak positions. *Applied Surface Science*, 150:255–262, 1999.

[24] R. Hesse, T. Chassé, and R. Szargan. Unifit 2002—universal analysis software for photoelectron spectra. *Analytical and Bioanalytical Chemistry*, 375(7):856–863, 2003.

[25] Jong Hun Kim, Jinhwan Lee, Jae Hyeon Kim, C. C. Hwang, Changgu Lee, and Jeong Young Park. Work function variation of MoS_2 atomic layers grown with chemical vapor deposition: The effects of thickness and the adsorption of water/oxygen molecules. *Applied Physics Letters*, 106(25), 2015.

[26] S. Mattila, J. A. Leiro, M. Heinonen, and T. Laiho. Core level spectroscopy of MoS_2. *Surface Science*, 600(24):5168–5175, 2006.

[27] Michael R. C. Hunt. Surface and bulk components in angle-resolved core-level photoemission spectroscopy of graphite. *Physical Review B*, 78(15), 2008.

[28] N. S. McIntyre, P. A. Spevack, G. Beamson, and D. Briggs. Effects of argon ion bombardment on basal plane and polycrystalline MoS_2. *Surface Science Letters*, 237:L390–L397, 1990.

Chapter 6

Growth of monolayer and few layer MoS_2 on graphene and graphite

This chapter discusses preliminary experiments performed to explore the growth of MoS_2 on graphene and graphite via hot-wall atmospheric-pressure chemical vapour deposition (AP-CVD). Samples produced by this method were studied with Raman spectroscopy to determine the uniformity and number of MoS_2 layers grown on the substrate and Scanning Electron Microscopy (SEM) to determine the morphology of the MoS_2 films.

6.1 Introduction

As discussed in detail in Chapter 1, the combination of graphene and other two-dimensional layered materials into artificial heterostructures can create new materials which exhibit desirable functionality [1]. Indeed, the efficiency of devices can be improved by adding graphene layer to a 2D semiconductor heterostructure assembly [2]. Layered MoS_2 is a 2D nanomaterial which, in monolayer form, has a direct bandgap while the bulk is an indirect gap semiconductor [3, 4]. The direct gap makes this material highly attractive for opto-electronics applications. Van der Waals heterostructures (vdWHS) of semiconducting MX_2 and graphene therefore have great technological potential. In this Chapter, initial work on the creation of such heterostructures by the CVD growth of MoS_2 on CVD-prepared graphene, commercially available graphene powder and a 'paper' made from the commercially produced graphene is presented, along with the growth of MoS_2 on highly-oriented pyrolytic graphite (HOPG) as a model system. The results indicate some of the challenges that must be overcome if direct growth is to be used for vdWHS fabrication.

6.1.1 MoS_2/graphene

Thus far, the mechanical transfer method has been the preferred technique for preparing for preparing vdWHS [5, 6]. The mechanical transfer approach builds upon the development of micromechanical exfoliation for the preparation of two-dimensional materials and involves the painstaking assembly of exfoliated layers into a vdWHS by mechanical manipulation. Although this technique offers great control and precision over assembly (to the degree that the azimuthal orientation between layers can be controlled [7]) it is clearly not scalable to industrial production. Moreover, as a result of this approach, the properties of the prepared heterostructures can be affected by contamination which occurs during the transfer process.

Recently, methods of direct growth have been adopted to solve these problems [8, 9, 10, 11]. Ago *et al.*, for example, used chemical vapour deposition to deposit monolayer MoS_2 islands on graphene domains which were then transferred onto a SiO_2/ Si substrate from a Cu substrate [8]. Shi *et al.* in 2015 reported the growth of MoS_2 islands randomly on a graphene/Au substrate [9]. In 2012 Shi *et al.* were the first to demonstrate the direct growth of MoS_2 on an as-prepared CVD-grown graphene monolayer on a Cu foil substrate [10]. In their experiment, the MoS_2 was grown on graphene at the relatively low temperature of 400°C in a low-pressure chemical vapour deposition (LP-CVD) system, using ammonium thiomolybdate $(NH_4)_2MoS_4$ as a precursor together with an organic solvent. The organic solvent was used to carry the precursor to the growth zone via an Ar gas flow and deposition on the graphene film at room temperature was the first step. Upon annealing, the precursors then decompose and assemble to form an epitaxial MoS_2 layer on the graphene surface. Controlling the number of MoS_2 layers on the graphene surface

was a challenge. In this work, we present first attempts at a single step growth process to produce MoS_2 on graphene with controllable coverage and thickness.

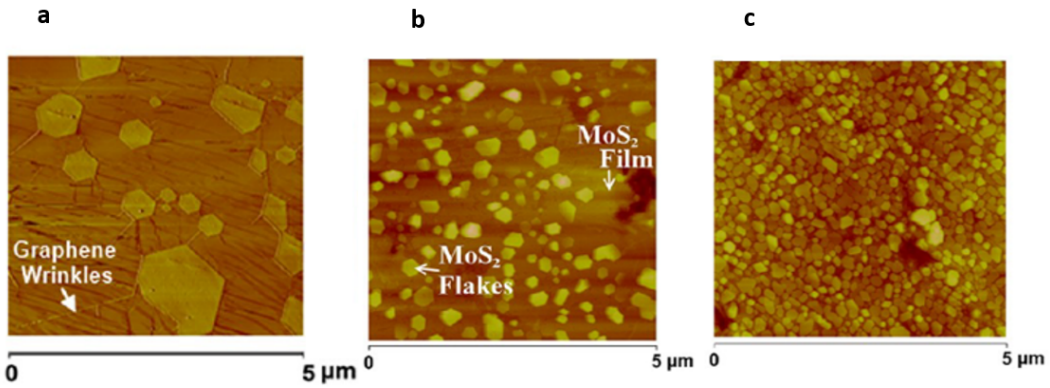

Figure 6.1: *AFM images showing MoS_2 islands on CVD grown graphene/Cu foil substrates under different growth conditions. a) AFM image showing the formation of isolated islands along graphene wrinkles at a very low precursor concentration. b) AFM images of the sample surface after MoS_2 was grown with a high concentration of precursor. Coverage of MoS_2 islands increases on the surface with the formation of a MoS_2 thin film between the flakes. c) when the amount of precursor further increases, hexagonal-shaped MoS_2 multilayer islands fully covered the MoS_2 film [10].*

Figure 6.1a shows AFM images of the resulting MoS_2 islands on graphene/Cu found by Shi *et al.* Isolated MoS_2 islands are clearly visible on the surface when a low concentration of precursor is employed. The shape of MoS_2 islands can be seen to be a hexagonal or quasi-hexagonal shape. The MoS_2 islands have a lateral size ranging from nanometers to several micrometres and are typically a few layers thick. The flakes were found to nucleate at graphene wrinkles, as can be seen Figure 6.1a. With an increased amount of precursor, thicker MoS_2 flakes can be found on the surface of graphene with thicknesses in the range of about $\sim$ 10 to $\sim$ 50 nm. As shown in Figure 6.1b, when MoS_2 islands have not fully covered the surface, the morphology between the MoS_2 flakes completely differs from the initial graphene grown on Cu; no terrace features of the graphene and Cu substrate were seen. This observation suggests the MoS_2 film has fully covered the graphene surface in that area, and the MoS_2 islands in Figure 6.1b grow on top of an underlying MoS_2 film. For the sample produced for a large concentration of precursor, MoS_2 islands fully covered the underlying MoS_2 film and are of small lateral size as seen in Figure 6.1c.

In a different approach, Ago and co-workers [8] used direct CVD growth of MoS_2 on graphene. In this case a hexagonal graphene island was transferred from the initial growth substrate to a SiO_2/Si surface (silicon wafer with a native oxide layer). In this study MoO_3 and S were employed as precursors for MoS_2 growth by CVD/vapour transport, much in

the manner employed in this thesis. The precursor materials were introduced into the growth system for 1 h under an Ar gas flow after heating the graphene to a temperature of about 900°C. As can be seen in the SEM image presented in Figure 6.2(a), a series of well-defined triangular islands of MoS_2 can be observed to have grown on the graphene flake, with a well-defined orientation, while no MoS_2 growth was found on the bare SiO_2 supporting substrate. The density of the MoS_2 islands within the interior of the graphene was found to be lower than that observed close to the graphene edges. it was suggested that this might be because the MoS_2 precursors deposit on SiO_2 first and then diffuse to the graphene edge and start to nucleate there.

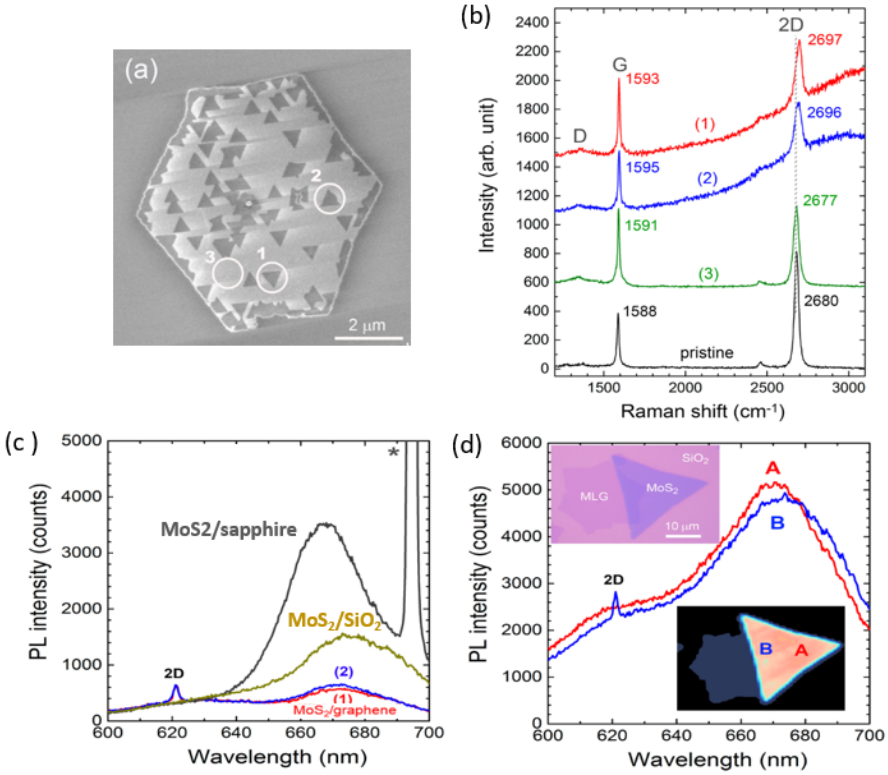

Figure 6.2: *(a) SEM image of an MoS_2/graphene heterostructure grown directly by CVD; (b) Raman spectra of pristine graphene measured before the growth of MoS_2 and spectra at the areas marked in (a) after MoS_2 growth.(c) Photoluminescence (PL) spectra of MoS_2 grown directly on graphene (red and blue) and sapphire (black), as well as that from MoS_2 transfered from sapphire to SiO_2 (brown).(d) PL spectra of a MoS_2 in a graphene heterostructure obtained by transferring MoS_2 from sapphire onto graphene/SiO_2. The upper and bottom insets show optical micrographs and PL intensity mapping, respectively. The spectra labelled A and B were taken at the places shown in the PL mapping picture. Adapted from [8].*

The interaction between MoS_2 and graphene in a MoS_2/graphene heterostructure can

also be studied by Raman spectroscopy. A Raman spectrum from the pristine graphene on SiO_2/Si before MoS_2 growth revealed strong G and $2D$ bands, with the intensity between $I_{2D}/I_G = 2$, indicating the good quality of the graphene monolayer and no significant D band present, Figure 6.2(b). However, due to the high growth temperature, there was a drop in 2D intensity on bare graphene after MoS_2 growth. Furthermore, the intensity of the $2D$ band was shown to be reduced after MoS_2 growth, with the appearance of a small intensity of the D band. As compared with the bare graphene, the region of graphene covered with MoS_2 showed upshifts in the position of both G and $2D$ bands. Other studies have shown that even mechanically stacked heterostructures of MoS_2 on graphene showed an increase in the $2D$ peak [12]. This shift in the position of the graphene Raman peaks was attributed to the interlayer coupling between MoS_2 and the graphene below.

It is known strong photoluminescence (PL) appears from MoS_2 when it is thinned to one layer [13], howevever, the PL intensity for direct heterostructure growth of MoS_2 on graphene is significantly reduced, Figure 6.2(c). A MoS_2 domain grown on sapphire was transferred to a graphene/SiO_2 substrate for comparison to direct growth Figure 6.2(d). The PL intensity was found to be strong and unaffected by the presence of graphene on the transferred heterostructure. The difference in spectra intensity at point A (overlapping region) when MoS_2 is in contact with the SiO_2 and point B when MoS_2 is in contact with the graphene is much smaller than the observed for direct MoS_2/graphene heterostructure. It was argued that this means that when the MoS_2 is grown directly on the graphene, there are stronger interactions between the layers than when they are transferred leading to a strong quenching of the PL in directly grown MoS_2 on graphene due to charge transfer (electron) from MoS_2 to graphene, which inhibits the recombination of electron-hole pairs formed by photo-excitation. Of course, it is also possible that the presence of defects in the CVD grown film could also increase coupling, leading to the same observations.

The position of the Raman modes associated with MoS_2 has also been observed to be influenced by incorporation into a vdWHS. The shift in the position of the MoS_2 Raman peak in mechanically stacked heterostructures of MoS_2/Graphene was reported by Zhou *et al.* [12], Figure 6.3. They found that the change in MoS_2 peak position was independent of the number of graphene layers under beneath. The shifts in the MoS_2 E^2_{1g} and A_{1g} Raman peak positions when incorporated into heterostructures are very similar to the shift when layer thickness increases from a MoS_2 monolayer to a few-layer MoS_2 [14]. The location of the Raman-active A_{1g} mode, in particular, in the monolayer heterostructure is very similar to that of a bare MoS_2 bilayer. They attributed the shift in MoS_2 Raman peaks in their study to the presence of van der Waals interactions between MoS_2 and graphene.

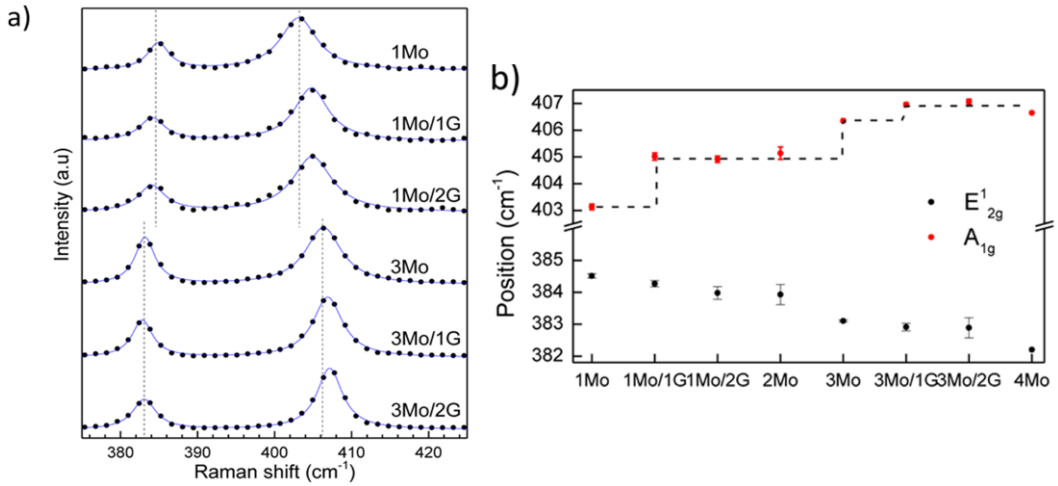

Figure 6.3: *(a) Raman spectra of MoS_2 in nMo/mG heterostructures, where n and m represent the MoS_2 and graphene layer numbers, respectively. (b) MoS_2 peak locations calculated from spectra in (a) [12].*

6.1.2 MoS_2 on graphite

As mentioned above, most heterostructure devices are made by mechanical transfer techniques and suffer from contamination caused by the transfer process as well as being inherently difficult to scale. For a clean interface, direct CVD development of heterostructures is a promising alternative, but the appropriate growth conditions need to be determined. Given the relative expense and difficulty in producing high quality graphene monolayers, an alternative approach to gain understanding of the growth of MoS_2 on graphene is to choose an appropriate model substrate. The atomic structure of the outermost layer of highly oriented pyrolytic graphite (HOPG) is identical to that of pristine graphene, hence it is perfect for studying the growth of MoS_2 on graphene and related surfaces. Moreover, HOPG is often significantly cleaner and has fewer defects than the CVD graphene surface. So, to avoid the necessity of graphene transfer, growth of heterostructures containing MoS_2 directly on graphite has been reported [15, 16, 17]. The results of these studies showed that most of the MoS_2 grown on top of graphite was in the form of highly ordered triangular islands which nucleated at graphite step edges. It was found that the MoS_2 followed the orientation of the underlying graphite substrate, which indicates that the graphite substrate is a good template for the MoS_2 growth. Pollmann *et al.* [15], for example, reported the direct growth of CVD MoS_2 on graphite. In their experiment, they used MoO_3 and S as precursors and freshly cleaved HOPG as a substrate. MoS_2 triangular nanoflakes with a 100 nm edge length were produced on the surface. The MoS_2 islands form a monolayer with a height of 0.7 nm, which is confirmed by AFM. Their study shows that the nucleation of MoS_2 on graphite is strongly influenced by graphite

substrate imperfections (graphite step height). In particular, a correlation between the MoS_2 island height and the graphite step height. A few monolayer MoS_2 'triangles' are found at the monolayer HOPG step edge, while a continuous sequence of multilayer MoS_2 islands is located at four HOPG layer step edges. Furthermore, it was found that triangular MoS_2 islands grew on the graphite upper and lower terraces, which they attributed to self-seeding nucleation, which acts as the origin of growth. A shift in MoS_2 Raman modes was observed in MoS_2 on graphite in the Pollmann *et al.* study, and it was found that the peak differences in MoS_2 on graphite were larger than those of exfoliated MoS_2 on SiO_2 [18]. This difference can be attributed to contamination and intercalated water at the interface between MoS_2 and SiO_2 induced during the exfoliation process. These impurities result in various charge transfers between MoS_2 and the SiO_2 surface, but are not present on the surface of clean graphite. The Raman shift in Pollmann *et al.* study was attributed to contributions from a few layers of MoS_2 or charge transfer from MoS_2 to graphite.

The influence of defects in the graphite surface on the growth of MoS_2 was investigated by pre-treating graphite surfaces with ion irradiation prior to MoS_2 growth to create active nucleation sites in order to promote growth on substrate terraces [19]. On ion-irradiated surfaces, it was found that MoS_2 grows not only at the graphite step, but also on the terraces. The resulting MoS_2 islands were found to be monolayer thick but did not have a perfect triangular shape, indicating a degree of disorder not observed for growth on pristine graphene surfaces. The number of MoS_2 islands grown was found to be less than the number of created defects. It was suggested that the reason for this was that some defect sites were not large enough to sustain stable nucleation or the ion-induced defect annealed when the graphite substrate was heated up during MoS_2 growth.

6.2 Growth of MoS_2 on Graphene and Graphite

6.2.1 Growth of MoS_2 on few-layer graphene (FLG)

First attempts to grow MoS_2 on graphene/Cu were undertaken using Method #1 described in Chapter 3, in which the tube with the two powders of MoO_3 and S was pushed manually after the furnace reached the target temperature, placing the sulphur boat halfway inside the furnace to ensure sufficient sulphur vapour during MoS_2 formation. It was found that when sulphur was introduced into the tube during the growth process, the hot sulphur strongly reacted with the copper substrate, leading to a dark grey solid surface. Figure 6.4 shows a photo of graphene on Cu before MoS_2 growth (a) and after MoS_2 growth (b). The change in the copper foil can be associated with the formation of CuS via the following reaction scheme:

$$\mathrm{Cu}(s) + \mathrm{S}(g) \rightarrow \mathrm{CuS}(s) \tag{6.1}$$

These results are similar to those observed by Ago *et al.* [8], in which the Cu colour was observed to changes with particles of MoS_2 flakes grown on graphene/Cu, but no heterostructure of MoS_2 on graphene/Cu was formed.

The formation of CuS led to a profound degradation of the mechanical properties of the copper foil substrate, which often crumbled to a powder. As a result of this degradation due to the reaction of copper with the sulphur, optimising the growth of MoS_2/graphene heterostructures was obviously not possible under these specific growth conditions . Hence, to try to avoid the occurrence of this kind of the reaction, it was decided to keep the sulphur boat next to the edge of the furnace rather than inside it, Method #2 described in Chapter 3.

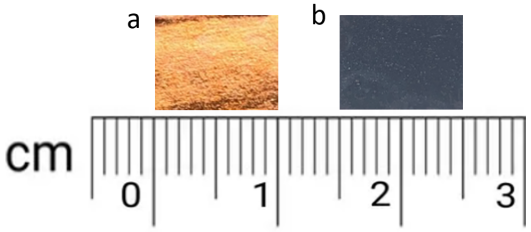

Figure 6.4: *a) An optical photograph of graphene/Cu before MoS_2 growth (a) and after CVD with MoO_3 and S (b). The colour change and degradation of mechanical properties are associated with strong sulphurisation.*

Figure 6.5 presents a photo of graphene/Cu after MoS_2 growth at 650°C and demonstrates that the Cu is less sulphurised than that shown in Figure 6.4. Figures 6.6(a-c) shows SEM images of the film grown on few layers of graphene/Cu produced by this approach. As the substrate surface is not fully covered by molybdenum oxide, terrace features of graphene and Cu substrate are easy to differentiate in the SEM micrographs. The high magnification image of the sample in Figure 6.6(b) clearly shows the presence of a submonolayer coverage of triangular islands which can be attributed to MoS_2 produced on the graphene (which fully covered the copper surface). MoS_2 islands were found nucleating at graphene wrinkles as indicated in 6.6(b) in agreement with the results of Shi *et al.* [10], suggesting that the graphene wrinkles can effectively act as the initial centre for MoS_2 nucleation. The nucleation of MoS_2 on the graphene wrinkles is possible due to the curvature created by their presence, which makes the wrinkles more reactive than planar graphene [20]. Networks of graphene wrinkles that have been observed on a number of surfaces, for example, the growth of few-layer graphene on SiC [21]. Previously these have been thought to be undesirable due to their negative influence on the transport properties of the graphene. However, their role as nucleation sites for transition metal dichalcogendides

may make them attractive for the production of heterostructures by scalable techniques, as such defects are less deleterious than grain boundaries, step edges and vacancies for example which, as discussed above, have also been observed as nucleation sites for TMDC growth.

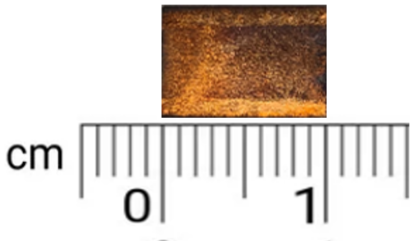

Figure 6.5: *A photo of graphene/Cu after MoS_2 growth at* 650°C *shows the Cu has less sulphurisation.*

As shown in Figure 6.6(c), increasing the substrate growth temperature to 700°C leads to a complete coverage of the surface by facetted crystals of molybdenum oxide and no contrast between the graphene and the underlying copper substrate can be observed. The Raman spectrum in Figure 6.7, obtained from the sample produced at the higher MoS_2 growth temperature, shown in Figure 6.6(c), displays a series peaks located at values close to that found in MoO_3 and MoO_2 [22], and there were no features associated with MoS_2 detectable. Raman lines associated with MoS_2 will occur at 384 cm^{-1} and 400 cm^{-1} [14] and cannot be observed above the noise. It can therefore be concluded that, although MoS_2 islands can be grown on graphene/Cu under the conditions investigated, they at best form a minority species.

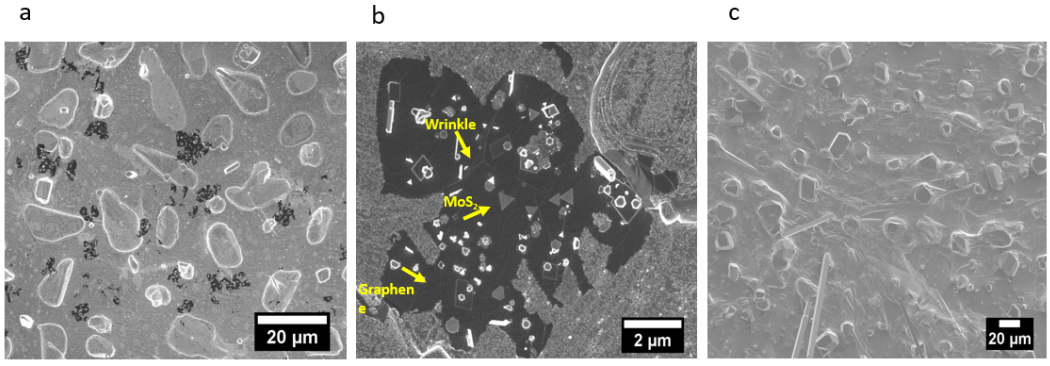

Figure 6.6: *SEM images showing films grown on CVD-produced graphene/Cu foil substrates under different growth temperatures: a,b) Isolated species which can be attributed to MoS_2 are observed at a substrate growth temperature of 650* °C*. c) An image of a sample surface after growth at a temperature of 700* °C*, the graphene surface is completely covered by an oxide layer. The growth time in both experiments was 2 h.*

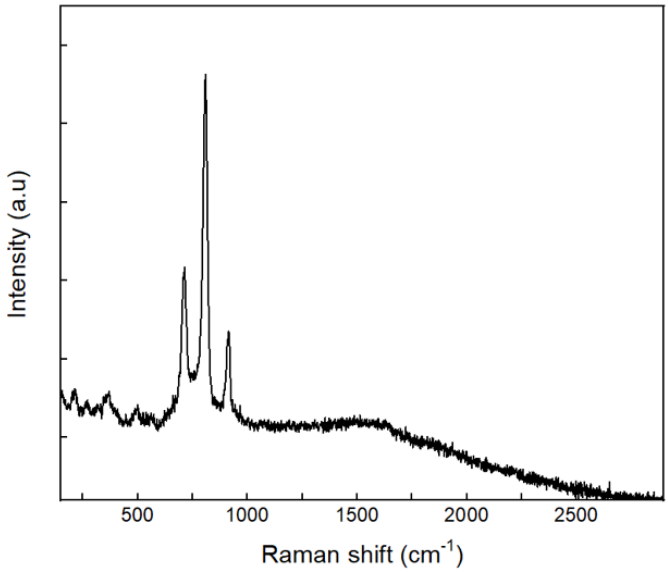

Figure 6.7: *Typical Raman spectrum for the sample shown in figure 6.6(c), which clearly indicates the dominance of Raman modes associated with MoO_3 and MoO_2.*

The dominance of MoO_3 and MoO_2 in the overlayers grown at higher sample temperature coupled with the appearance of limited coverage of MoS_2 at lower growth temperature indicated a need to reduce the growth temperature further. Hence, samples were grown at a substrate temperature of 550 °C, which are shown in the SEM images of Figures 6.8(a, b). Figure 6.8(a) shows a film produced at 550°C with a sulphur evaporation temperature of 140°C which can be seen to be similar to that shown in Figure 6.6(b); terrace features of graphene are observed where there is incomplete oxide coverage. An example of the range of island morphologies presented on the surface is circled in red. A Raman spectrum obtained from this sample is shown in Figure 6.9(a) in which lines associated with graphene and molybdenum oxides can clearly be observed. However, despite careful measurement no features associated with MoS_2 could be observed above the noise.

Figure 6.8(b) shows the morphology of a film produced at a sample temperature of 550°C with a sulphur temperature of 200°C and growth time 2 h. There is a significantly lower coverage of oxide although no readily identifiable features which can be associated with MoS_2 are seen. Correspondingly, no oxide peaks could be found in Raman spectra Figure 6.9(b) from this sample. However, neither were the characteristic Raman peaks of MoS_2 present as a result of the low coverage. These results demonstrate that a lower growth temperature preserves the structure of the copper foil substrate, preventing the reactions which cause the substantial surface roughening seen in Figure 6.4(b). However, there is clearly an insufficient (if any) coverage of MoS_2. Moreover, the topography of the graphene can make the identification of MoS_2 islands difficult, especially when the coverage

is insufficient to produce a clear and unambiguous signal in Raman spectra. It was therefore decided to use a model substrate, graphite to explore growth conditions further, whilst keeping the substrate temperature at 650°C or below. The results of such an investigation could then be used as the basis of future experiments in which a complete MoS_2 overlayer could be grown on a full monolayer of graphene supported by a copper foil.

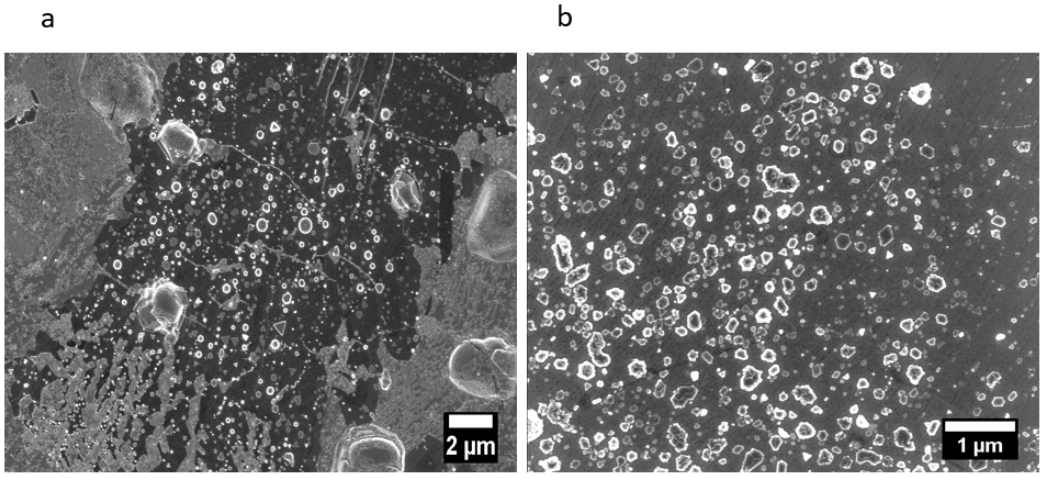

Figure 6.8: *SEM images showing film formation on CVD graphene/Cu foil substrates produced at a substrate growth temperature of 550* °C *for sulphur evaporation temperatures of (a) 140* °C *and (b) 200* °C *and a growth time of 2 h.*

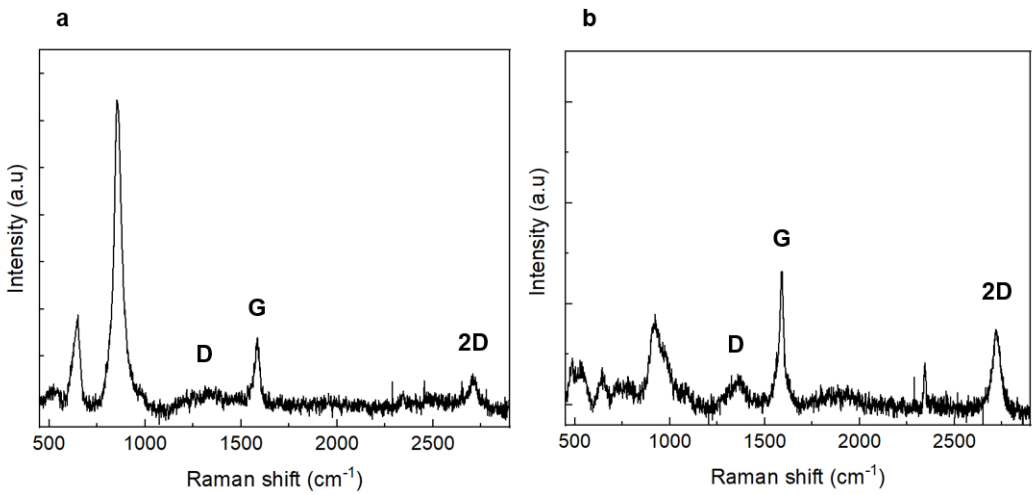

Figure 6.9: *a) Raman spectrum for the sample shown in Figure 6.8(a), which clearly shows the dominance of MoO_3 peaks on the surface, although lines due to graphene are also present. b) Raman spectrum for the samples shown in figure 6.8(b), which clearly shows a lower oxide peak intensity.*

6.2.2 Growth of MoS_2 on Highly Oriented Pyrolytic Graphite

A series of experiments were undertaken to explore the growth of MoS_2 on HOPG, the graphite being used as a model substrate in place of graphene, as described above. For each experiment the graphite samples were freshly cleaved using Scotch Magic Tape many times at room temperature until the surfaces were smooth and only surface which had not been in direct contact with the tape was exposed. Films were grown using the external heating approach, Method #2, discussed in Chapter 3, with the temperature profile shown in Figure 3.9(a).

Figure 6.10 shows SEM images of MoS_2 grown on graphite at the same substrate temperature of 650 °C but with different sulphur temperatures. MoS_2 islands can clearly be identified as dark regions on the HOPG surface. We found that reducing the sulphur temperature from 160 °C to 140 °C increased coverage, which was consistent with the observation on the growth of MoS_2 on SiO_2/Si reported in Chapter 5 in which an increase of coverage was observed with decreasing sulphur temperature, consistent with Langmuir-Hinshelwood growth kinetics.

At the lowest sulphur temperatures used, 120 °C, bright particles and needle-like micro-crystals which, due to their morphology, can be associated with MoO_3, were observed to be present at a high concentration on the graphite surface. Such incomplete sulphurisation of molybdenum oxides was also previously observed under similar growth conditions for silicon

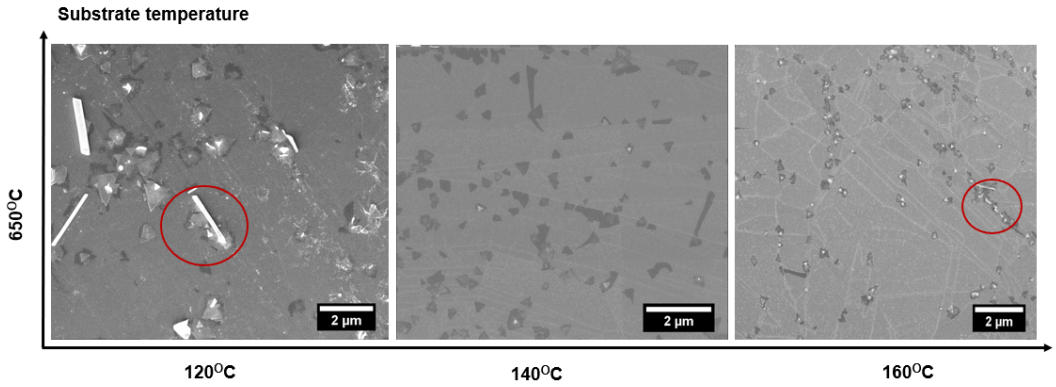

Figure 6.10: *SEM images of MoS_2 grown on HOPG at a substrate temperature of 650 °C with different sulphur temperatures. Most of the MoS_2 grown on top of graphite had a triangular shape and nucleated at the graphite step edges. Molybdenum oxide particles observed on the surface are circled in red. Growth was undertaken using Method #2 with the temperature profile describe in Figure 3.9(a).*

substrates, as reported in Chapter 5. Hence, there once more is a minimum sulphur vapour pressure below which it is not possible to completely sulphurise the molybdenum oxide precursors, which places a lower limit on the sulphur evaporation temperatures/partial pressures which are compatible with both high coverage and high MoS_2 quality.

On graphite substrates, white particles, which are likely to be $MoO_{3-X}S_Y$ are seen in the centre of most MoS_2 islands produced, as shown in the SEM images of Figure 6.10. The presence of nanoparticles in the centre of MoS_2 flakes has previously been observed in the literature [11, 23]. It has been suggested that the nanoparticles at the nucleation sites serve as a feed source for MoS_2 growth. There is agreement that the nanoparticles are formed during the early stages of growth of MoS_2, when the concentration of sulphur is low. As a result, these nanoparticles will diffuse across the surface, acting as additional nucleation sites for MoS_2 growth. In the case of the growth of MoS_2 on graphite, Pollman *et al.* found that triangular MoS_2 islands grew on the upper and lower terraces of HOPG [15], and they attributed their observation to the role of sub-oxide nanoparticles in island nucleation. These nanoparticles are mostly found in large sizes and can become trapped at the graphite step edges. Higher step edges are more likely to trap the big nanoparticles, leading to a higher concentration at those locations. It was assumed that the nanoparticles were more likely higher than the graphite edge, see Figure 6.11, allowing the growth of MoS_2 on both the upper and lower terraces.

MoS_2 was grown again using the external heating approach, Method #2, this time with the temperature profile shown in Figure 3.9(c) to determine any differences in MoS_2 film growth between the two conditions. SEM images of MoS_2 islands grown on HOPG at

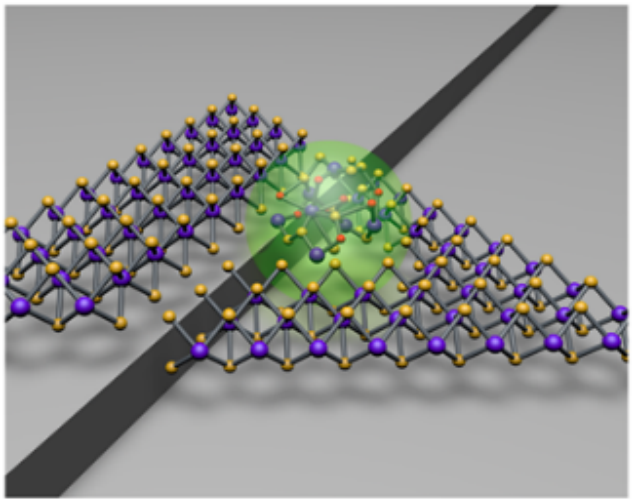

Figure 6.11: *An illustration of an HOPG substrate, sub-oxide nanoparticles, and the MoS_2 islands nucleating at a substrate step [15].*

substrate temperatures of 550 °C and 650 °C utilising a sulphur temperature of 140 °C are shown in Figure 6.12 (a) and (b), respectively. Large MoS_2 islands can be seen to nucleate at the higher growth temperature, probably across step edges – as a result of the limited height resolution possible within the SEM not all steps/step bunches are visible, but MoS_2 island nucleation is observed at all those which can be made out. At the lower growth temperature, MoS_2 island sizes are observed to be smaller, with nucleation once again appearing to occur at step edges and, possibly, grain boundaries. The MoS_2 coverage calculated for the sample in Figure 6.12 (a) was found to be 5.3 ± 0.7 %.

Comparing the SEM images presented in Figures 6.10 and 6.12 it can be seen that MoS_2 layers grown on graphite using Method #2 with the temperature profile given in Figure 3.9(c) contains fewer molybdenum oxide $MoO_{3-X}S_Y$ particles than = samples grown using the temperature profile of Figure 3.9(a). It was found that if MoO_3 is allowed to deposit on the substrate before a sufficient sulphur flux is available, crystals of $MoO_{3-X}S_Y$ grow on the surface. These crystals do not appear capable of evolving into MoS_2 via a post-deposition sulphurisation reaction under the range of growth conditions used in this study, the same observation as that for MoS_2 growth on Si when using the Method #2 with the temperature profile of Figure 3.9(a).

Although there appears to be little difference in terms of the presence or otherwise of $MoO_{3-X}S_Y$ with growth conditions for silicon and graphite substrates there is a clear dissimilarity between in MoS_2 island coverage between the two substrates, with the coverage of MoS_2 on graphite being much less than that of MoS_2 on silicon. There are a number of possibilities for this difference in island growth rate. For example, this might be a reflection of the morphology of the substrates. The amoprhous SiO_2 surface of the natively oxidised silicon wafers is very flat, smooth, and free of steps, which allows deposited precursors to readily diffuse to find critical nuclei, as seen in Chapter 5. While the cleaved graphite surface has a high step density with many step bunches visible even in SEM, which may hinder diffusion. Indeed, this may explain the smaller island sizes observed on HOPG.

An alternative explanation could be that the interaction between adsorbed precursors and the substrate is larger in the case of oxidised silicon than for graphite, in which case the residence time of the adsorbates will be significantly lower in the latter case, making desorption before meeting critical nuclei more likely and so reducing coverage. Theoretical studies, such as first-principles Density Functional Theory (DFT) calculations of the precursor-substrate binding energy, may be able to shed light on the likelihood of this latter hypothesis.

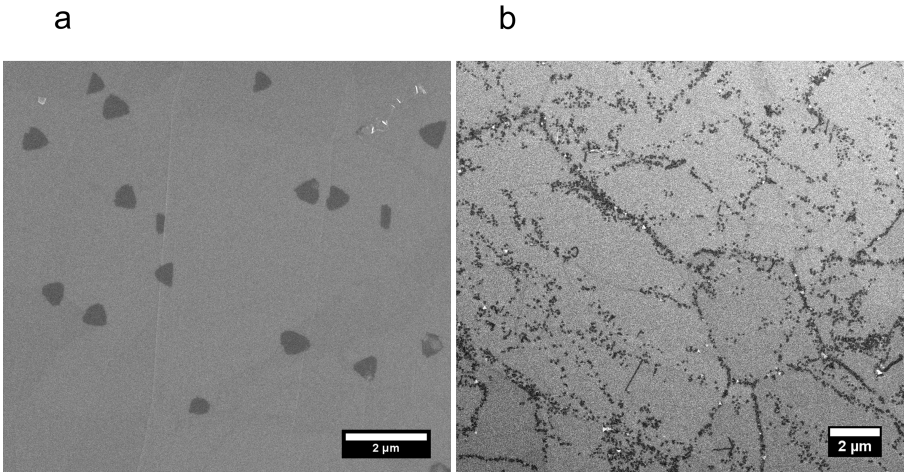

Figure 6.12: *SEM images of MoS_2 grown on HOPG at substrate growth temperatures of (a) 650 °C and (b) 550 °C with a sulphur temperature of 140 °C by Method #2 according to the temperature profile scheme of Figure 3.9(c).*

6.2.3 Growth of MoS_2 on graphene powder and graphene paper

In order to determine if fundamental differences could be observed between MoS_2 growth on HOPG and graphene, growth on commercially available few layer graphene (Morsh) was

attempted. The graphene was used in two forms: a powder consisting of few-layer graphene platelets, shown in the SEM micrograph of Figure 6.13(a) and a graphene 'paper' derived from the same material, Figure 6.13(c). The graphene paper was produced by dispersing the few-layer graphene powder in ultra-pure water with the aid of a surfactant (Triton X-100), vacuum filtering the suspension onto a cellulose nitrate membrane with a 0.1 μm pore size and peeling off the resulting film after thorough washing in ultra-pure water to remove the surfactant.

Although the same growth conditions were employed as for the growth of MoS_2 on HOPG it is clear from Figures 6.13 (a) and (b) that no evidence of MoS_2 can be observed. Likewise, Raman spectra (not shown) were characteristic of the few-layer graphene, with no signal from MoS_2 evident. Given that HOPG and few-layer graphene share the same local atomic structure it is clear that the micron scale roughness and structure of the graphene powder has a significant effect upon growth. It is possible that the higher surface area of the few-layer graphene powder compared with HOPG reduces the density of MoS_2 islands below that which can be readily observed or that the relatively small size of the few-layer graphene platelets prevents the 'capture' of a large enough quantity of precursor upon each to enable nucleation of MoS_2.

The arguments related to surface area outlined above appear supported, at least in part, by the result of attempts to grow MoS_2 on graphene paper shown in Figure 6.13(d). There are clear differences in the SEM micrographs of the pristine graphene paper, Figure 6.13(c) and that after growth, Figure 6.13(d). After growth, a dense layer of particles can be seen on the graphene paper, which have a morphology consistent with that of molybdenum oxides, rather than MoS_2. Therefore, it would appear that although the compact nature of the graphene paper, in comparison with the structure of the graphene powder, localises deposited material to the substrate surface there are still substantial differences between growth on this material than upon HOPG, although the precise causes are currently unclear.

6.3 Conclusions

The CVD growth of MoS_2 on monolayer graphene on copper substrates, few-layer graphene powder, few-layer graphene paper and HOPG have been explored in the preliminary experiments reported in this chapter. It is found that single-step growth of MoS_2 on these graphitic surfaces is far from simple in comparison with growth on natively oxidised silicon surfaces reported in Chapter 5.

In particular, it is found that the upper permissible growth temperature for attempts to grow MoS_2 on copper supported graphene films is limited to below 650 °C due to the sulphurisation and decomposition of the copper substrate. Where MoS_2 growth can be

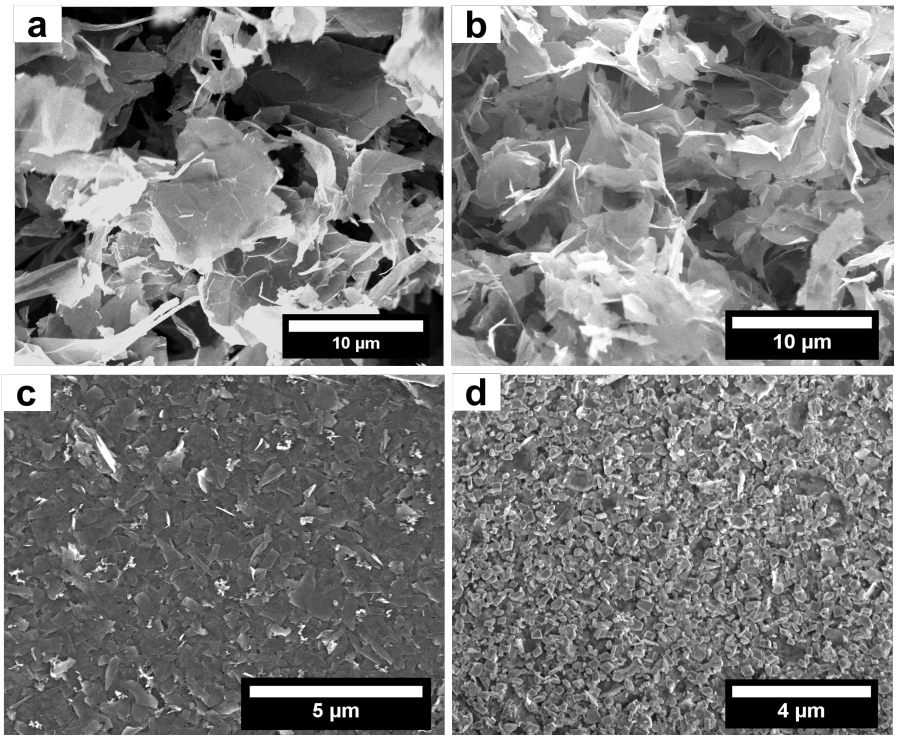

Figure 6.13: *SEM images of graphene powder before (a) and after (b) attempted MoS_2 growth and graphene paper before (c) and after (d) attempted MoS_2 growth.*

inferred from observations of islands of the correct triangular morphology on the graphene surface, they remain a minority species with molybdenum oxides forming the dominant phase within the as-grown films.

Sub-monolayer coverages of MoS_2 were found to be possible to grow on HOPG surfaces and, via choice of the correct temperature profile during growth, the presence of oxides could be minimised. However, despite the assumption that HOPG could act as a model surface for MoS_2 growth on graphene, attempts to grow films on graphene powders and graphene papers demonstrated that this is not the case, indicating the role that surface morphology can play in defining the structure and composition of CVD grown films. Therefore, we can conclude that the single-step CVD growth of continuous MoS_2 films remains a challenge to be addressed in future work.

References

[1] Yuan Liu, Nathan O Weiss, Xidong Duan, Hung-Chieh Cheng, Yu Huang, and Xiangfeng Duan. Van der Waals heterostructures and devices. *Nature Reviews Materials*, 1(9):1–17, 2016.

[2] Zongyou Yin, Hai Li, Hong Li, Lin Jiang, Yumeng Shi, Yinghui Sun, Gang Lu, Qing Zhang, Xiaodong Chen, and Hua Zhang. Single-layer MoS_2 phototransistors. *ACS Nano*, 6(1):74–80, 2012.

[3] Kin Fai Mak, Changgu Lee, James Hone, Jie Shan, and Tony F Heinz. Atomically thin MoS_2: a new direct-gap semiconductor. *Physical Review Letters*, 105(13):136805, 2010.

[4] Andrea Splendiani, Liang Sun, Yuanbo Zhang, Tianshu Li, Jonghwan Kim, Chi-Yung Chim, Giulia Galli, and Feng Wang. Emerging photoluminescence in monolayer MoS_2. *Nano Letters*, 10(4):1271–1275, 2010.

[5] Kallol Roy, Medini Padmanabhan, Srijit Goswami, T Phanindra Sai, Gopalakrishnan Ramalingam, Srinivasan Raghavan, and Arindam Ghosh. Graphene - MoS_2 hybrid structures for multifunctional photoresponsive memory devices. *Nature Nanotechnology*, 8(11):826–830, 2013.

[6] Woo Jong Yu, Zheng Li, Hailong Zhou, Yu Chen, Yang Wang, Yu Huang, and Xiangfeng Duan. Vertically stacked multi-heterostructures of layered materials for logic transistors and complementary inverters. *Nature Materials*, 12(3):246–252, 2013.

[7] A. Mishchenko, J. S. Tu, Y. Cao, R. V. Gorbachev, J. R. Wallbank, M. T. Greenaway, V. E. Morozov, S. V. Morozov, M. J. Zhu, S. L. Wong, F. Withers, C. R. Woods, Y. J. Kim, K. Watanabe, T. Taniguchi, E. E. Vdovin, O. Makarovsky, T. M. Fromhold, V. I. Fal'ko, A. K. Geim, L. Eaves, and K. S. Novoselov. Twist-controlled resonant tunnelling in graphene/boron nitride/graphene heterostructures. *Nature Nanotechnology*, 9(10):808–813, 2014.

[8] Hiroki Ago, Hiroko Endo, Pablo Solis-Fernandez, Rina Takizawa, Yujiro Ohta, Yusuke Fujita, Kazuhiro Yamamoto, and Masaharu Tsuji. Controlled van der Waals epitaxy of monolayer MoS_2 triangular domains on graphene. *ACS Applied Materials & Interfaces*, 7(9):5265–5273, 2015.

[9] Jianping Shi, Mengxi Liu, Jinxiu Wen, Xibiao Ren, Xiebo Zhou, Qingqing Ji, Donglin Ma, Yu Zhang, Chuanhong Jin, Huanjun Chen, et al. All chemical vapor deposition synthesis and intrinsic bandgap observation of MoS_2/graphene heterostructures. *Advanced Materials*, 27(44):7086–7092, 2015.

[10] Yumeng Shi, Wu Zhou, Ang-Yu Lu, Wenjing Fang, Yi-Hsien Lee, Allen Long Hsu, Soo Min Kim, Ki Kang Kim, Hui Ying Yang, Lain-Jong Li, et al. van der Waals epitaxy of MoS_2 layers using graphene as growth templates. *Nano Letters*, 12(6):2784–2791, 2012.

[11] Dancheng Zhu, Haibo Shu, Feng Jiang, Danhui Lv, Vijayshankar Asokan, Omar Omar, Jun Yuan, Ze Zhang, and Chuanhong Jin. Capture the growth kinetics of CVD growth of two-dimensional MoS_2. *npj 2D Materials and Applications*, 1(1):1–8, 2017.

[12] Kai-Ge Zhou, Freddie Withers, Yang Cao, Sheng Hu, Geliang Yu, and Cinzia Casiraghi. Raman modes of MoS_2 used as fingerprint of van der Waals interactions in 2-D crystal-based heterostructures. *ACS Nano*, 8(10):9914–9924, 2014.

[13] Goki Eda, Hisato Yamaguchi, Damien Voiry, Takeshi Fujita, Mingwei Chen, and Manish Chhowalla. Photoluminescence from chemically exfoliated MoS_2. *Nano Letters*, 11(12):5111–5116, 2011.

[14] Changgu Lee, Hugen Yan, Louis E Brus, Tony F Heinz, James Hone, and Sunmin Ryu. Anomalous lattice vibrations of single-and few-layer MoS_2. *ACS Nano*, 4(5):2695–2700, 2010.

[15] Erik Pollmann, Juliana M Morbec, Lukas Madauß, Lara Bröckers, Peter Kratzer, and Marika Schleberger. Molybdenum disulfide nanoflakes grown by chemical vapor deposition on graphite: Nucleation, orientation, and charge transfer. *The Journal of Physical Chemistry C*, 124(4):2689–2697, 2020.

[16] Peichao Zhang, Yimei Fang, Yinghui Zhou, Wen Wan, Xiaolan Yan, Rui Zhang, Shunqing Wu, Zi-Zhong Zhu, Weiwei Cai, and Junyong Kang. Epitaxial growth and intrinsic nature of molybdenum disulfide on graphite. *Applied Physics Express*, 10(5):055201, 2017.

[17] Antal A Koós, Péter Vancsó, Gábor Z Magda, Zoltán Osváth, Krisztián Kertész, Gergely Dobrik, Chanyong Hwang, Levente Tapasztó, and László P Biró. STM study of the MoS_2 flakes grown on graphite: A model system for atomically clean 2D heterostructure interfaces. *Carbon*, 105:408–415, 2016.

[18] Oliver Ochedowski, Kolyo Marinov, Nils Scheuschner, Artur Poloczek, Benedict Kleine Bussmann, Janina Maultzsch, and Marika Schleberger. Effect of contaminations and surface preparation on the work function of single layer MoS_2. *Beilstein Journal of Nanotechnology*, 5(1):291–297, 2014.

[19] Erik Pollmann, Philipp Ernst, Lukas Madauß, and Marika Schleberger. Ion-mediated growth of ultra thin molybdenum disulfide layers on highly oriented pyrolytic graphite. *Surface and Coatings Technology*, 349:783–786, 2018.

[20] Ki Kang Kim, Alfonso Reina, Yumeng Shi, Hyesung Park, Lain-Jong Li, Young Hee Lee, and Jing Kong. Enhancing the conductivity of transparent graphene films via doping. *Nanotechnology*, 21(28):285205, 2010.

[21] G. H. Wells, T. Hopf, K. V. Vassilevski, E. Escobedo-Cousin, N. G. Wright, A. B. Horsfall, J. P. Goss, A. G. O'Neill, and M. R. C. Hunt. Determination of the adhesion energy of graphene on sic(0001) via measurement of pleat defects. *Applied Physics Letters*, 105(19), 2014.

[22] Donovan Enrique Diaz-Droguett, R El Far, VM Fuenzalida, and Alejandro Leopoldo Cabrera. In situ-Raman studies on thermally induced structural changes of porous MoO_3 prepared in vapor phase under He and H_2. *Materials Chemistry and Physics*, 134(2-3):631–638, 2012.

[23] Jeffrey D Cain, Fengyuan Shi, Jinsong Wu, and Vinayak P Dravid. Growth mechanism of transition metal dichalcogenide monolayers: the role of self-seeding fullerene nuclei. *ACS Nano*, 10(5):5440–5445, 2016.

Chapter 7

Summary and Further work

This chapter gives a brief summary of the data presented in this thesis. It then discusses which future experiments could be done to build on the research in this work.

7.1 Summary and Conclusions

At the beginning of this thesis, a brief introduction to graphene and the other member of the 2-D transition metal dichalcogenides materials, MoS_2 was given. The structures and properties of graphene and MoS_2 were described. This discussion also included several ways of producing graphene and MoS_2, ranging from mechanical exfoliation to chemical vapour deposition, as well as their advantages and disadvantages. In Chapter 4, the growth of graphene by CVD is studied by looking at the effects of methane flow rate, growth temperatures, pre-treatment, and growth time on graphene growth. This investigation found that a high methane concentration in graphene synthesis results in a graphene multilayer with a high defect intensity that can delaminate from the copper substrate. There is no self-limitation of growth to a single graphene monolayer under these conditions. It was found that for acetic acid treated samples, the quality of graphene grown depends strongly on the growth temperature. With increasing growth temperatures from (1065-1075 °C) the areal graphene coverage increased from 58% to 93%. The effect of growth time on graphene coverage and film quality was also explored on these samples. Acetic acid etched copper foils were grown at 1065 °C with 1 sccm CH_4 flow rate for various times (4, 6, 9, and 12 minutes). It was found that the initial coverage increased from 58% to 82% almost linearly. However, graphene coverage does not increase beyond that point. So, the temperature and flow rate are not enough to create a supersaturated surface under these conditions. The influence of surface pre-treatment was also described in Chapters 3 and 4, as the morphology of the substrate can affect graphene growth. It was found that the graphene grown on electropolished copper and nitric acid etched copper contained larger domains than graphene grown on copper etched with acetic acid. When compared to the position of the peaks in acetic acid samples, the G and $2D$ peaks in electropolished and nitric acid samples shifted up to a higher wavenumber.

Chapter 5 discussed the growth of MoS_2 on Si substrates. Chemical vapour deposition is also used for growing monolayer and few-layer MoS_2 films from MoO_3 and sulphur precursors. SEM and Raman spectroscopy show how changing the time of evaporation of the precursor materials affects the growth of MoS_2: if sulphur is evaporated before the MoO_3, there are no molybdenum (sulph)oxide particles present on the surface, whereas if MoO_3 is evaporated before sulphur, molybdenum (sulph)oxides are found to grow on the surface and are not converted to MoS_2. The defect density in the MoS_2 films is shown to be influenced by the sulphur flux. The influence of sulphur partial pressure on MoS_2 growth is also considered. XPS shows that the effect of increasing the suphur partial pressure is to cause incomplete surface coverage but low defect density, due to site blocking by sulphur atoms.

Chapter 6 focused on the growth of MoS_2 directly on graphene/Cu and on graphite by CVD methods. In both cases, it was found that there was limited MoS_2 coverage. The growth of MoS_2 on graphene/Cu was limited to a Cu substrate as there is a strong reaction between the sulphur and Cu. When the sample and sulphur temperature were lowered, some particles were seen, but no heterostructures were found, as evidenced by Raman spectra. When looking at the growth of MoS_2 on graphite, it was found that the coverage of MoS_2 was reduced with increasing the temperature of sulphur, a similar observation to that of MoS_2 on Si with increasing sulphur temperature. The growth of MoS_2 was found to be coordinated at the graphite grain boundary and the step edges, with very little growth found on flat surfaces. It was concluded that growth of MoS_2 on graphene and graphite did not attain the same high coverage of continuous MoS_2 as growth on Si, demonstrating that MoS_2 growth is highly dependent on the morphology of the surface.

7.2 Further work

The research outlined in this thesis aims to lay the foundation for the controlled growth of high-quality van der Waals heterostructures to be used in devices such as those outlined in the introductory chapters of this thesis (FFETs, photodetectors, photovoltaics, etc.). The most important step in building any structure is the foundation upon which it is built, which, for CVD-based methodologies, is the graphene layer due to the requirement for the presence of a copper substrate for the catalytic decomposition of hydrocarbons. Uniform graphene films have been produced on Cu-treated Ni and a MoS_2 layer on Si using APCVD, so it would be possible to produce a bilayer heterostructure. This will involve the deposition of a layer of MoS_2 (which has layer-dependent band gaps) to create a graphene-2D semiconductor bilayer junction. Employing MoS_2 as the two-dimensional semiconducting solid, as this has been one of the most studied graphene analogues, allows the growth process to be benchmarked through a comparison with the literature. In addition to investigating the growth mode, morphology, and defect density and the dependence of these on growth conditions, approaches for transfer of the bilayers to insulating structures will be studied, based on those currently employed successfully for graphene. If successful, transfer to an insulating substrate will enable simple transport measurements, such as conductivity, and provide the basis for device fabrication from multilayer van der Waals heterostructures.

Chapter 6 discusses the growth of MoS_2 on graphene and on graphite. Direct growth of MoS_2 on graphene and graphite is likely to be very difficult, and other methods are needed. A method, such as transferring graphene from Cu to any arbitrary substrate, could be attempted to avoid the reaction between the sulphur and Cu. This could then facilitate the growth of a MoS_2-graphene heterostructure. It might then be possible to transfer another layer of graphene on top of the MoS_2, creating a 3-layer heterostructure, and the interaction

between MoS_2 and graphene in a MoS_2/graphene heterostructure can be studied.